Generalized factorial cumulants

applied to Coulomb-blockade systems

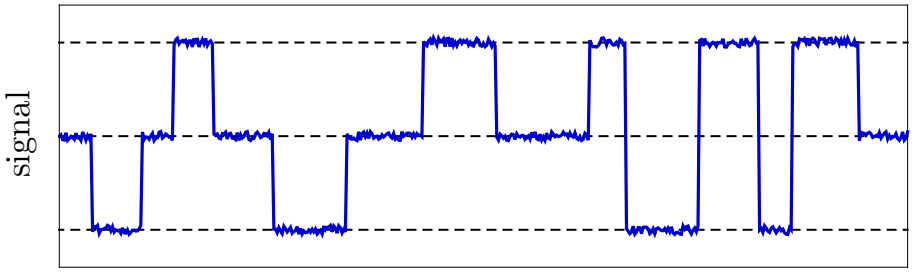

Von der Fakultät für Physik
der Universität Duisburg-Essen
genehmigte Dissertation
zur Erlangung des Grades
Dr. rer. nat.
von

Philipp Stegmann
aus Bottrop

Tag der Disputation: 05.07.2017
Referent: Prof. Dr. Jürgen König
Korreferent: Prof. Dr. Christian Flindt
Korreferent: Prof. Dr. Thomas Guhr

Summary

Tunneling of electrons through a Coulomb-blockade system is a stochastic (i.e., random) process. The number of the transferred electrons per time interval is determined by a probability distribution. The form of this distribution can be characterized by quantities called cumulants. Recently developed electrometers allow for the observation of each electron transported through a Coulomb-blockade system in real time. Therefore, the probability distribution can be directly measured.

In this thesis, we introduce **generalized factorial cumulants** as a new tool to analyze the information contained in the probability distribution. For any kind of Coulomb-blockade system, these cumulants can be used as follows:

First, **correlations** between the tunneling electrons are proven by a certain sign of the cumulants. In the limit of short time intervals, additional criteria indicate correlations, respectively. The cumulants allow for the detection of correlations which cannot be noticed by commonly used quantities such as the current noise. We comment in detail on the necessary ingredients for the presence of correlations in the short-time limit and thereby explain recent experimental observations.

Second, we introduce a mathematical procedure called **inverse counting statistics**. The procedure reconstructs, solely from a few experimentally measured cumulants, characteristic features of an otherwise unknown Coulomb-blockade system, e.g., a lower bound for the system dimension and the full spectrum of relaxation rates.

Third, the cumulants reveal **coherent oscillations** or other processes transferring single electrons in a regular manner. The sensitivity for the oscillations increases dramatically in comparison to the commonly used quantities as the waiting times and finite-frequency current noise. The increased sensitivity is especially convenient for the detection of coherent oscillations in already existing experimental set-ups.

Fourth, a violation of **detailed balance** is indicated by the cumulants. Detailed balance means the absence of net probability currents in the system's state space for the stationary limit. A violation of detailed balance is possible if the state space consist of more than two states connected by tunneling rates in such a way that a closed loop is formed.

We illustrate the application of the generalized factorial cumulants for the transport through single metallic islands and quantum dots tunnel coupled to superconducting, ferromagnetic, or normal metallic electrodes. For all these example systems, it has been demonstrated already in experiments that electron transport can be observed in real time. Thus, our results can be applied immediately to such experimental realizations of a Coulomb-blockade system.

Zusammenfassung

Das Tunneln von Elektronen durch ein Coulomb-Blockade-System ist ein stochastischer Prozess bzw. Zufallsprozess. Die Anzahl an transferierten Elektronen pro Zeitintervall ist bestimmt von einer Wahrscheinlichkeitsverteilung. Die Form dieser Verteilung kann durch Größen charakterisiert werden, die Kumulanten genannt werden. Kürzlich entwickelte Elektrometer ermöglichen es, jedes Elektron in Echtzeit zu beobachten, das durch ein Coulomb-Blockade-System transportiert wird. Deshalb kann die Wahrscheinlichkeitsverteilung direkt gemessen werden.

In dieser Dissertation führen wir **generalisierte faktorielle Kumulanten** als ein neues Instrument ein, um die in der Wahrscheinlichkeitsverteilung enthaltenden Informationen zu analysieren. Für jede Art von Coulomb-Blockade-System können diese Kumulanten wie folgt genutzt werden:

Erstens, **Korrelationen** zwischen den tunnelnden Elektronen werden durch ein bestimmtes Vorzeichen der Kumulanten nachgewiesen. Im Limes kurzer Zeitintervalle zeigen zusätzliche Kriterien jeweils Korrelationen an. Die Kumulanten ermöglichen das Detektieren von Korrelationen, die von üblicherweise verwendeten Messgrößen wie dem Stromrauschen nicht bemerkt werden. Wir erläutern im Detail die notwendigen Voraussetzungen für das Vorhandensein von Korrelationen im Limes kurzer Zeiten und erklären dabei jüngste experimentelle Beobachtungen.

Zweitens, wir führen eine mathematische Prozedur namens **inverse Zählstatistik** ein. Die Prozedur rekonstruiert, ausschließlich mittels einiger experimentell gemessener Kumulanten, charakteristische Merkmale eines ansonsten unbekannten Coulomb-Blockade-Systems, z. B. eine untere Grenze für die Dimension des Systems und das volle Spektrum an Relaxationsraten.

Drittens, die Kumulanten offenbaren **kohärente Oszillationen** oder andere Prozesse, die einzelne Elektronen in einer regelmäßigen Weise transferieren. Die Sensitivität für die Oszillationen steigt dramatisch an im Vergleich zu den im Allgemeinen genutzten Messgrößen wie den waiting times und dem frequenzabhängigen Stromrauschen. Die erhöhte Sensitivität ist insbesondere günstig, um kohärente Oszillationen in bereits existierenden experimentellen Aufbauten zu detektieren.

Viertens, eine Verletzung des Prinzips des **detaillierten Gleichgewichts** wird von den Kumulanten angezeigt. Detailliertes Gleichgewicht bezeichnet die Abwesenheit von netto Wahrscheinlichkeitsströmen im Zustandsraum des Systems für den stationären Limes. Eine Verletzung des detaillierten Gleichgewichts ist möglich, falls der Zustandsraum aus mehr als zwei Zuständen besteht, die über Tunnelraten derart verknüpft sind, dass sich eine geschlossene Schleife bildet.

Wir veranschaulichen die Anwendung der generalisierten faktoriellen Kumulanten für den Transport durch einzelne metallische Inseln oder Quantenpunkte, die an supraleitende, ferromagnetische oder gewöhnliche metallische Elektroden tunnel-gekoppelt sind. Für all diese Beispielsysteme ist bereits in Experimenten demonstriert worden, dass Elektronentransport in Echtzeit beobachtet werden kann. Daher können unsere Resultate sofort auf derartige experimentelle Realisierungen eines Coulomb-Blockade-Systems angewendet werden.

Contents

1 Motivation and outline

Electron transport through nanoscale devices is a very active field of research. Some of the most natural quantities utilized to probe transport are the average current and the current noise [1]. If the noise surpasses a certain threshold value, electron transport is *correlated*. Electrons are transferred in bunches due to some interaction. Moreover, with the finite-frequency noise, one can probe processes transferring electrons at a specific frequency through the system.

A new generation of measurement apparatus has been recently developed to probe electron transport. Mesoscopic electrometers have reached such a high resolution that each transported electron can be observed and counted in real time. Ongoing efforts are made to improve the accuracy of these electrometers further [2].

What are the benefits of those real-time measurements? The current and noise can be measured on much higher resolutions than with conventional techniques [3]. Even if no bias voltage is applied and the average current vanishes, equilibrium electron fluctuations can be detected. Moreover, one can directly observe different kinds of electron bunches [4, 5], whereas the noise yields only the average electron number per bunch. In this sense, it has been suggested to study multilevel-quantum dots [6] or superconducting systems [7–12]. Furthermore [3], the real-time data yields tunneling rates and occupation probabilities of different system states. Information about excited states and relaxation times has been obtained.

Counting the number of transferred electrons gives access to the *full counting statistics*. The statistics is characterized by the probability distribution $P_N(t)$ that N electrons have been transferred in a time interval $[0, t]$. In general, it is quite challenging to deal simultaneously with all information contained in $P_N(t)$ or any other distribution describing a stochastic process. An easier approach is to analyze scalar quantities calculated from the respective distribution. The value of each scalar should *accumulate* information from the distribution into one *meaningful statement*. Such a scalar can be called *cumulant*. It depends on the scientific field what can be considered to be a meaningful statement.

In the field of mathematical statistics, quantities referred to as cumulants are already known for a long time. A cumulant C_m of order m makes a statement concerning the form of a distribution. The cumulant C_1 is the mean of the distribution, C_2 quantifies the width of the distribution, C_3 the asymmetry, and C_4 the degree of peakedness.

How must cumulants be defined which do not aim at a mere characterization of the distribution's form, but make statements leading to a better understanding of the electron transport? The quantity C_1 from mathematical statistics yields the current and C_2 the noise. Thus, a quite obvious assumption is that all C_m are convenient to study electron transport. The C_m of higher-order $m > 2$ have been studied extensively for the full counting statistics of electron transport. Typically, striking oscillations of the C_m have been observed both in theory [13–16] and experiment [17–19]. In 2009 [20], it has been

explained why these oscillations are a universal phenomenon, appearing as function of almost any variation of electron transport. Hence, the C_m seem not conveniently defined to lead to a deeper understanding of the studied transport scenario.

Ordinary cumulants C_m have properties advantageous to handle distributions of a continuos variable. In contrast, for distributions of an integer variable N, the lesser known *factorial cumulants* $C_{\mathrm{F},m}$ are more appropriate [21]. For the first time in 2011, the $C_{\mathrm{F},m}$ haven been applied to study electron transport [22]. The factorial cumulants are linear combinations of the C_m. Therefore, they contain the same information than the ordinary cumulants. However, the C_m are combined in such a way that universal oscillations cancel out each other. Hence, the factorial cumulants are more conveniently defined to study electron transport.

In this thesis, we aim at the most convenient definition of cumulants as explained in the following. Each cumulant should accumulate information from $P_N(t)$ into one value and make a meaningful statement leading to a better understanding of the electron transport. To some extent, the accumulation should be tunable in order to handle a large plethora of systems, varying both drastically or only slightly. The range of accessible statements should be larger than for the C_m and $C_{\mathrm{F},m}$. Nevertheless, the definition should be as general that meaningful statements obtainable from the current, noise, and the $C_{\mathrm{F},m}$ are already included. First, this ensures that results can easily be compared with other studies. Second, if a system is studied by such a conventional quantity, one immediately sees that the cumulants provide a possible alternative.

To fulfill all these demands, we introduce *generalized factorial cumulants*. The outline of this thesis is as follows. In Chapter 2, we explain the functionality of the electrometers measuring real-time electron transport. The probed systems are commonly referred to as *Coulomb-blockade systems*. In Chapter 3, we sketch the mathematical background of ordinary cumulants C_m and factorial cumulants $C_{\mathrm{F},m}$. Afterwards, we introduce generalized factorial cumulants $C_{s,m}$. We explain how these cumulants indicate correlated electron transport. The sensitivity of the $C_{s,m}$ for correlations surpasses dramatically the sensitivity of the current noise and the $C_{\mathrm{F},m}$ as illustrated in Chapter 4. In Chapter 5, we discuss for short time intervals $[0, t]$ that, in addition to the sign, also the time-dependence or an s-dependence of the $C_{s,m}$ indicates correlations. However, generalized factorial cumulants can not only be used to prove the presence of correlations. As discussed in Chapter 6, the $C_{s,m}$ yield characteristic features of the underlying stochastic system, e.g., a lower bound for the system dimension and the full spectrum of relaxation rates. Moreover, as illustrated in Chapter 7, the cumulants can be used to detect coherent oscillations or other processes transferring electrons at a specific frequency. Finally in Chapter 8, we explain how a violation of detailed balance can be proven by cumulants. The conclusions of this thesis are given in Chapter 9.

2 Electron counting in Coulomb-blockade systems

Recent progress in nanotechnology has led to the development of electrometers so sensitive that transport of individual electrons can be observed in real time. In this chapter, we summarize the current state of this technology. In Sections 2.1 and 2.2, we specify what kind of systems can be probed by these electrometers: Coulomb-blockade systems like the single-electron box (SEB) and the single-electron transistor (SET). The working principle of the electrometers is explained in Section 2.3.

2.1 Coulomb-blockade systems based on metallic islands

Charge current consists of single electrons transferred through the respective device. However, only under certain conditions the charge quantization can be noticed as explained in the following. Consider the set-up of two metallic particles depicted in Figure 2.1 (a). The equivalent electric circuit is shown in Figure 2.1 (b). The conduction electrons in each metallic particle can be considered to be noninteracting and delocalized. The size of each particle confines the free movement of these electrons. Therefore, the electrons occupy different singe-electron energy levels ε_l (*confinement energies*) with a mean spacing that can be estimated as [23, Section 2.2]

$$\Delta = \frac{2\pi^2\hbar^2}{m\,k_\mathrm{F}\,L^3} \approx 0.15\,\mathrm{eV}\left(\frac{\mathrm{nm}}{L}\right)^3 . \tag{2.1}$$

The electron mass and the volume of each particle are denoted m and L^3, respectively. The Fermi wave number is of the order $k_\mathrm{F} \propto 10\,\mathrm{nm}^{-1}$. The level spacing is so small that the level spectrum of each particle can be considered to be a continuum, see Figure 2.1 (c).

The right particle (blue) is capacitively coupled to a gate electrode. Due to the applied voltage V_G, the particle is on a lower potential than the left particle (red). If the two particles are contacted, a net charge current flows. Each electron from the left continuum can occupy a free state in the right continuum if it can provide the necessary energy. Of course, the confinement energy must be paid. Furthermore, Coulomb repulsion has to be taken into account. Consequently, each additional electron charge costs electrostatic energy.

Since excess charges are distributed continuously over a metallic particle, the electrostatic energy can be modeled conveniently by capacitances C_L and C_G, see Figure 2.1 (b). The capacitances depend solely on the form and permittivity of the particles and gate electrode. Moreover, we assume in the following that the left particle is a large electron reservoir and the right particle a small *metallic island*. Hence, the potential of the reservoir is not

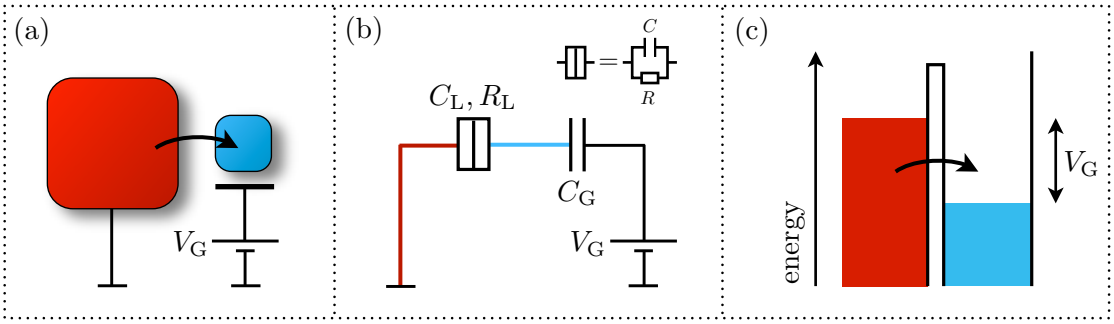

Figure 2.1: The single-electron box (SEB): one large metallic reservoir of electrons (red) weakly tunnel coupled to a mesoscopic metallic island (blue). Via the gate voltage V_G, the box can be filled or emptied. (a) Schematic diagram of the set-up, (b) equivalent electric circuit, and (c) corresponding continua of single-electron energy levels.

affected by the electron flow. The electrostatic energy to bring an integer number of n excess electron charges on the island is

$$E_{es}(n) = E_C(n - n_G)^2\,, \tag{2.2}$$

where the continuous parameter $n_G := C_G\,V_G/\,|e|$ is called the *gate charge*. The parameter $E_C := e^2/2(C_L + C_G)$ is called the *charging energy* of the first electron for $n_G = 0$. In general, the nth excess electron entering the island must provide the charging energy $U(n) = E_{es}(n) - E_{es}(n-1)$, in addition to the confinement energy ε_l. Typical values for the capacitances as function of the surface area L^2 yield [23, Section 2.2]

$$E_C \approx 0.8\,\text{eV}\left(\frac{\text{nm}}{L}\right)^2\,. \tag{2.3}$$

For a macroscopic island, both Δ and E_C are so small that a flowing current transfers a huge number of electrons simultaneously. No sign of quantized charge transport can be observed. However, if the island size is decreased to *mesoscopic* scales ($\sim \mu$m down to $\sim$ nm), the situation changes.

The confinement energy remains small. It is on the scale of neV. Still, a large number of conduction electrons reside on the island. The level spectrum can still be considered to be a continuum. In contrast, the charging energy is of the order of meV or 10 K in temperature units. Thus, if voltages and temperatures are applied on this scale, only one or a few (excess) electrons can be exchanged between the reservoir and island. If the voltages and temperatures are much smaller, electrons cannot be exchanged anymore. The system is in the so called *Coulomb blockade*.

Only a small number of allowed charge states is the first requirement for the observation of single-electron transport in real time. As a second requirement, the charge states must be well isolated from each other in the time domain. Thus, the reservoir and island must be weakly tunnel coupled such that the resistance R_L [see Figure 2.1 (b)] is larger than the inverse of one *conductance quantum* $h/e^2 \approx 26\,\text{k}\Omega$. Then, single excess electron charges are well localized in a mesoscopic space and time of several milliseconds. Excess charges

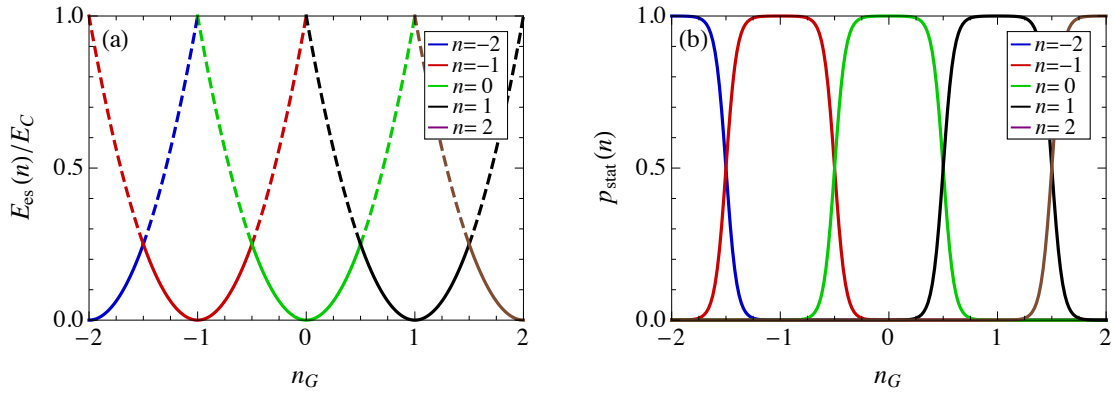

Figure 2.2: (a) Electrostatic energy and (b) stationary occupation probability of a single-electron box (SEB) for different numbers of excess electron charges n as function of the continuous parameter n_G, cf. [24, Section 10.2.1]. Via n_G, the box can be filled or emptied.

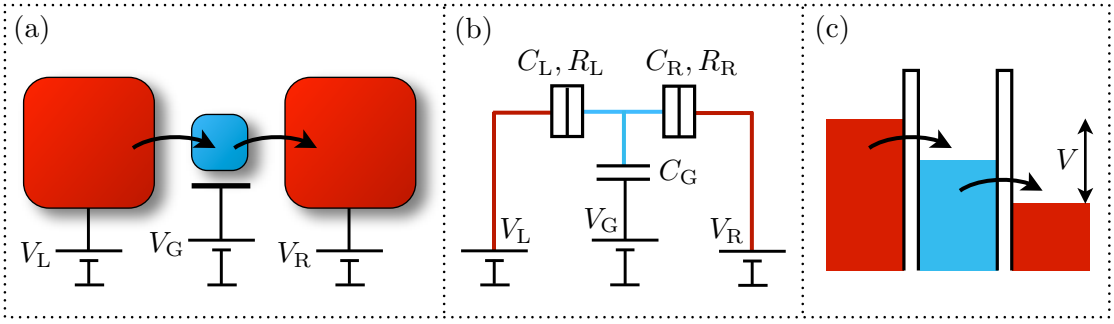

Figure 2.3: The single-electron transistor (SET): a left and right large metallic reservoir of electrons (red) are weakly tunnel coupled to a mesoscopic metallic island (blue). For a negative bias voltage $V = V_L - V_R$ electrons are transferred from left to right. The single-electron current flow can be controlled by the gate voltage V_G. (a) Schematic diagram of the set-up, (b) equivalent electric circuit, and (c) corresponding continua of single-electron energy levels.

quantized in this manner can be observed in real time by the electrometers that will be introduced in Section 2.3. The probed systems are referred to as *Coulomb-blockade systems*.

With increasing time, a gate-voltage-induced potential difference between reservoir and island is counterbalanced by a net electron current I. In the stationary limit, an excess charge n is on the island for which the electrostatic energy $E_{es}(n)$ is minimal, see Figure 2.2 (a). The value of the stationary n is the integer value closest to $n_G(V_G)$ as illustrated in Figure 2.2 (b) depicting the stationary occupation probabilities $p_{stat}(n)$. Thus, by means of the gate voltage V_G, the metallic island can be filled or emptied with single electrons in a controlled manner. The set-up is therefore known as *single-electron box* (SEB). For half-integer values of n_G, two charge states are degenerate. Thus, near such n_G ($\pm 2k_BT/E_C$), temperature-induced fluctuations between two charge states can be observed with a finite occupation probability for each charge state, see Figure 2.2 (b). Of course, averaging over charge fluctuations into and out of the island does not yield a net

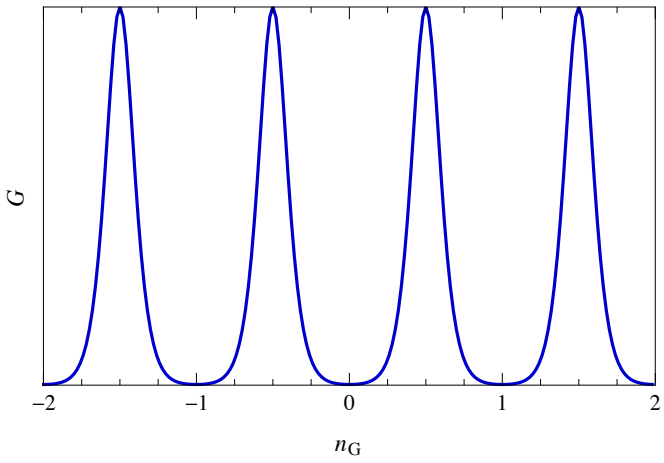

Figure 2.4: Differential conductance $G = \mathrm{d}I/\mathrm{d}V|_{V=0}$ of a single-electron transistor as function of the gate charge, cf. [24, Section 10.2.1].

current I. Nevertheless, these fluctuations can be noticed by an electrometer and will be relevant for the physics discussed in Chapters 4, 5, 6, and 8.

The most basic single-electron system that allows for a permanent net current is depicted in Figure 2.3. A mesoscopic metallic island is weakly tunnel coupled to a left and right electron reservoir. A bias voltage $V = V_\mathrm{L} - V_\mathrm{R}$ is applied such that electrons are transported from left to right. Via the gate voltage V_G, the single-electron current flow can be controlled. The system is therefore referred to as *single-electron transistor* (SET). The electrostatic energy is given by Eq. (2.2) with the charging energy $E_C = e^2/2(C_\mathrm{L} + C_\mathrm{R} + C_\mathrm{G})$ and gate charge $n_\mathrm{G} = (C_\mathrm{L}V_\mathrm{L} + C_\mathrm{R}V_\mathrm{R} + C_\mathrm{G}V_\mathrm{G})/|e|$. If n_G is tuned near a half-integer value ($\pm 2k_\mathrm{B}T/E_C$), the differential conductance $G = \mathrm{d}I/\mathrm{d}V|_{V=0}$ is finite, see Figure 2.4. Away from half-integer values, G is suppressed and the system is in Coulomb blockade. The resulting pattern of peaks is referred to as *Coulomb oscillations*.

A SET accompanied by real-time charge detection has been realized by metallic and superconducting islands [25–32]. Note that a SET can easily be made to a SEB by switching off the bias voltage $V_\mathrm{L} = V_\mathrm{R}$ and keeping both reservoirs at the same temperature.

2.2 Coulomb-blockade systems based on quantum dots

Coulomb-blockade systems like the SEB or the SET can be based on a mesoscopic island as illustrated in the previous section. Although the island is of small size, its confinement energy Δ is many orders below the charging energy E_C. As a result the island can be completely characterized by its charge state, i.e., the number of excess electrons n.

Another approach for building up Coulomb-blockade systems are *quantum dots* [33]. Structures are denoted in this way if not only the charging energy E_C is large, but also the level spacing Δ is on a similar scale. The number of conduction electrons is low ranging from zero to a few hundreds. The level spacing can vary between the different single-electron levels such that a kind of atomic shell structures can be observed. Quantum dots are therefore also denoted as *artificial atoms*. As a further consequence, typically the charge

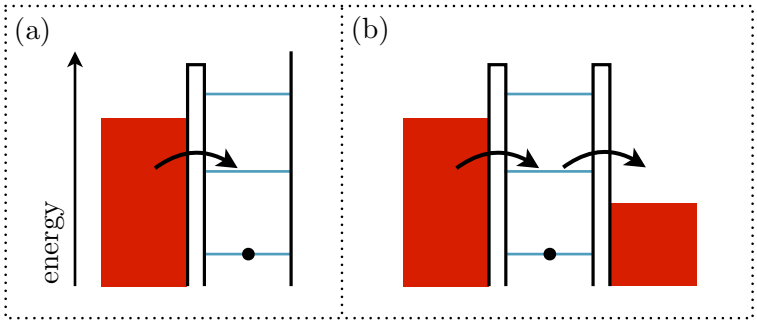

Figure 2.5: (a) Single-electron box (SEB) and (b) single-electron transistor (SET) realized with a quantum dot. Each lead contains a continuum of single-electron levels. The level spacing in the quantum dot is on similar scale as the charging energy.

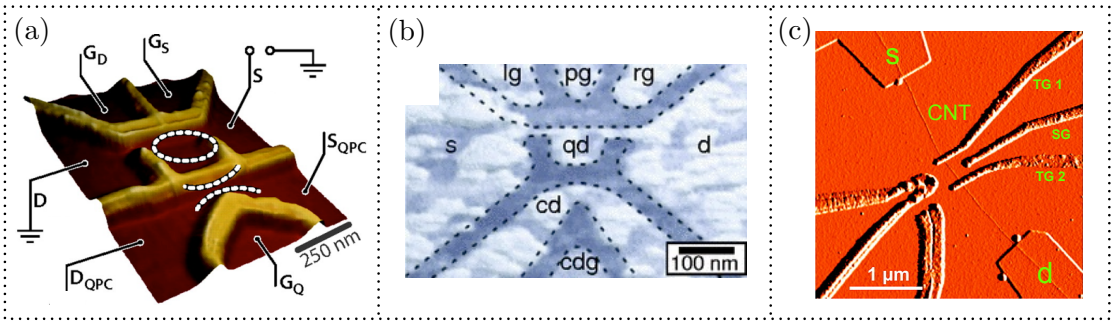

Figure 2.6: Atomic-force-microscopy picture of a SET fabricated by (a) local oxidation of a GaAs/AlGaAs heterostructure, (b) etching of a graphene flake, and (c) a carbon-nantotube with tunnel barriers formed by metallic top gates. The current through the SET flows from s to d. (a) Reprinted from [20] with permission from PNAS. (b) Reprinted with permission from [34]. Copyright 2017 by the American Physical Society. (c) Reprinted with permission from [35]. Copyright 2017 by the American Chemical Society.

state n is not enough to characterize the dot. The occupied levels must be clearly specified, i.e., different microscopic realization of the same charge state must be taken into account. However, an electrometer cannot distinguish between these different microscopic realizations.

The single-electron levels of a quantum-dot based SEB and SET are depicted in Figure 2.5. Only the level spectrums of the reservoirs can be considered to be continua. The electrostatic energy can still be modeled by Eq. (2.2). However, due to the low number of conduction electrons on the dot, the capacitances may change if the number of the excess electrons n changes drastically [33].

A SEB and SET accompanied by real-time charge detection have been realized in semiconductor GaAs/AlGaAs [4, 17–20, 36–43] and Si/SiGe [44–47] heterostructures, see Figure 2.6 (a). At the interface between the two semiconductors, a two-dimensional electron gas is formed aligning the two different Fermi energies. Via voltage-biased metallic gates on top of the surface, local oxidation, or etching, mesoscopic structures can be formed in the electron gas like quantum dots, tunnel junctions, and sensitive electrometers.

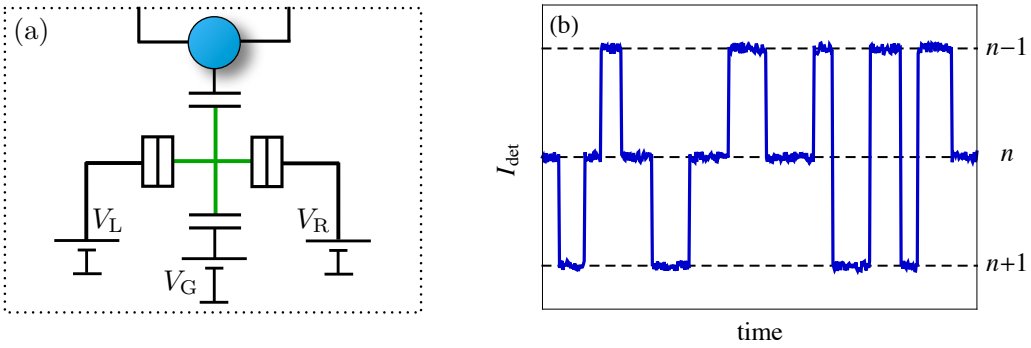

Figure 2.7: (a) Quantum dot (blue) coupled to the island or dot (green) of the detector SET. (b) Time trace of the detector current. The current switches between three discrete values. Each value corresponds to a different charge state ($n-1$, n, or $n+1$) of the dot (blue) in (a).

Another possible realization is given by graphene flakes [34, 48, 49], see Figure 2.6 (b). Dots, tunnel junctions, gate electrodes, and electrometers are carved out of the flake by local etching.

Moreover, InAs-nanowire [50–53] and carbon-nanotube [35, 54] quantum dots have been utilized to form real-time observed SET, see Figure 2.6 (c). Phosphorus-donor-based quantum dots in silicon [55–57] have been used to to build up a real-time observed SEB.

In Chapters 4, 7, and 8, some of the discussed systems are SETs based on quantum dots.

2.3 Single-electron electrometers

Two different kinds of electrometers are commonly used to observe the charge transport through Coulomb-blockade systems like the single-electron box or transistor. The first electrometer is a single-electron transistor itself. The island or dot of the detector SET is capacitively coupled to the island or dot whose charge state shall be observed in real time, see Figure 2.7 (a). Of course, the coupling is weak such that the studied device is not influenced by the detector. If the charge state changes, the gate charge n_G of the detector changes slightly. To maximize the impact, the detector SET is operated at the steepest slope of a conductance peak, see Figure 2.4. Moreover, the tunnel resistances in the detector SET are much smaller than in the inspected device. Therefore, the current through the detector SET adopts almost immediately to a changing charge state. In the end, the detector current switches between discrete values as function of time. A typical *time trace* of the detector current is depicted in Figure 2.7 (b). Each value corresponds to one charge state of the studied device.

In order to increase the sensitivity, a strong capacitive coupling to the detector is more favorable. In this sense, some experimental approaches use a reservoir of the studied device as island for the detector SET [30, 55–57]. However, one has to be sure that the detector does not influence the probed physics.

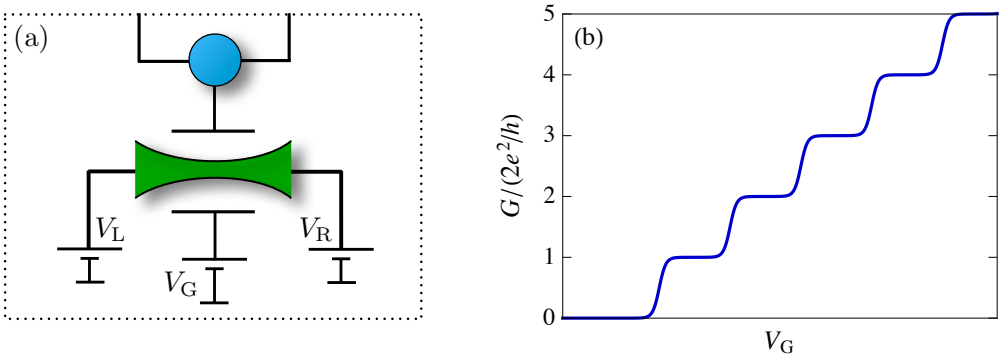

Figure 2.8: (a) Quantum dot (blue) coupled to a QPC (green). (b) Differential conductance $G = \mathrm{d}I/\mathrm{d}V|_{V=0}$ of the QPC as function of an applied gate voltage, cf. [58, Section 11.2]. Temperature smeared steps are observed.

The second kind of electrometers is the *quantum point contact* (QPC) depicted in Figure 2.8 (a). Two electron reservoirs are connected by a narrow wire. The QPC can be easily realized in the semiconductor heterostructures mentioned at the end of Section 2.2. A constriction can be formed in the two-dimensional electron gas (the wire) separating two large electron pools (the reservoirs). In the direction of the wire, electrons can be considered as free with energies $\hbar^2k^2/2m$. In the transverse direction, the motion of the electrons is strongly confined. Thus, continua with energies $\varepsilon_l + \hbar^2k^2/2m$ are formed, which are separated by the confinement energies ε_l. In the case of spin degeneracy, each continuum of states can be occupied by one spin $\uparrow$ and one spin $\downarrow$ electron. A continuum is called *transverse (quantum) channel* and contributes twice the amount of a conductance quantum $2 \times e^2/h$ to the total conductance of the QPC. If temperature smearing $4k_\mathrm{B}T$ is smaller than the spacing between the confinement energies ε_l, one observes the conductance quantization depicted in Figure 2.8 (b). As a function of the gate voltage V_G, the number of populated channels increases in discrete steps.

If the QPC is placed close to the island or dot of a Coulomb-blockade system, a changing charge state influences the transport through the QPC. Island or dot act as a additional gate of the QPC, see Figure 2.8 (a). To maximize the impact, the QPC is tuned close to $G = e^2/h$, i.e., the middle of the first step. Similar to the detector SET, the QPC current switches between discrete values as function of time, see Figure 2.7 (b). Each value corresponds to one charge state of the studied device.

Both the detector SET and the QPC are used as sensitive electrometers. From the fabrication point of view, it is convenient if both the device and the detector can be easily defined in the same process. A detector SET is typically used for the charge detection of islands [25–32], graphene quantum dots [34, 48, 49], carbon-nanotube dots [35, 54], and phosphorus-donor-based dots in silicon [55–57]. For an InAs-nanowire quantum dot [50–53], the QPC is preferred. In semiconductor heterostructures, both the detector-SET [36, 37, 47] and the QPC [4, 17–20, 38–46] have been realized. However, the QPC is used more frequently. Its fabrication requires only one additional voltage-biased gate, whereas the detector SET requires the gate and moreover two tunnel contacts.

3 Full counting statistics

In this chapter, we give an introduction to the field of full counting statistics. The statistics is characterized by the probability distribution $P_N(t)$ that N electrons have been transferred in a time interval $[0, t]$, see Section 3.1. From this distribution, ordinary statistical moments and cumulants can be derived as introduced in Section 3.2. For probability distributions of integer-valued stochastic variable, like the integer number N, it is more convenient to study factorial moments and cumulants as introduced in Section 3.3. By means of the factorial cumulants, correlations between the counted electrons can be identified as explained in Section 3.4. Even more sensitive and versatile quantities are the *generalized* factorial cumulants defined in Section 3.5. The introduction of generalized factorial cumulants to the field of full counting statistics is the aim of this thesis. These cumulants can be directly obtained from the measured $P_N(t)$. The theoretical framework to simulate cumulants is outlined in Section 3.6.

3.1 Probability distribution

In Chapter 2, real-time charge detection by detectors based on a SET or QPC has been elucidated. The output of the detector is a long time trace as depicted in Figure 3.1 (a). Each current value corresponds to a different charge state of the inspected island or quantum dot. In the following, we simply refer to the "dot" for both the island and the quantum dot.

From the long time trace, we can obtain the *full counting statistics* of electron transfer as illustrated in the following. Each step between one of the charge states indicates an electron transfer process. If the charge increases, a corresponding number of electrons has tunneled into the dot. Such processes are indicated by red spikes in Figure 3.1 (b). If the charge decreases, a corresponding number of electrons has tunneled out of the dot, green spikes in Figure 3.1 (c). Note that tunneling processes can transfer a single as well as multiple electrons simultaneously, cf. Chapter 5.

To obtain the full counting statistics, we divide the long time trace $\mathcal{T}$ in intervals of length t. For each interval j, we count the number N_j of either the entering *or* leaving electrons. Finally, we obtain the probability distribution

$$P_N(t) := \sum_j \frac{t\,\delta_{N,N_j}}{\mathcal{T}} \tag{3.1}$$

that N electrons have been transferred in a time interval $[0, t]$, see Figure 3.2. This distribution characterizes the counting statistics and is the basis for the remaining chapters of this thesis.

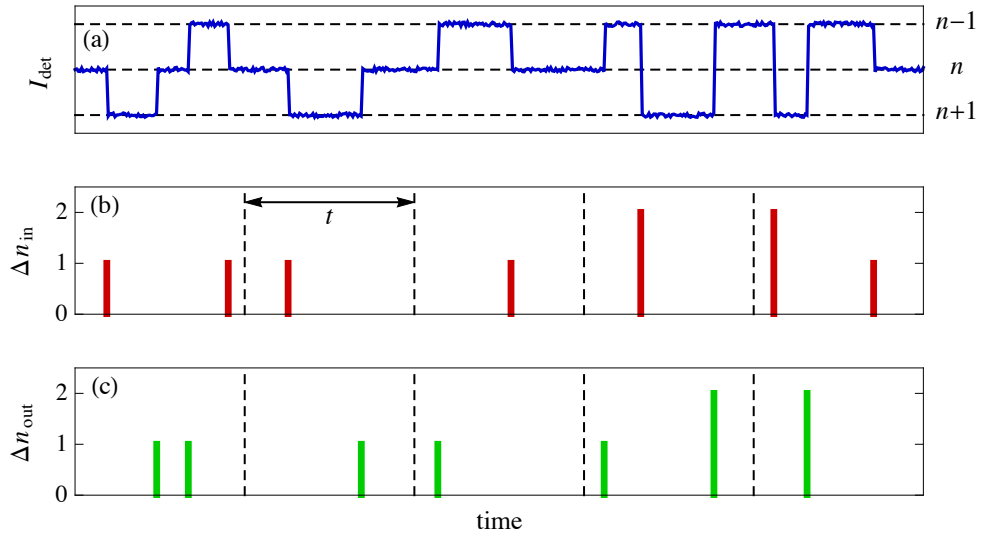

Figure 3.1: (a) Long time trace of the detector current. Each of the three discrete current values corresponds to one charge state of a island or quantum dot. (b) Each spike corresponds to a certain number of electrons tunneling in or (c) out. Counting the number of either tunneling in or out electrons in the intervals t yields the probability distribution $P_N(t)$ for the transfer of N electrons.

We emphasize that a detector based on a SET or QPC can usually *not* distinguish if electrons leave (enter) the dot in the direction of the source *or* drain electrode.[1] Possessing this information, we could count electrons tunneling in the direction of the source (drain) electrode with negative (positive) integers. We would obtain the statistics of the *net charge transport*. We do not discuss such net counting in this thesis and therefore $N \geq 0$. However, in Section 4.3 and Chapter 7, electron transport from source to drain is *unidirectional*. Electrons do not tunnel in the opposite direction as defined by a large bias voltage. Hence, the $P_N(t)$ obtained from our counting procedure is equal to the probability distribution that a net charge of N electrons has been transferred to the drain electrode.

3.2 Ordinary moments and cumulants

By means of the probability distribution, statistical moments

$$\langle N^m \rangle (t) := \sum_{N=0}^{\infty} N^m P_N(t) \tag{3.2}$$

of order m can be calculated. The first moment $\langle N \rangle (t)$ is the mean of the probability distribution. For the net-transport statistics, the first moment yields the average current $\langle I \rangle = \lim_{t\to\infty} \langle N \rangle (t)/t$ through the system. To quantify deviations from the average

[1] If two dots are tunnel coupled in series and the charge on each dot is detected separately, the direction of the tunneling processes can be obtained. However, such case is not considered in this thesis.

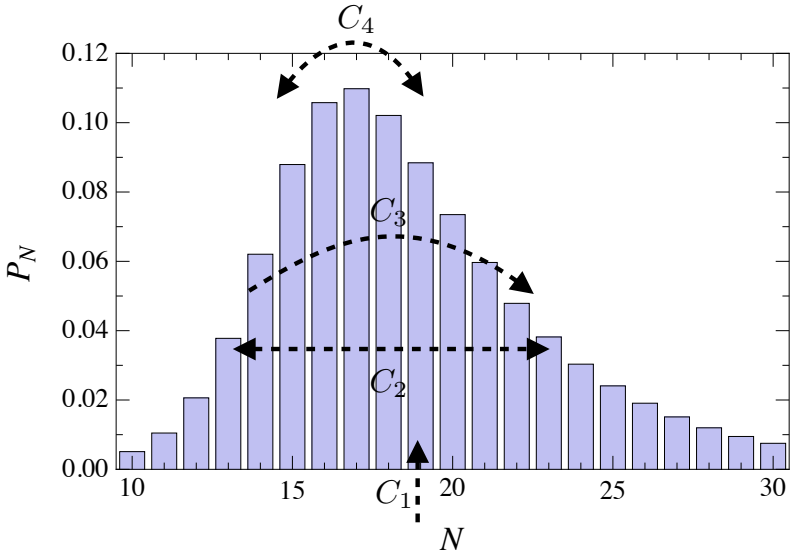

Figure 3.2: A hypothetical probability distribution characterized by the mean $C_1 = \langle N \rangle$, width $C_2 = \langle (N - \langle N \rangle)^2 \rangle$, skewness $C_3 = \langle (N - \langle N \rangle)^3 \rangle$, and kurtosis C_4. All four cumulants are positive for the depicted distribution.

electron tunneling, central moments can be defined

$$\langle (N - \langle N \rangle)^m \rangle (t) := \sum_{N=0}^{\infty} (N - \langle N \rangle)^m P_N(t) \,. \tag{3.3}$$

Due to the definition, the first central moment is vanishing. The second central moment $\langle N^2 \rangle (t) - \langle N \rangle^2 (t)$ is the variance of the probability distribution and quantifies the width of the distribution. For the net-transport statistics, the second central moment yields the zero-frequency current noise $S(0) = \lim_{t\to\infty} 2 \langle (N - \langle N \rangle)^2 \rangle (t)/t$ [58, Section 20.3]. The third moment $\langle N^3 \rangle (t) - 3 \langle N \rangle (t) \langle N^2 \rangle (t) + 2 \langle N \rangle^3 (t)$ is called the skewness and characterizes the asymmetry of the distribution. Symmetric probability distributions have a vanishing skewness [59, Section 2.1.2], whereas a negative (positive) skewness implies a longer left (right) tail of the probability distribution, cf. Figure 3.2.

An elegant way to combine the information of all moments is given by the moment-generating function

$$\mathcal{M}(z,t) := \left\langle e^{Nz} \right\rangle (t) = \sum_{N=0}^{\infty} e^{Nz} P_N(t) \,, \tag{3.4}$$

which is the Laplace transformation of the probability distribution. The analogous generating function for the central moments is given by Eq. (3.4) after replacing e^{Nz} with $e^{(N-\langle N \rangle)z}$. The relation to the moments becomes clear by writing the generating function as Taylor series $\mathcal{M}(z,t) = \sum_m \langle N^m(t) \rangle \, z^m/m!$. Taking the mth derivative at $z = 0$ leads to the corresponding moment

$$\langle N^m \rangle (t) = \frac{\partial^m}{\partial z^m} \mathcal{M}(z,t) \bigg|_{z=0} \,. \tag{3.5}$$

If the total electron transport can be separated into independent subprocesses, the total probability distribution $P_N(t)$ can be expressed by probability distributions $P_N(t,j)$ of the different subprocesses j

$$P_N(t) = \sum_{N_1,N_2,\cdots} P_{N_1}(t,1)P_{N_2}(t,2)\cdots\,, \tag{3.6}$$

where in each summand $\sum_j N_j = N$. The corresponding moment-generating function factorizes into a product of the generating functions of the different subprocesses, see Appendix A.1,

$$\mathcal{M}(z,t) = \prod_j \mathcal{M}(z,t,j)\,, \tag{3.7}$$

where $\mathcal{M}(z,t,j) = \sum_N e^{Nz}P_N(t,j)$. Unfortunately, the (central) moments cannot be expressed easily in terms of the (central) moments of the different subprocesses. The derivation of the whole generating function and not of the different subprocesses' generating functions has to be calculated. To circumvent this disadvantage, one can conveniently define quantities commonly referred to as *cumulants*. The cumulant-generating function is given by the logarithm of the moment-generating function

$$\mathcal{S}(z,t) := \ln \mathcal{M}(z,t)\,. \tag{3.8}$$

Again, this function can be expressed in a Taylor series $\mathcal{S}(z,t) = \sum_m C_m(t)z^m/m!$ where the coefficients

$$C_m(t) := \frac{\partial^m}{\partial z^m}\mathcal{S}(z,t)\bigg|_{z=0} \tag{3.9}$$

are denoted as cumulants. However, by means of the recursive formula

$$C_m(t) = \langle N^m\rangle(t) - \sum_{j=1}^{m-1}\binom{m-1}{j-1}C_j(t)\langle N^{m-j}\rangle(t) \tag{3.10}$$

the cumulants can still be expressed by the moments. The first cumulant is the first moment. The second and third cumulant are identical to the corresponding central moment. Beginning with the fourth cumulant, cumulants and (central) moments differ. Due to the logarithm, in the case of separated independent subprocesses, see Eq. (3.7), the cumulant-generating function can be written as a sum of the individual generating functions $\mathcal{S}(z,t) = \sum_j S(z,t,j)$ with $S(z,t,j) = \ln \mathcal{M}(z,t,j)$. Hence, the cumulants

$$C_m(t) = \sum_j C_m(t,j) \tag{3.11}$$

are a sum over the individual subprocess cumulants $C_m(t,j) = \partial_z^m \mathcal{S}(z,t,j)|_{z=0}$.

Another advantage of cumulants can be understood by inspecting the special case of a Gaussian probability distribution

$$P_N(t) = \frac{\vartheta(\mu, e^{-2\pi^2\sigma^2})}{\sigma\sqrt{2\pi}}e^{-\frac{(N-\mu)^2}{2\sigma^2}}\,. \tag{3.12}$$

The Jacobi theta function $\vartheta(x,y) = 1 + 2\sum_{n=1}^{\infty} y^{n^2}\cos(2n\pi x)$ ensures normalization, $\sum_N P_N(t) = 1$. It can be approximated by $\vartheta(\mu, e^{-2\pi^2\sigma^2}) \approx 1$ for $\sigma \gg 1/\sqrt{2\pi}$. In this limit,[2] the generating function is

$$\mathcal{M}(z,t) = e^{\frac{1}{2}\sigma^2 z^2 + \mu z} \tag{3.13}$$

and the cumulants are

$$C_m(t) = \begin{cases} \mu, & m = 1 \\ \sigma^2, & m = 2 \\ 0, & m > 2 \end{cases}. \tag{3.14}$$

Only the first and second cumulant are nonvanishing. In contrast, the central moments are only vanishing for odd m. Noncentral moments $\langle N^m \rangle(t)$ are neither vanishing for even nor odd m. Thus, cumulants are appropriate to measure deviations from Gaussian statistics. Especially the fourth cumulant, called the kurtosis, measures the degree of peakedness in comparison to the Gaussian distribution [59, Section 2.1.2]. A negative (positive) kurtosis implies a distribution with a broader (sharper) peak and thinner (thicker) tails than for the Gaussian distribution, see Figure 3.2.

Finally, we want to mention that cumulants in the limit of long times t can be used to reconstruct characteristic features of an unknown stochastic system, e.g., a lower bound for the system dimension and the full spectrum of relaxation rates as explained in more detail in Chapter 6. However, for this purpose, it is more convenient to apply not the ordinary cumulants but the (generalized) factorial cumulants introduced in the following sections.

3.3 Factorial moments and cumulants

Instead of ordinary moments and ordinary cumulants, factorial moments and factorial cumulants can be used to analyze stochastic processes [21]. These quantities are adapted to integer-valued stochastic variables like the number of tunneled electrons N in the case of full counting statistics. Factorial moments

$$\langle N^{(m)} \rangle(t) := \sum_{N=0}^{\infty} N^{(m)} P_N(t) = \sum_{j=1}^{m} s_1(m,j) \langle N^j \rangle(t) \tag{3.15}$$

are defined by the factorial power $N^{(m)} := N(N-1)\cdots(N-m+1)$ rather than the ordinary power N^m used in Eq. (3.2). The coefficients $s_1(m,j)$ that relate the factorial to the ordinary moments are called the *Stirling numbers* of the first kind. The first three factorial moments take the form

$$\langle N^{(1)} \rangle(t) = \langle N \rangle(t), \tag{3.16}$$

$$\langle N^{(2)} \rangle(t) = \langle N^2 \rangle(t) - \langle N \rangle(t), \tag{3.17}$$

$$\langle N^{(3)} \rangle(t) = \langle N^3 \rangle(t) - 3\langle N^2 \rangle(t) + 2\langle N \rangle(t). \tag{3.18}$$

[2] The limit is already reached for $\sigma = 1$ in good approximation, i.e., the width of the Gaussian distribution is at least on the scale of the discretization of the variable N. Since we discuss the case $N \geq 0$, we furthermore assume that $\mu \gg \sigma$, i.e., the cutoff at $N = 0$ can be neglected.

The factorial-moment generating function is given by

$$\mathcal{M}_{\mathrm{F}}(z,t) := \left\langle (z+1)^N \right\rangle (t) = \sum_{N=0}^{\infty} (z+1)^N P_N(t) \tag{3.19}$$

and yields the factorial moments as derivatives $\langle N^{(m)} \rangle (t) = \partial_z^m \mathcal{M}_{\mathrm{F}}(z,t)|_{z=0}$. Factorial cumulants

$$C_{\mathrm{F},m}(t) := \frac{\partial^m}{\partial z^m} \mathcal{S}_{\mathrm{F}}(z,t)\bigg|_{z=0} = \sum_{j=1}^{m} s_1(m,j) C_j(t) \tag{3.20}$$

are defined via the generating function $\mathcal{S}_{\mathrm{F}}(z,t) := \ln \mathcal{M}_{\mathrm{F}}(z,t)$. They are related to the ordinary cumulants in the same way as the factorial moments to the ordinary moments, cf. Eq. (3.15). The relation can easily be expressed in double-bracket notation [22]

$$C_{\mathrm{F},m} = \langle\langle N^{(m)} \rangle\rangle (t)\,, \tag{3.21}$$

where $\langle\langle \cdots \rangle\rangle$ is defined by the linearity property $\langle\langle \alpha N^m + \beta N^n \rangle\rangle = \alpha \langle\langle N^m \rangle\rangle + \beta \langle\langle N^n \rangle\rangle$ and $\langle\langle N^m \rangle\rangle = C_m$. Thus, the relation of the first three factorial cumulants to the ordinary cumulants is given by Eqs. (3.16) - (3.18) after replacing the brackets with double brackets.

The relation of the factorial cumulants to the factorial moments is given by Eq. (3.10) after the replacements $\langle N^m \rangle (t) \to \langle N^{(m)} \rangle (t)$ and $C_m(t) \to C_{\mathrm{F},m}(t)$.

Just as the ordinary cumulants, the factorial cumulants possess the additive property of individual subprocesses discussed in the previous chapter

$$C_{\mathrm{F},m} = \sum_j C_{\mathrm{F},m}(t,j)\,, \tag{3.22}$$

where $C_{\mathrm{F},m}(t,j) = \partial_z^m \ln \mathcal{M}_{\mathrm{F}}(z,t,j)|_{z=0}$ and $\mathcal{M}_{\mathrm{F}}(z,t,j) = \sum_N (z+1)^N P_N(t,j)$. In contrast to ordinary cumulants, all factorial cumulants are nonvanishing for Gaussian statistics. For the Poisson distribution

$$P_N(t) = \frac{\mu^N}{N!} e^{-\mu}, \quad N \geq 0 \tag{3.23}$$

the generating function of the factorial cumulants takes the form $\mathcal{S}_{\mathrm{F}}(z,t) = \mu z$ and all factorial cumulants, except the first, are vanishing

$$C_{\mathrm{F},m}(t) = \begin{cases} \mu, & m = 1 \\ 0, & m > 1 \end{cases}. \tag{3.24}$$

Thus, factorial cumulants measure deviations from Poisson statistics and *not* Gaussian statistics as ordinary cumulants do.

The factorial moments $\langle N^{(m)} \rangle (t)$ and factorial cumulants $C_{\mathrm{F},m}(t)$ are just linear combinations of ordinary moments $\langle N^m \rangle (t)$ and ordinary cumulants $C_m(t)$, respectively. In a similar way, ordinary moments and ordinary cumulants are completely determined by the corresponding factorial quantities

$$\langle N^m \rangle (t) = \sum_{j=1}^{m} s_2(m,j) \langle N^{(j)} \rangle (t), \tag{3.25}$$

$$C_m(t) = \sum_{j=1}^{m} s_2(m,j) C_{\mathrm{F},j}(t)\,, \tag{3.26}$$

where $s_2(m,j)$ are Stirling numbers of the second kind given by [21, Section 1.1.3]

$$s_2(m,j) = \frac{1}{j!}\sum_{k=0}^{j}(-1)^k\binom{j}{k}(j-k)^m\,. \tag{3.27}$$

Hence, the ordinary quantities up to a certain order m provide the same information as the corresponding factorial quantities up to the same order m. The same information is just presented in two different manners.

If the distribution $P_N(t)$ is nonvanishing only for a finite number of $N = 0, 1\ldots, N_{\text{cutoff}}$, especially factorial quantities are more convenient. Then, the factorial moments of order $m > N_{\text{cutoff}}$ are vanishing. In contrast, the ordinary moments are, in general, nonvanishing independent of m. Correspondingly, many terms in Eq. (3.10) vanish in the former but not in the latter case. Thus, in this scenario, factorial quantities present the information in a more effective manner.

Moreover, factorial cumulants are especially suited to identify correlations between tunneling electrons, as already indicated by their normalization to the Poisson distribution. We elaborate this topic further in the next section.

3.4 Correlations

Suppose a detector counts tunneled electrons. If the electrons tunnel in an uncorrelated manner (i.e., independently from each other), the total probability distribution $P_N(t)$ can be written in the form of Eq. (3.6). Each electron increases the detector counter just by one if it tunnels, otherwise the detector counter remains unchanged. Thus, the probability distributions of each subprocess j is given by $P_1(t,j) = 1 - P_0(t,j) = p_j(t)$ and $P_N(t,j) = 0$ for $N \neq 0, 1$, where $p_j(t)$ is just a shorthand notation for $P_1(t,j)$. Each subprocess is determined by a *Bernoulli distribution*. For the total probability distribution, we obtain the *Poisson binomial distribution*

$$P_N(t) = \sum_{A_N}\prod_{j\in A_N} p_j(t)\prod_{k\in A_N^{\text{c}}}\left[1-p_k(t)\right]\,. \tag{3.28}$$

The sum goes over all subsets A_N of the natural numbers with cardinality N, and A_N^{c} is the complement of A_N. If all events occur with the same probability $p_j(t) = p(t)$, the Poisson binomial distribution becomes the *binomial distribution*. Moreover, in the limit of small probabilities $p_j \ll 1$ the distribution can be approximated [60] by the Poisson distribution defined in Eq. (3.23) with $\mu = \sum_j p_j(t)$.

If the statistics cannot be expressed by a Poisson binomial distribution, at least one subprocess $P_N(t,j)$ of Eq. (3.6) cannot be decomposed into independent single-electron tunneling events (independent Bernoulli distributions). In the following, such a subprocess is denoted as correlated transfer process, or we simply refer to *correlations* between the counted electrons.

The remaining question is how correlated transport processes can be identified easily? One possible procedure is provided by ordinary cumulants. For the Poisson binomial distribution, the generating function of the ordinary moments is

$$\mathcal{M}(z,t) = \prod_j\left[1 - p_j(t) + e^z p_j(t)\right]\,. \tag{3.29}$$

The cumulants can be written in the form [61]

$$C_m(t) = \sum_j \left[p(1-p)\frac{\mathrm{d}}{\mathrm{d}p} \right]^{m-1} p \Big|_{p=p_j(t)} . \tag{3.30}$$

Since the $p_j(t)$ are real and lie in the interval $[0,1]$, the first cumulant $C_1(t) = \sum_j p_j(t)$ and also the second cumulant $C_2(t) = \sum_j p_j(t)[1-p_j(t)]$ are always positive. Moreover, the second cumulant is smaller than the first one. Thus, the ratio $F(t)$ between both cumulants, commonly denoted as *Fano factor*, fulfills

$$0 \leq F(t) = \frac{C_2(t)}{C_1(t)} \leq 1 \tag{3.31}$$

for the Poisson binomial distribution. In the limit of a Poisson distribution, the Fano factor becomes $F(t) = 1$ and is, therefore, called *Poissonian*. For $F(t) < 1$, one refers to a *sub-Poissonian* Fano factor. If the transport is completely deterministic, i.e., each $p_j(t)$ is zero (one) for times smaller (larger) than some clearly defined time point, the Fano factor $F(t) = 0$.[3]

For a different distribution than Eq. (3.28), the first cumulant $C_1(t) = \langle N \rangle (t)$ remains positive taking into account that the detector counter only increases. The second cumulant $C_2(t) = \langle (N - \langle N \rangle)^2 \rangle (t)$ remains also a positive quantity independently of $P_N(t)$. Thus, a negative sign of the Fano factor can never occur. However, *any* value of the Fano factor $F(t) > 1$ for *any* time t indicates correlated electron transport. In this case, the Fano factor is denoted as *super-Poissonian*.

In general, the sign of ordinary cumulants $C_m(t)$ with $m > 2$ can be positive or negative, which leads to the observation of universal oscillations [20]. Thus, the formulation of correlation-detection criteria for higher-order cumulants becomes more challenging. An easier approach is provided by the factorial cumulants.

For the Poisson binomial distribution, the generating function of the factorial moments takes the form

$$\mathcal{M}_{\mathrm{F}}(z,t) = \prod_j \left[1 - p_j(t) + (z+1)p_j(t) \right] \tag{3.32}$$

and the factorial cumulants are

$$C_{\mathrm{F},m}(t) = (-1)^{m-1}(m-1)! \sum_j \left[p_j(t) \right]^m . \tag{3.33}$$

Since the $p_j(t)$ are real and lie in the interval $[0,1]$, the sign of the factorial cumulants is fixed [22, 63]

$$(-1)^{m-1} C_{\mathrm{F},m}(t) \geq 0 . \tag{3.34}$$

Any violation of this sign criterion for *any* time t or order m indicates correlated transport.

[3] If electrons are transferred deterministically, successive intervals of length t in Figure 3.1 contain the same number of tunneled electrons. One refers to *temporal correlation* between successive electrons [62]. However, the probability distribution can still be expressed by a Poisson binomial distribution. These temporal correlations are not the correlations defined in this section.

Since ordinary and factorial cumulants provide the same information, one immediately sees that a violation of the sign criterion for $m = 2$ is equivalent to a super-Poissonian Fano factor

$$-C_{\mathrm{F},2} < 0 \quad \Longleftrightarrow \quad F(t) > 1\,. \tag{3.35}$$

The violation of the sign criterion Eq. (3.34) is a more sensitive tool to detect correlations then solely inspecting the Fano factor. As pointed out for the statistics discussed in Ref. [64] and Chapter 4, factorial cumulants of order $m > 2$ can reveal correlations while the Fano factor fails $F \leq 1$. To analyze the sensitivity of the sign criterion (3.34), we inspect the factorial cumulants in more detail in the following.

In an actual counting experiment, see Chapter 2, the total number of counts is always finite since a measurement can be performed only over a limited time span. Thus, the number of transferred electrons N is always limited by some finite but large cutoff N_{cutoff}. The resulting generating function $\mathcal{M}_{\mathrm{F}}(z,t)$ is a polynomial of finite order with zeros $z_j(t)$, i.e., $\mathcal{M}_{\mathrm{F}}(z_j(t),t) = 0$, being either real or appearing as conjugate complex pairs. The generating function can be written in the form $\mathcal{M}_{\mathrm{F}}(z,t) = \mathcal{M}_{\mathrm{F}}(0,t)\prod_j [1 - z/z_j(t)]$. Multiple zeros appear with corresponding multiplicity in the product. If we define $\widetilde{p}_j(t) := -1/z_j(t)$ and take the normalization $\mathcal{M}_{\mathrm{F}}(0,t) = 1$ into account, we obtain

$$\mathcal{M}_{\mathrm{F}}(z,t) = \prod_j \left[1 - \widetilde{p}_j(t) + (z+1)\widetilde{p}_j(t)\right]\,. \tag{3.36}$$

The generating function acquires the form of Eq. (3.32) and the factorial cumulants

$$C_{\mathrm{F},m}(t) = (-1)^{m-1}(m-1)!\sum_j [\widetilde{p}_j(t)]^m \tag{3.37}$$

resemble Eq. (3.33). However, only if all the $\widetilde{p}_j(t)$ are real and lie in the interval $[0,1]$, i.e., the zeros $z_j(t) \in (-\infty,-1]$, the case of the Poisson binomial distribution is recovered and no correlated transfer processes are present. If at least one subprocess transfers multiple electrons in a correlated manner, $\widetilde{p}_j(t)$ can be < 0 or > 1 or pairs of complex-valued $\widetilde{p}_j(t)$ appear.

The sum in Eq. (3.37) can be written in the form $\sum_j \widetilde{p}_j^m = \sum_j |\widetilde{p}_j|^m \cos\left[m \arg(\widetilde{p}_j)\right]$. Deviations of $\arg(p_j)$ from 0 are amplified by the multiplication with m such that $\cos\left[m\arg(\widetilde{p}_j)\right]$ can become negative and the sign criterion is violated. In this sense, we see that higher-order factorial cumulants can detect correlations while lower-order cumulants fail.

By inspecting Eq. (3.37), we also see that those $\widetilde{p}_j(t)$ with the largest absolute values dominate the complete sum. Moreover, in the limit $m \gg 1$, the sum can even be approximated by the single $\widetilde{p}_j(t)$ or complex conjugated pair of $\widetilde{p}_j(t)$ with the largest absolute value. Thus, factorial cumulants are only sensitive to processes decomposed into these $\widetilde{p}_j(t)$. Other transfer processes are not recognized by factorial cumulants, although they may even transfer multiple electrons in a correlated manner.

To amplify the sensitivity for correlations further and enable the study of arbitrary $\widetilde{p}_j(t)$ separately, we introduce *generalized factorial cumulants* in the next chapter.

3.5 Generalized factorial moments and cumulants

On the basis of the factorial moments and cumulants we introduce in this section generalized factorial moments and cumulants. For the generalization, we effectively shift the counting variable z along the real axis by the amount $s-1$. In this sense, we define the generating function of the generalized factorial moments as

$$\mathcal{M}_s(z,t) := \sum_{N=0}^{\infty} (z+s)^N P_N(t)\,, \tag{3.38}$$

where s is a real parameter. The generalized factorial moments are defined as

$$M_{s,m}(t) := \frac{\partial^m}{\partial z^m}\mathcal{M}_s(z,t)\bigg|_{z=0} = \frac{\partial^m}{\partial z^m}\mathcal{M}_0(z,t)\bigg|_{z=s} = \sum_{N=0}^{\infty} N^{(m)} s^{N-m} P_N(t) \tag{3.39}$$

and the generalized factorial cumulants as

$$C_{s,m}(t) := \frac{\partial^m}{\partial z^m}\ln\mathcal{M}_s(z,t)\bigg|_{z=0} = \frac{\partial^m}{\partial z^m}\ln\mathcal{M}_0(z,t)\bigg|_{z=s}\,. \tag{3.40}$$

For $s=1$, the factorial generating function $\mathcal{M}_1(z,t)=\mathcal{M}_{\mathrm{F}}(z,t)$ is recovered and, thus, $M_{1,m}(t)=\langle N^{(m)}\rangle$ and $C_{1,m}(t)=C_{\mathrm{F},m}(t)$.[4]

By comparing Eq. (3.38) with Eq. (3.19), we see that the zeros of $\mathcal{M}_s(z,t)$ and $\mathcal{M}_{\mathrm{F}}(z,t)$ differ just by the amount $s-1$. Thus, following the argumentation that has led to Eq. (3.36), we obtain

$$\mathcal{M}_s(z,t) = \mathcal{M}_s(0,t)\prod_j\left[1-\frac{1}{-z_j(t)+s-1}+(z+1)\frac{1}{-z_j(t)+s-1}\right] \tag{3.41}$$

and the generalized factorial cumulants ($m>0$) become

$$C_{s,m}(t) = (-1)^{m-1}(m-1)!\sum_j\left[\frac{1}{-z_j(t)+s-1}\right]^m\,. \tag{3.42}$$

If electron transport is uncorrelated, the zeros are $z_j(t)=-1/p_j(t)$ and, therefore, lie in the interval $(-\infty,-1]$. Hence, for $s\geq 0$, the denominators $-z_j(t)+s-1$ are always positive and the sign of the generalized factorial cumulants is fixed

$$(-1)^{m-1}C_{s,m}(t)\geq 0\,. \tag{3.43}$$

[4] In this thesis, we define the generating function without a normalization factor $1/\mathcal{M}_s(0,t)$. Taking the normalization factor into account, the generalized factorial moments can be rewritten as

$$M_{s,m}(t) = \sum_{N=m}^{\infty} N^{(m)} s^{N-m} P_N(t) \Big/ \sum_{N=0}^{\infty} s^N P_N(t)\,.$$

For $s=0$, $M_{0,m}(t)=m!P_m(t)/P_0(t)$. A z-independent normalization factor does not influence the cumulants of order $m>0$, but it would set, per definition, $M_{s,0}(t)=1$ and $C_{s,0}=0$. Moreover, the relation of the cumulants to the moments would be given by Eq. (3.10) after the replacements $\langle N^m\rangle(t)\to M_{s,m}(t)$ and $C_m(t)\to C_{s,m}(t)$.

If $s < 0$, this sign criterion still holds for all even orders m. A violation of this criterion for any time t, order m, or real s indicates correlations.[5]

The sum in Eq. (3.42) can be rewritten to obtain

$$C_{s,m}(t) = (-1)^{m-1}(m-1)! \sum_j \frac{\cos\{m \arg[-z_j(t)+s-1]\}}{|-z_j(t)+s-1|^m} \,. \tag{3.44}$$

Deviations of $\arg[-z_j(t)+s-1]$ from zero can be amplified by changing the parameter s such that the sign criterion can become violated. For doing so, it is more likely that s must be decreased than increased. The reason is that zeros in the complex plane are usually close to the interval $(-\infty, -1]$. The sensitivity for correlations can be increased tremendously as illustrated in Chapter 4.

More importantly, the sum in Eq. (3.44) is dominated by the zeros yielding the smallest absolute value $|-z_j(t)+s-1|$. Thus, by varying the parameter s different zeros, i.e., different processes, can be brought into focus. Especially, processes can be studied which are hidden to ordinary and factorial cumulants. In Chapter 4, we detect correlations just because we obtain access to these hidden processes. In Chapter 6, we find additional dimensions and relaxation rates. Finally, coherent oscillations are uncovered in Chapter 7.

3.6 Full counting statistics for Coulomb-blockade systems

In the next chapters, we consider charge transport through Coulomb-blockade systems which can be simulated by means of a *master equation*

$$\dot{p}^\chi(t) = \sum_{\chi'} [\Gamma_{\chi\chi'} p^{\chi'}(t) - \Gamma_{\chi'\chi} p^\chi(t)] \,. \tag{3.45}$$

A central region, e.g., an island or quantum dot, is weakly tunnel coupled to some electronic reservoirs. In the following, we refer to the central region simply as the "dot". The system is characterized by the different probabilities $p^\chi(t)$ that the dot is in state χ. Each state is determined by the electron number (charge) on the dot, but also other microscopic attributes like the occupied orbitals or the adopted spin can be relevant. Coherent superpositions between different states χ are not taken into account here. They are only relevant in Chapter 7 and will be discussed separately there. Thus, to be precise, the system can be characterized by the finite-dimensional, diagonal, and reduced density matrix of the dot.

The reservoirs' degrees of freedom enter only effectively via the transition rates $\Gamma_{\chi\chi'}$ from state χ' to χ. These rates account for the stochastic appearance of tunneling events between the dot and the reservoirs. The rates are time independent, i.e., memory effects (non-Markovian effects) [13, 15, 65] are not taken into account. The first term of the master equation $\sum_{\chi'} \Gamma_{\chi\chi'} p^{\chi'}(t)$ describes the probability current into state χ, whereas the second term $\sum_{\chi'} \Gamma_{\chi'\chi} p^\chi(t)$ the probability flow out of state χ. Starting at arbitrary initial probabilities $p^\chi(0)$, the system approaches stationary (i.e., time independent) probabilities p^χ_{stat} determined by

$$0 = \sum_{\chi'} [\Gamma_{\chi\chi'} p^{\chi'}_{\text{stat}} - \Gamma_{\chi'\chi} p^\chi_{\text{stat}}] \,, \tag{3.46}$$

[5] In Chapter 5, we extend criterion (3.43) and find additional conditions which have to be fulfilled in the short-time limit.

where the total probability flow into and out of a state χ compensate each other. The probability flow in the stationary limit is discussed in more detail in Chapter 8 dealing with the violation of *detailed balance*.

To include the detector, counting the number $N \geq 0$ of transferred electrons in time interval $[0,t]$, we replace the master equation for $p^\chi(t)$ by an N-resolved version for $p_N^\chi(t)$

$$\dot{p}_N^\chi(t) = \sum_{\chi'} \sum_k d_{\chi\chi'}^k \Gamma_{\chi\chi'} p_{N-k}^{\chi'}(t) - \sum_{\chi'} \Gamma_{\chi'\chi} p_N^\chi(t)\,. \tag{3.47}$$

The coupling constant $d_{\chi\chi'}^k$ is 1 if the detector counter is increased by $k \geq 0$ for the transition from χ' to χ and otherwise 0.

Note that in contrast to $p^\chi(t)$, for $p_N^\chi(t)$ also tunneling processes with rate $\Gamma_{\chi\chi}$ can be relevant, where the system ends up in the same state χ as it started. This is, e.g., the case for cotunneling through a magnetic atom [66]. However, these processes are not recognized by detectors like the single-electron transistor or the quantum point contact introduced in Section 2.3 and, therefore, are not dealt with in this thesis.[6] Such detectors recognize only electrons leaving or entering the dot if the charge on the dot changes during the transition from χ' to χ. Differences in the counting statistics of tunneling in and out electrons indicate a violation of detailed balance as explained in Chapter 8. However, in the remaining part of this thesis, we decide to count the electrons leaving the dot.

Solving the N-resolved master equation for the probabilities $p_\chi^N(t)$ yields the distribution $P_N(t) = \sum_\chi p_\chi^N(t)$. It is then straightforward to calculate the moments and cumulants defined in the previous chapters. However, solving the N-resolved master equation for many different values of N can be very challenging. A more elegant procedure is to first perform a z-transform of Eq. (3.47), i.e., multiply with z^N and then sum over N. If we combine the z-transformed N-resolved probabilities $p_z^\chi = \sum_N z^N p_N^\chi$ of the different states χ in a vector $\mathbf{p}_z(t)$, the z-transformed master equation can be written in the form

$$\dot{\mathbf{p}}_z(t) = \mathbf{W}_z \mathbf{p}_z(t)\,, \tag{3.48}$$

with matrix elements

$$(\mathbf{W}_z)_{\chi\chi'} = \sum_k z^k d_{\chi\chi'}^k \Gamma_{\chi\chi'} - \delta_{\chi\chi'} \sum_{\chi''} \Gamma_{\chi''\chi'}\,. \tag{3.49}$$

In the following, we call the matrix $\mathbf{W}_z$ the *generator* of the system's dynamics. The formal solution of Eq. (3.48) is

$$\mathbf{p}_z(t) = e^{\mathbf{W}_z t} \mathbf{p}_z(0). \tag{3.50}$$

The matrix exponential $e^{\mathbf{W}_z t}$ can be calculated by means of the right and left eigenvectors

$$\mathbf{W}_z \mathbf{r}_{z,j} = \lambda_j(z) \mathbf{r}_{z,j}\,, \quad \mathbf{l}_{z,j}^T \mathbf{W}_z = \lambda_j(z) \mathbf{l}_{z,j}^T\,, \tag{3.51}$$

yielding, after a proper normalization, the identity $\mathbf{1} = \sum_{j=1}^M \mathbf{r}_{z,j} \mathbf{l}_{z,j}^T$. Thus, we can write

$$e^{\mathbf{W}_z t} = \sum_{j=1}^M e^{\lambda_j(z) t} \mathbf{r}_{z,j} \mathbf{l}_{z,j}^T\,, \tag{3.52}$$

[6] Nevertheless, for completeness, we include the possibility of the detection of these processes in the inverse-counting-statistics procedure introduced in Chapter 6.

where M is the number of different states χ and each $\lambda_j(z)$ is an eigenvalue of $\mathbf{W}_z$. For real z, the eigenvalues are either real or appear as complex-conjugates pairs since the probability vector $\mathbf{p}_z(t)$ is also real. For $z = 1$, the vector $\mathbf{p}_z$ includes probabilities where the detector's degrees of freedom have been traced out, $p_1^\chi = \sum_N p_N^\chi$. Then, Eq. (3.48) is nothing but the master equation (3.45) and Eq. (3.50) its solution.

The eigenvalues $\lambda_j(1)$ determine the exponential relaxation from arbitrary initial probabilities to the stationary probabilities. Therefore, $\lambda_j(1)$ are called the *relaxation rates* of the system [67–72]. The eigenvalues $\lambda_j(z)$ play an important role for the inverse counting statistics discussed in the Chapter 6.

For $t = 0$, the detector counter is still zero, i.e., $p_N^\chi(0) = p^\chi(0)\,\delta_{N,0}$. Therefore, the initial vector $\mathbf{p}_z(0)$ is z-independent and determined solely by the initial probabilities $p^\chi(0)$. In the following, we assume that electron counting starts only after the system has reached its stationary limit, i.e., $p^\chi(0) := p_{\text{stat}}^\chi$. If we arrange the stationary probabilities in the vector $\mathbf{p}_{\text{stat}}$, we can write Eq. (3.46) in the form $\mathbf{W}_1\mathbf{p}_{\text{stat}} = \mathbf{0}$ with $\mathbf{e}^T\mathbf{p}_{\text{stat}} = 1$. We defined $\mathbf{e}^T = (1, \ldots, 1)$ to sum over all states χ in $\mathbf{p}_{\text{stat}}$.

Finally, we obtain the generating function of the generalized factorial moments

$$\mathcal{M}_s(z,t) = \mathbf{e}^T e^{\mathbf{W}_{z+s}\,t}\mathbf{p}_{\text{stat}} = \sum_{j=1}^{M} \left(\mathbf{e}^T\mathbf{r}_{z+s,j}\right)\left(\mathbf{l}_{z+s,j}^T\,\mathbf{p}_{\text{stat}}\right) e^{\lambda_j(z+s)t}\,. \tag{3.53}$$

If we replace $z + s$ by $\exp(z)$, Eq. (3.53) yields the generating function $\mathcal{M}(z,t)$ of the ordinary moments.

Within this procedure, it has not been necessary to calculate the probability distribution $P_N(t)$. However, the distribution can be obtained, e.g., via the inverse Laplace transform of $\mathcal{M}(z,t)$, cf. Eq. (3.4). An easier approach is to calculate the generalized factorial moments for $s = 0$ from Eq. (3.53). Taking Eq. (3.38) into account, we obtain the probability distribution via

$$P_N(t) = \frac{M_{0,N}}{N!}\,. \tag{3.54}$$

4 Detection of correlations via generalized factorial cumulants

In this chapter, we illustrate the sensitivity of generalized factorial cumulants to detect correlations by means of two example systems.

Some of the most common quantities used to study the statistics of electron tunneling are the current $\langle I \rangle = \lim_{t\to\infty} C_1(t)/t$ and the zero-frequency current noise $S(0) = \lim_{t\to\infty} 2\,C_2(t)/t$. In particular, a super-Poissonian Fano factor $F = S(0)/(2\,\langle I \rangle) > 1$ is a clear signature of the presence of correlations. In various scenarios, a super-Poissonian Fano factor of the electron tunneling has been predicted theoretically [73–79] or observed experimentally [80–86]. However, the presence of correlations does not always imply a super-Poissonian Fano factor.

Two example systems consisting of a quantum dot coupled to electronic reservoirs are presented in Section 4.1. The quantum dot is either subjected to a Zeeman field and coupled to a single reservoir (Section 4.2) or not subjected to a Zeeman field, but coupled to two ferromagnetic reservoirs (Section 4.3). The former case is a non-voltage biased scenario, whereas in the latter case a bias voltage is applied such that electrons are transferred unidirectionally from the source to the drain electrode.

In Section 4.2, we discuss for which time intervals t and system parameters electrons tunnel in a correlated manner. In many cases the Fano factor fails to detect these correlations. Applying higher-order factorial cumulants, see Chapter 3.4, reveals correlations in a successively increasing area of the parameter space. Utilizing generalized factorial cumulants enhances dramatically the sensitivity for correlations.

In Section 4.3, the discussion is repeated for the second example system. Again, the sensitivity for correlations increases dramatically if generalized factorial cumulants are applied. Moreover, we identify parameter regimes where generalized factorial cumulants detect correlations, but the Fano factor and all the ordinary factorial cumulants fail.

The results of this chapter have been published, in parts verbatim, in Ref. [63].

4.1 Model of the single-level quantum dot

In this and the following chapters, we illustrate our theoretical findings for the example of a single-level quantum dot either in a non-voltage or voltage-biased situation. The set-up and corresponding single-electron energy levels are depicted in Figs. 4.1 and 4.2 (a), (b). The former case is a realization of the single-electron box (SEB) and the latter a realization of the single-electron transistor (SET), cf. Chapter 2. The system is described by the full

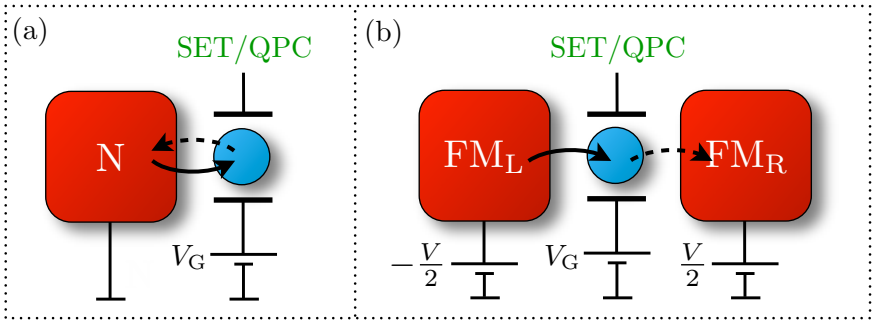

Figure 4.1: (a) Single-electron box (SEB) and (b) single-electron transistor (SET) realized by a single-level quantum dot (blue). In (a), the dot is weakly tunnel coupled to a normal-metal lead (red) and subjected to a Zeeman field. In (b), electrons are transferred in a unidirectional fashion from the left to the right ferromagnetic lead. Electrons leaving the dot are counted by a detector SET or QPC (green).

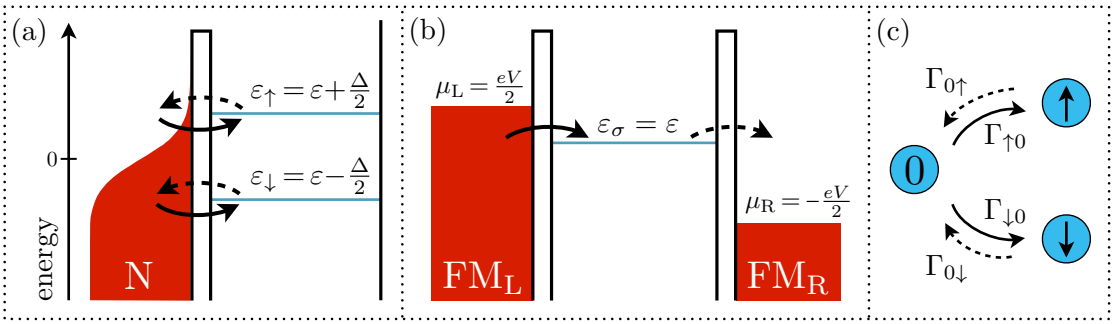

Figure 4.2: Single-electron energy levels of (a) the SEB and (b) the SET depicted in Figure 4.1. (c) Sketch of the states and transition rates. Dashed lines indicate transitions counted by the detector.

Hamiltonian

$$H = \sum_r H_r + H_{\text{dot}} + H_{\text{tun}} \tag{4.1}$$

containing one part for the leads, quantum dot, and the electron tunneling, respectively. Each lead is modeled as reservoir of noninteracting electrons at electrochemical potential μ_r. For the SEB, only one normal-metal lead must be accounted for with $r = \text{N}$. All other relevant energies will be measured relative to μ_N and therefore we choose $\mu_\text{N} = 0$. For the SET, an applied bias voltage V yields the electrochemical potentials $\mu_\text{L} = eV/2 > 0$ and $\mu_\text{R} = -eV/2 < 0$ for the left and right lead. The Hamiltonian of lead r reads

$$H_r = \sum_{\mathbf{k}\sigma} \varepsilon_{r\mathbf{k}\sigma} a^\dagger_{r\mathbf{k}\sigma} a_{r\mathbf{k}\sigma} \,. \tag{4.2}$$

The operator $a^\dagger_{r\mathbf{k}\sigma}$ ($a_{r\mathbf{k}\sigma}$) creates (annihilates) an electron with momentum $\mathbf{k}$ and either majority ($\sigma = +$) or minority spin ($\sigma = -$). Only for a ferromagnetic lead, the energy levels $\varepsilon_{r\mathbf{k}\sigma}$ depend on the spin index σ and we obtain a spin-dependent density of states $\rho_{r\sigma}$. Since the density of states varies on the scale of the conduction band (eV) but μ_r is only varied on the meV-scale, we can assume that $\rho_{r\sigma}$ is energy independent. The degree of the lead's spin polarization is parametrized by $p_r = (\rho_{r+} - \rho_{r-})/(\rho_{r+} + \rho_{r-})$.

The Hamiltonian of the single-level quantum dot is

$$H_{\mathrm{dot}} = \sum_{\sigma} \varepsilon_{\sigma} c_{\sigma}^{\dagger} c_{\sigma} + U c_{\uparrow}^{\dagger} c_{\uparrow} c_{\downarrow}^{\dagger} c_{\downarrow} \,. \tag{4.3}$$

The operator $c_{\sigma}^{\dagger}$ (c_{σ}) creates (annihilates) an electron with spin $\sigma =\uparrow,\downarrow$ on the quantum dot. The first term is the energy needed to occupy the single-particle energy-levels $\varepsilon_{\sigma} = \varepsilon \pm \Delta/2$, where ε is the mean energy level tunable by the gate voltage V_{G}. If the dot is subjected to a Zeeman field, spin degeneracy is lifted by the amount Δ. The second term accounts for the Coulomb energy U necessary to bring both electrons on the quantum dot. The Coulomb energy U is twice the charging energy defined in Section 2.1, i.e., $U = 2E_C$. The eigenstates $|\chi\rangle$ of the dot Hamiltonian are $\chi = 0$ for zero excess electrons on the quantum dot, $\chi =\uparrow (\downarrow)$ for a single electron with spin $\uparrow$ ($\downarrow$) on the dot, and $\chi = \mathrm{d}$ for the doubly occupied dot.

The tunneling of electrons between the dot and the leads is described by the tunneling Hamiltonian

$$H_{\mathrm{tun}} = \sum_{r\mathbf{k}} t_r \left(a_{r\mathbf{k}+}^{\dagger}, a_{r\mathbf{k}-}^{\dagger} \right) D^{1/2}(\alpha,\beta,\gamma) \begin{pmatrix} c_{\uparrow} \\ c_{\downarrow} \end{pmatrix} + \mathrm{H.c.} \,, \tag{4.4}$$

with the spin-1/2 rotation matrix [87, Chapter 13] connecting the spin-quantization axis of the lead r and the dot

$$D^{1/2}(\alpha,\beta,\gamma) = \begin{pmatrix} \cos\left(\frac{\beta}{2}\right) e^{-\frac{i}{2}(\alpha+\gamma)} & -\sin\left(\frac{\beta}{2}\right) e^{-\frac{i}{2}(\alpha-\gamma)} \\ \sin\left(\frac{\beta}{2}\right) e^{\frac{i}{2}(\alpha-\gamma)} & \cos\left(\frac{\beta}{2}\right) e^{\frac{i}{2}(\alpha+\gamma)} \end{pmatrix}. \tag{4.5}$$

The tunnel matrix elements t_r can be expressed by the tunnel-coupling strength $\Gamma_{r\pm} = 2\pi|t_r|^2\rho_{r\pm} = (1 \pm p_r)\Gamma_r$, which is related to the average tunnel-coupling strength $\Gamma_r = \sum_{\sigma} \Gamma_{r\sigma}/2$. For normal leads ($p_r = 0$) or ferromagnetic leads ($p_r \neq 0$) with collinear magnetizations (Chapters 4, 6, 8), we choose the same spin-quantization axis for each lead and the dot. Then, the three Euler angles are $\alpha = \beta = \gamma = 0$ and the rotation matrix becomes the identity matrix. In Chapter 7, we will have to deal with nonvanishing Euler angles.

The tunnel-coupling strength Γ_r is weak such that a detector (cf. Chapter 2) has enough time to clearly measure the number of electrons on the quantum dot.[1] Thus, the electron tunneling dynamics resulting from the full Hamiltonian H can be conveniently described by the N-resolved master equation

$$\begin{aligned} \dot{p}_N^0(t) &= -\left(\Gamma_{\uparrow 0} + \Gamma_{\downarrow 0}\right) p_N^0(t) + \Gamma_{0\uparrow} p_{N-1}^{\uparrow}(t) + \Gamma_{0\downarrow} p_{N-1}^{\downarrow}(t) \,, \\ \dot{p}_N^{\uparrow}(t) &= \Gamma_{\uparrow 0} p_N^0(t) - \Gamma_{0\uparrow} p_N^{\uparrow}(t) \,, \\ \dot{p}_N^{\downarrow}(t) &= \Gamma_{\downarrow 0} p_N^0(t) - \Gamma_{0\downarrow} p_N^{\downarrow}(t), \end{aligned} \tag{4.6}$$

to leading order in Γ_r. The master equation is visualized in Figure 4.2 (c). The Coulomb interaction U is assumed to be so large that double occupation of the dot is forbidden. The detector counts the electrons which leave the quantum dot in the time interval $[0, t]$. Electrons entering the dot are not counted. The transition rates $\Gamma_{\chi\chi'}$ from state χ' to χ

[1] Weak tunneling corresponds to $\hbar\Gamma \ll k_{\mathrm{B}}T$, see Ref. [88, Section 4.6].

are calculated from Fermi's golden rule [24, Section 10.2.2] or, alternatively, by applying diagrammatic rules [89–93]. The probability vector $\mathbf{p}_z = (p_z^0, p_z^\uparrow, p_z^\downarrow)^T$ is determined by the generator

$$\mathbf{W}_z = \begin{pmatrix} -\Gamma_{\uparrow 0} - \Gamma_{\downarrow 0} & z\Gamma_{0\uparrow} & z\Gamma_{0\downarrow} \\ \Gamma_{\uparrow 0} & -\Gamma_{0\uparrow} & 0 \\ \Gamma_{\downarrow 0} & 0 & -\Gamma_{0\downarrow} \end{pmatrix} . \tag{4.7}$$

Each counting factor z in the upper-right off-diagonal matrix elements correspond to counting an electron leaving the dot.

4.2 Single-level quantum dot with Zeeman field

First, we consider the not voltage-biased scenario: a quantum dot coupled to a single normal lead, see Figs. 4.1 (a) and 4.2 (a). The transition rates take the form

$$\Gamma_{\sigma 0} = \Gamma f(\varepsilon_\sigma) , \tag{4.8}$$
$$\Gamma_{0\sigma} = \Gamma \left[1 - f(\varepsilon_\sigma)\right] , \tag{4.9}$$

with the tunnel-coupling strength Γ. The Fermi function $f(\varepsilon) = \{1 + \exp[(\varepsilon - \mu_\mathrm{N}/k_\mathrm{B}T]\}^{-1}$ gives the probability that an energy level ε in the lead is occupied by one electron. The energy ε is measured relative to the electrochemical potential of the lead and therefore we set $\mu_\mathrm{N} = 0$. As unit of energy and time, we choose $k_\mathrm{B}T$ and $1/\Gamma$, respectively.

For a vanishing Zeeman field, $\Delta = 0$, the counted electrons tunnel in an uncorrelated manner since the Coulomb interaction as source of correlations drops effectively out. The model can be mapped onto a noninteracting one in which a single, spin-less quantum-dot level ($\chi = 0, 1$) is filled with rate $\Gamma_{10} := \Gamma_{\uparrow 0} + \Gamma_{\downarrow 0}$ and emptied with rate $\Gamma_{01} := \Gamma_{0\uparrow} = \Gamma_{0\downarrow}$.[2] As a consequence, all zeros $z_j(t)$ of $\mathcal{M}_\mathrm{F}(z,t)$ lie in the interval $(-\infty, -1]$ and Eq. (3.43) holds. More details are given in Appendix A.2.1.

For a finite Zeeman field, $\Delta \neq 0$, the zeros of $\mathcal{M}_s(z,t)$ remain in $(-\infty, -1]$ for short times, see Figure 4.3 (a). However, after a minimal time span t_min, which depends on the system parameters and can be larger or smaller than $1/\Gamma$, the first pair of zeros moves from $(-\infty, -1]$ into the complex plane, see Figure 4.3 (b). Beyond this time, the presence of correlations can be detected from the full counting statistics, as we will detail in the following.[3]

In Figure 4.4 (a), we show the factorial cumulants ($s = 1$) as a function of time for fixed values of $\varepsilon/k_\mathrm{B}T$ and $\Delta/k_\mathrm{B}T$. For the first four factorial cumulants, Eq. (3.43) holds. Especially, the second factorial cumulant, i.e., the commonly known Fano factor, see Eq. (3.35), is not sufficient to detect correlations. A sign change can be observed only for higher orders m, which indicates the presence of correlations. With increasing m, the time at which the sign change occurs decreases and approaches t_min. However, when considering

[2] Although the rate Γ_{10} is larger than Γ_{01}, the net charge current between lead and dot is zero since $\Gamma_{10}\, p_\mathrm{stat}^{\chi=0} = \Gamma_{01}\, p_\mathrm{stat}^{\chi=1}$.

[3] As will be discussed in Section 5.2, for Coulomb-blockade systems with two charge states connected by sequential-tunneling transitions, $t_\mathrm{min} > 0$. In the case of more charge states, the minimal time span can also be $t_\mathrm{min} = 0$.

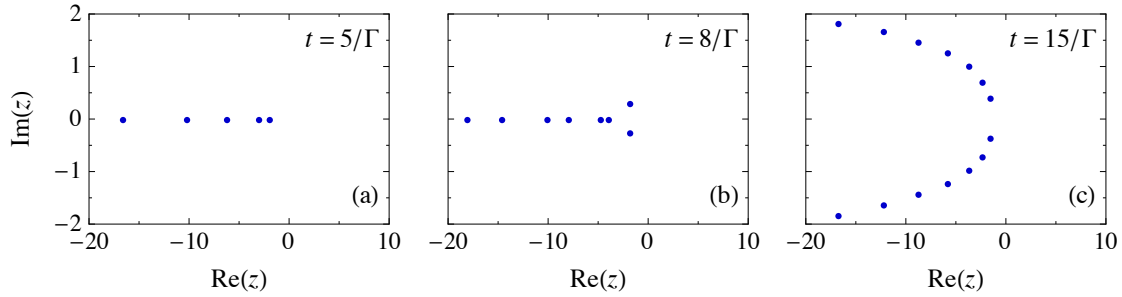

Figure 4.3: Zeros z_j for a single-level quantum dot subject to a Zeeman field with $\Delta = k_\mathrm{B}T/2$, $\varepsilon = -\Delta$, and times $t = 5/\Gamma, 8/\Gamma, 15/\Gamma$. For times $t \leq t_\mathrm{min} \approx 6.83/\Gamma$, the zeros remain in $(-\infty, -1]$. For $t > t_\mathrm{min}$, zeros leave $(-\infty, -1]$ into the complex plane and correlations can be detected by generalized factorial cumulants.

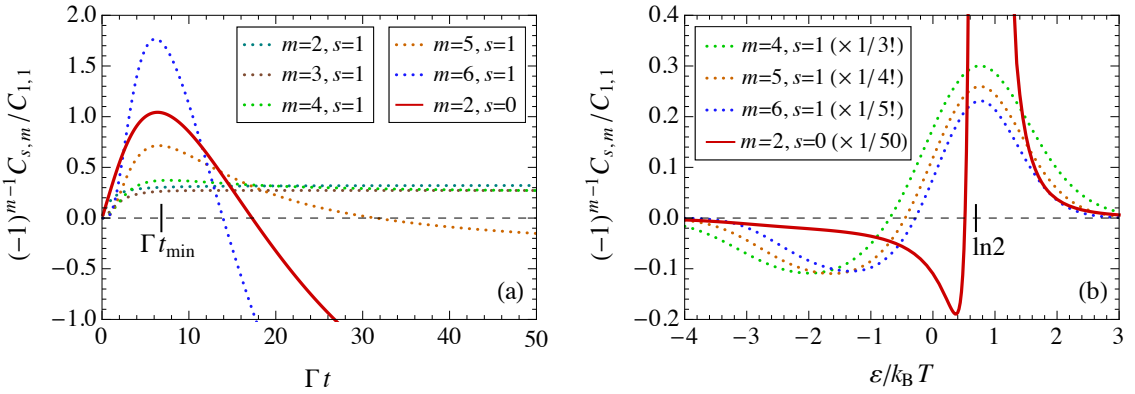

Figure 4.4: (Generalized) factorial cumulant $C_{s,m}$ normalized by $C_{1,1} = C_1 = \langle N \rangle > 0$ for a single-level quantum dot subject to a Zeeman field as a function of (a) time t and (b) dot-level energy ε. The parameters are $\Delta = k_\mathrm{B}T/2$ and (a) $\varepsilon = -\Delta$ or (b) $t = 100/\Gamma$. Negative values of $(-1)^{m-1}C_{s,m}(t)$ indicate the presence of correlations. Correlations can be detected (a) for times larger than $t_\mathrm{min} \approx 6.83/\Gamma$ and (b) for level positions $\varepsilon \lesssim k_\mathrm{B}T \ln 2$.

generalized factorial cumulants, already the cumulant $C_{0,2}(t)$ of second order violates the sign criterion Eq. (3.43).

In Figure 4.4 (b), the gate-voltage dependence of the factorial cumulants is depicted. We find that the criterion Eq. (3.43) is violated for low-lying level energies ε, indicating that correlations are more important in the regime when both spin states in the quantum dot have a finite occupation probability. Again, by decreasing from $s = 1$ to $s = 0$, already for $m = 2$ correlations can be identified.

Figure 4.5 (a) illustrates the possibility to detect correlations via different generalized factorial cumulants. To the right of the dashed line, cf. Appendix A.2.2, given by

$$\frac{\varepsilon}{k_\mathrm{B}T} = \ln 2 + \frac{1}{72}\left(\frac{\Delta}{k_\mathrm{B}T}\right)^2 + \mathcal{O}\left(\frac{\Delta}{k_\mathrm{B}T}\right)^4, \tag{4.10}$$

all zeros $z_j(t)$ remain in the interval $(-\infty, -1]$, see Figure 4.6 (c). The minimal time span t_min is infinite, see Figure 4.5 (b). Therefore, a violation of the sign criterion Eq. (3.43)

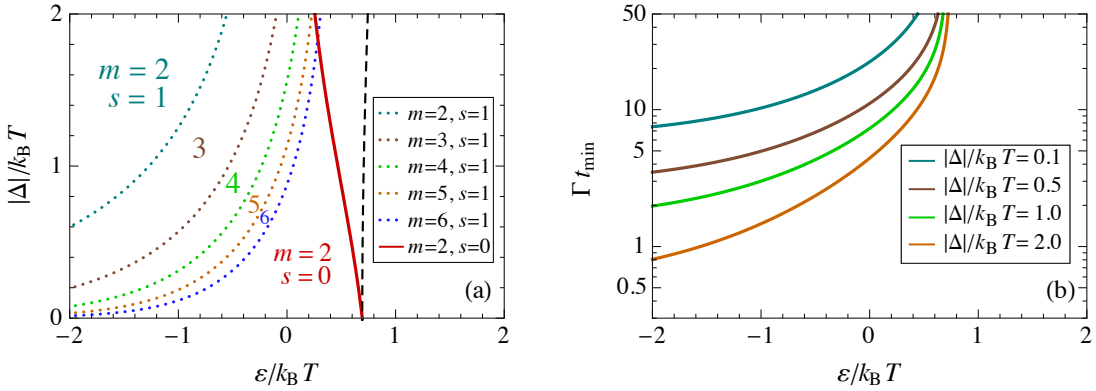

Figure 4.5: Parameter space (a) and minimal time span $t_{\min}$ (b) of a single-level quantum dot subject to a Zeeman field. (a) To the left of the colored lines, the sign criterion for the respective $C_{s,m}(t)$ is violated at some time t. To the right of the dashed line, $\mathcal{M}_{\mathrm{F}}(z,t)$ has only real zeros in $(-\infty,-1]$ and the sign criterion cannot be violated. (b) Minimal time span $t_{\min}$ increases with increasing ε and decreasing $|\Delta|$. It diverges if ε encloses the values of the dashed line in (a). For fixed ε, it diverges if Δ is tuned to zero.

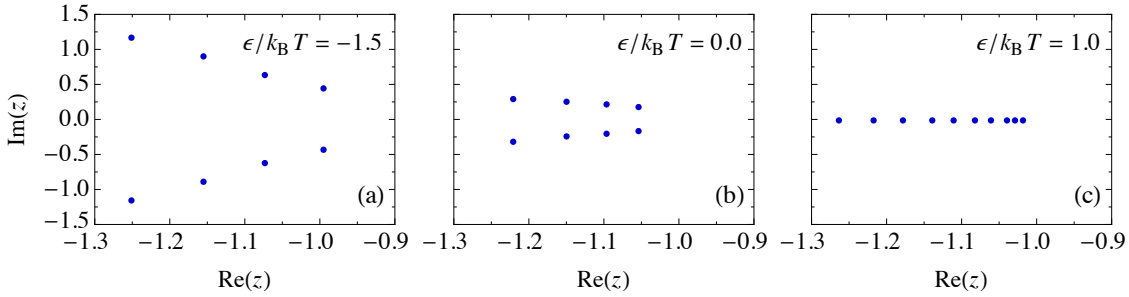

Figure 4.6: Zeros z_j for a single-level quantum dot subject to a Zeeman field with $\Delta = k_{\mathrm{B}}T/2$, $t = 100/\Gamma$, and $\varepsilon/k_{\mathrm{B}}T = -1.5, 0.0, 1.0$. For $\varepsilon/k_{\mathrm{B}}T \lesssim \ln 2$, zeros leave $(-\infty,-1]$ into the complex plane after some time and correlations can be detected by generalized factorial cumulants.

and thus a detection of correlations is only possible for $\varepsilon \lesssim k_{\mathrm{B}}T \ln 2$. The second-order factorial cumulant, $s = 1$ and $m = 2$, violates Eq. (3.43) only for rather large values of the Zeeman energy and a low-lying quantum-dot level. With increasing m, the region in which correlations can be detected is gradually increased to lower Zeeman splitting $|\Delta|$ and larger level positions ε. For generalized factorial cumulants with $s = 0$, already the second order, $m = 2$, covers a much larger region of violation of Eq. (3.43). This clearly demonstrates the enhanced sensitivity of generalized factorial cumulants to the presence of correlations.

4.3 Single-level quantum dot with ferromagnetic leads

As a second example, see Figs. 4.1 (b) and 4.2 (b), we consider a spin-degenerate quantum dot ($\Delta = 0$ and $\varepsilon_\sigma = \varepsilon$) in a voltage-biased scenario. The dot is coupled to a left and right ferromagnetic lead $r = \mathrm{L}$, R with parallel magnetizations and tunnel coupling strengths Γ_r. Each ferromagnet is characterized by its degree of spin polarization p_r ranging from $p_r = 0$ for a normal metal to $p_r = 1$ for a half-metallic ferromagnet with majority-spin $\uparrow$ electrons only. A bias voltage V is applied symmetrically between the two ferromagnets. The bias voltage is so large that the Fermi function $f_r(\varepsilon) = \{1 + \exp[(\varepsilon - \mu_r)/k_\mathrm{B}T]\}^{-1}$ is one (zero) for the left (right) lead. Transport through the quantum dot is supported by unidirectional sequential tunneling with rates

$$\Gamma_{\sigma 0} = (1 \pm p_\mathrm{L})\Gamma_\mathrm{L}\,, \tag{4.11}$$

$$\Gamma_{0\sigma} = (1 \pm p_\mathrm{R})\Gamma_\mathrm{R}\,. \tag{4.12}$$

Again, the positive (negative) sign corresponds to $\sigma = \uparrow$ ($\downarrow$). We denote the asymmetry of tunnel couplings to source and drain by $a := (\Gamma_\mathrm{L} - \Gamma_\mathrm{R})/(\Gamma_\mathrm{L} + \Gamma_\mathrm{R})$.[4]

In Figure 4.7 (a), we demonstrate the possibility to detect the presence of correlations in this system. The dashed and dot-dashed line are derived as explained in Appendix A.2.2. Below the dashed line given by

$$a = \frac{3p_\mathrm{R}^2 + 4p_\mathrm{L}p_\mathrm{R} + 1}{3p_\mathrm{R}^2 - 3}\,, \tag{4.13}$$

all zeros $z_j(t)$ remain in the interval $(-\infty, -1]$, see Figure 4.8 (a), i.e., neither factorial nor generalized factorial cumulants indicate the presence of correlations. The same is true for the trivial case $p_\mathrm{R} = 0$ and the dot-dashed line given by

$$a = \frac{p_\mathrm{R}^2 + 2p_\mathrm{L}p_\mathrm{R} + 1}{p_\mathrm{R}^2 - 2p_\mathrm{L}p_\mathrm{R} - 3}\,, \tag{4.14}$$

where the system can be mapped onto a two-state model without the correlating Coulomb interaction, see Appendix A.2.1. Of course, t_min diverges at these system parameters, see Figure 4.7 (b). Above the dot-dashed line, all the zeros move into the complex plane, see Figure 4.8 (c), including the rightmost zeros which dominate the behavior of the factorial cumulants, $s = 1$. For large values of the spin polarization $p = p_\mathrm{L} = p_\mathrm{R}$ or the asymmetry a of the tunnel couplings, Eq. (3.43) is already violated for the second-order factorial cumulant ($m = 2$). Correlations are already detected by means of the commonly known Fano factor, see Eq. (3.35). With decreasing p or a, higher orders m of the factorial cumulants are needed to detect correlations.

An interesting regime resides between the dashed and dot-dashed line. Here, the rightmost zeros remain on the real axis with $z_j(t) \leq -1$, but zeros further to the left move into the complex plane, see Figure 4.8 (b). As a consequence, a violation of Eq. (3.43) cannot be found for any ordinary ($s = 1$) factorial cumulant. This limitation is overcome by generalized factorial cumulants. By an appropriate choice of s, they can probe the position of *any* zero $z_j(t)$ of $\mathcal{M}_\mathrm{F}(z,t)$ in the complex plane and, thus, detect correlations where ordinary factorial cumulants fail. Furthermore, as in Section 4.2, for a given order m, generalized factorial cumulants can detect correlations in a larger area of parameter space.

[4] Each tunnel coupling strength can be expressed via the asymmetry by $\Gamma_r = (1 \pm a)(\Gamma_\mathrm{L} + \Gamma_\mathrm{R})/2$ with positive (negative) sign for $r = \mathrm{L}\,(\mathrm{R})$, where $(\Gamma_\mathrm{L} + \Gamma_\mathrm{R})$ drops out if its inverse is chosen as unit of time.

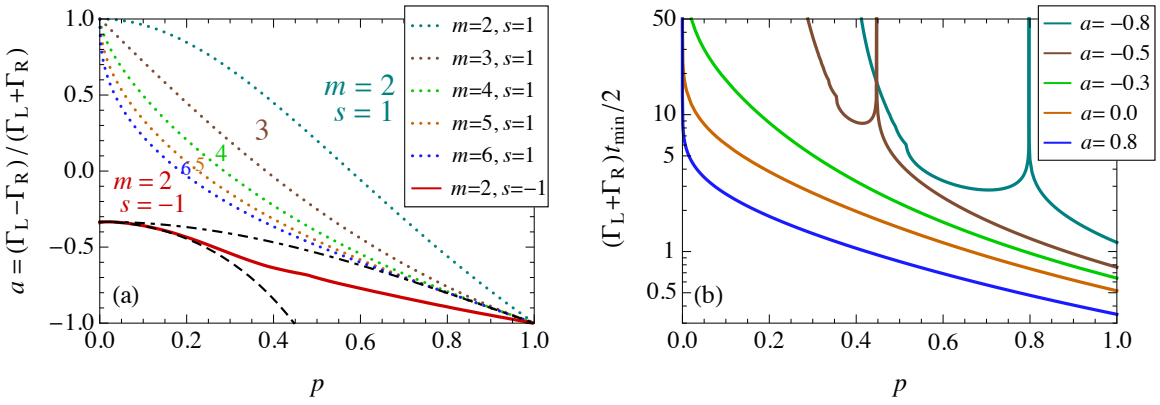

Figure 4.7: (a) Parameter space and (b) minimal time span $t_{\min}$ of a single-level quantum dot with ferromagnetic leads. The polarizations are $p_{\mathrm{L}} = p_{\mathrm{R}} = p$, however, a different polarization p_{L} (even $p_{\mathrm{L}} = 0$) does not change the results qualitatively. (a) Below the dashed line, $\mathcal{M}_s(z,t)$ has only zeros $\in (-\infty, -1]$ such that the sign criterion cannot be violated. The same is true exactly on the dot-dashed line. For different parameters above the colored lines, the sign criterion for the respective $C_{s,m}(t)$ is violated at some time t. (b) For $a \geq -1/3$, the minimal time $t_{\min}$ increases with decreasing p and decreasing a and diverges at $p = 0$; for $a < -1/3$, the minimal time $t_{\min}$ diverges both at the dashed and the dot-dashed line in (a).

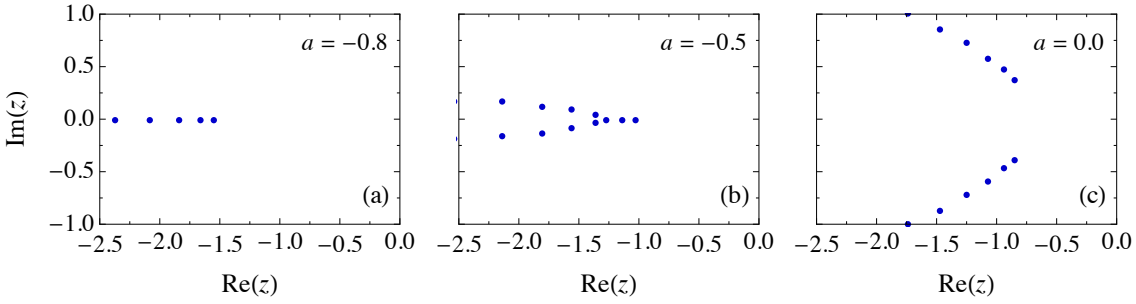

Figure 4.8: Zeros z_j for a single-level quantum dot with ferromagnetic leads discussed in Figure 4.7 with $p_{\mathrm{L}} = p_{\mathrm{R}} = 0.35$, $t = 50/(\Gamma_{\mathrm{L}} + \Gamma_{\mathrm{R}})$, and $a = (\Gamma_{\mathrm{L}} - \Gamma_{\mathrm{R}})/(\Gamma_{\mathrm{L}} + \Gamma_{\mathrm{R}}) = -0.8, -0.5, 0.0$. For $a = -0.8$, all zeros remain on and for $a = 0.0$ all zeros leave the real axis. For $a = -0.5$, the rightmost zeros remain on the real axis, but zeros further to the left move into the complex plane. While factorial cumulants are insensitive to correlations in this case, generalized factorial cumulants can detect their presence.

4.4 Conclusions

In summary, we demonstrated that generalized factorial cumulants $C_{s,m}(t)$ of the full counting statistics of electron transport through nanostructures are a sensitive and versatile tool to detect the presence of correlations via the violation of Eq. (3.43). Our discussion was based on two examples of a single-level quantum dot tunnel coupled to electronic reservoirs. Importantly, we demonstrated that already in a simple non-voltage biased case

of experimental relevance, correlations can be detected via generalized factorial cumulants.

We found that generalized factorial cumulants are superior to ordinary factorial ones: with decreasing s, correlation effects already show up in lower order m and at earlier times. This may be crucial for overcoming experimental limitations since the error of experimentally determined cumulants typically increases both with order and time [19, 20].

Furthermore, there are regimes in which generalized factorial cumulants can detect correlations while ordinary ones completely fail even for arbitrary large m.

Finally, we emphasize the general validity of the criterion Eq. (3.43). In future research, it may be used to study different transport regimes or types of correlations (e.g., not induced by Coulomb interaction). Moreover, multilevel and multichannel set-ups can be probed. The criterion may also be applied to systems where coherent superpositions of different quantum-dot states have to be taken into account.

5 Short-time counting statistics for Coulomb-blockade systems

In this chapter, we discuss the detection of correlations for Coulomb-blockade systems in the limit of time intervals $[0, t]$ being short in comparison to the average waiting time between two successive tunneling events.

In Section 5.1, we illustrate that ordinary cumulants are insufficient quantities for this purpose, in contrast to generalized factorial cumulants. In addition to criterion (3.43), we find for Coulomb-blockade systems in the short-time limit a more general criterion that will be given in Eq. (5.4).

To find the necessary ingredients for a violation of this criterion, we derive in Section 5.2 universal expressions for the generalized factorial cumulants to the leading order in t. At least three charge-states or fundamental tunneling processes of higher order are necessary to observe correlations. Our findings for the uncorrelated case of two-charge states are in complete agreement with novel experimental data [19].

As an example for correlated electron transport in the short-time limit, we simulate in Section 5.3 the generalized factorial cumulants for a normal-state island coupled to a superconducting lead. The simulated system has been recently experimentally realized in Ref. [5]. Correlations are identified and the validity of universal expressions of Section 5.2 is confirmed.

The results of this chapter have been published, in parts verbatim, in Ref. [94].

5.1 Detection of correlations in the short-time limit

In this chapter, we concentrate on the short-time limit of counting statistics in Coulomb-blockade systems, which can be simulated by a master equation, see Section 3.6. The short-time limit is defined by the length t of the measuring-time interval being small as compared to the average waiting time between two successive tunneling events. Of course, t has to remain larger than the time resolution of the detector. To emphasize once more, we do not cover non-Markovian effects [13, 15, 65]. We assume a detector counts the number of electrons tunneling out of a central region, e.g, an island or quantum dot. Counting starts after the system has reached its stationary state. Charging energy limits the number of possible charge states, i.e, only certain numbers of electrons on the central region are allowed. However, we take into account arbitrary many microscopic realizations of each charge state (e.g, the electrons on the central region may occupy different orbital and/or spin states). Coherent superpositions, as explained in more detail in Chapter 7, between different microscopic realizations but not between different charge states are also covered by our discussion.

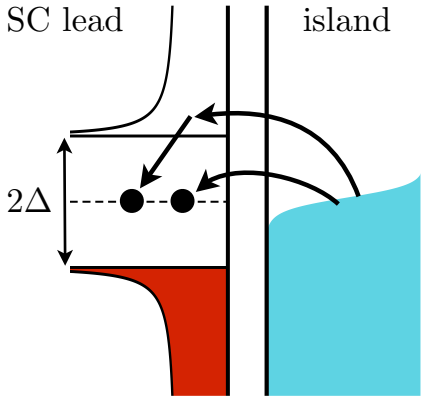

Figure 5.1: Andreev tunneling from a metallic island to a superconducting lead modeled as second-order tunneling process [95]. A single electron is annihilated in the island and a single excitation is created in the superconductor. Subsequently, a second electron is annihilated in the island and forms, together with the excitation, a Cooper pair.

As in the previous chapters, we aim at the detection of correlations between counted electrons. Correlations can arise between sequentially tunneling electrons, e.g., as a consequence of Coulomb interaction, cf. Chapter 4. Another source of correlations provides the superconducting pairing interaction [7–12, 96, 97]. If a metallic island is tunnel coupled to a superconducting lead, two electrons can be transferred simultaneously, see Figure 5.1. Such process is referred to as Andreev tunneling [98]. In a counting experiment, a single Andreev-tunneling process yields the probability distribution $P_2(t) = 1 - P_0(t)$ and $P_N(t) = 0$ for $N \neq 0, 2$. Thus, it cannot be decomposed into two single-electron subprocesses which would imply a finite probability $P_1(t)$. We see that any fundamental electron-tunneling process transferring $N > 1$ electrons is a correlated transfer process as defined in Chapter 3.4.

Ordinary cumulants in the short-time limit are *not* a convenient tool to identify correlations, neither for correlated sequential-tunneling processes nor for fundamental tunneling processes of multiple electrons. This can be understood by inspecting the moment-generating function

$$\mathcal{M}(z,t) = 1 + \mathbf{e}^T \mathbf{W}_{\exp(z)} \mathbf{p}_{\text{stat}}\, t + \mathcal{O}\left(t^2\right) . \tag{5.1}$$

What is the form of the leading order linear in t? Let us assume that a single electron can tunnel with a rate Γ_1, two electrons (Andreev tunneling) with Γ_2, and, in general, there may be fundamental processes in which even a larger number N of electrons tunnel simultaneously with Γ_N.[1] Thus, the probability distribution takes the form $P_N(t) = \Gamma_N t + \mathcal{O}(t^2)$ and $P_0(t) = 1 - \sum_{N\geq 1} \Gamma_N t + \mathcal{O}(t^2)$. It contains only contributions with at most *one* fundamental N-particle process during the measuring-time interval; contributions with more such processes are of order t^2 or higher. From Eq. (3.4), we obtain

$$\mathcal{M}(z,t) = 1 + \sum_{N\geq 1} \left(e^{Nz} - 1\right) \Gamma_N t + \mathcal{O}\left(t^2\right) \tag{5.2}$$

[1] In general, there may be several N-particle processes whose individual tunneling rates $\Gamma_{N\chi}$ depend on the state χ of the central region. In this case, Γ_N is the average rate, where each $\Gamma_{N\chi}$ is weighted with the probability to find the central region in state χ.

and the resulting cumulants in the short-time limit are

$$C_m(t) = \sum_{N\geq 1} N^m \Gamma_N t\,. \tag{5.3}$$

They are all positive and linear in t, irrespective of the presence or absence of correlations. Only the relative magnitude of the cumulants of different order m may be used to identify the presence of fundamental tunneling processes with $N \geq 2$.

Generalized factorial cumulants $C_{s,m}(t)$ in the short-time limit are much more convenient to identify correlations. Taking into account that in the short-time limit of a Coulomb-blockade system $C_1(t) = C_{\mathrm{F},1}(t) \propto t$, we see from Eq. (3.37) that the Poisson binomial distribution is determined by small probabilities $p_j(t) \propto t$. Inserting the resulting zeros $z_j(t) = -1/p_j(t)$ into Eq. (3.42) yields s-independent generalized factorial cumulants with fixed sign and time dependence

$$C_{s,m}(t) = C_{1,m}(t) \propto (-1)^{m-1} t^m\,. \tag{5.4}$$

In agreement with Eq. (3.43), which is valid for arbitrary time t, a different sign indicates correlations. But, in contrast to Eq. (3.43), this statement does also hold for odd m if $s < 0$. More remarkably, in the short time limit, also an s-dependence itself or a time dependence different from $\propto t^m$ proves the presence of correlations. In the following, we illustrate this for Coulomb-blockade systems with different numbers of accessible charge states and different fundamental tunneling processes.

5.2 Generalized factorial cumulants in the short-time limit

To obtain the $C_{s,m}(t)$ in the short-time limit, we first calculate the zeros $z_j(t)$ and then apply Eq. (3.42). What are the relevant zeros? For small but finite t, the $P_N(t)$ in Eq. (3.38) with $N \geq 1$ are small, which implies that the zeros $z_j(t)$ of the generating function have a large magnitude. From Eq. (3.42), it is clear that the short-time behavior of the (generalized) factorial cumulants is governed by those zeros $z_j(t)$ that diverge slowest as $t \to 0$. To determine them, we expand the generating function, Eq. (3.38), in powers of t and keep only the leading terms proportional to t^0. Hence, the constant term $z^0 t^0$ must be taken into account plus those terms $\propto z^k t^l$ with the smallest appearing ratio l/k (for $l \geq 1$). This yields $z_j(t) \propto t^{-l/k}$. Other terms can be neglected due to their larger ratio l/k.

5.2.1 Sequential tunneling for two charge states

We start by discussing sequential tunneling between two accessible charge states. In the short-time limit, we can approximate the generating function by $\mathcal{M}_{\mathrm{F}}(t) \approx 1 + zP_1(t)$, where $P_1(t) = \Gamma_1 t$ linear in time describes a single tunneling-out event. Contributions $P_N(t)$ with $N \geq 2$ tunneling-out events can be ignored for the following reason. After each tunneling-out event (being counted) an electron has to tunnel in (which is not counted) before another tunneling-out event can happen. This implies $P_N(t) \propto t^{2N-1}$ (with $N \geq 1$), and from all the contributions $z^N P_N(t) \propto z^N t^{2N-1}$ to the generating function, only the

one with $N = 1$ has to be kept since this has the smallest ratio $2 - 1/N$ of the exponents for t and z. Thus, there is only one zero

$$z_1(t) = -\frac{1}{\Gamma_1 t} \tag{5.5}$$

and by means of Eq. (3.42) we get the short-time generalized factorial cumulants

$$C_{s,m}(t) = (-1)^{m-1}(m-1)!\,(\Gamma_1 t)^m \propto t^m\,. \tag{5.6}$$

Despite the presence of Coulomb interactions (only two charge states are allowed) the cumulants agree with Eq. (5.4). They are s-independent, the sign is $(-1)^{m-1}$, and the power law t^m is recovered in the short-time limit. Thus, for a system restricted to two charge states, the short-time limit is not suited to detect correlations.

The short-time behavior of recently measured factorial cumulants for hole transfer in semiconductor quantum dots with dense excitation spectrum [19] is in full agreement with Eq. (5.6): while the alternation of the sign with increasing m is explicitly commented on, also the power-law dependence t^m is clearly visible in the data shown in Fig. 5(e) of Ref. [19]. Our argumentation now provides an explanation for this experimental finding.

5.2.2 Sequential tunneling for three charge states

If three charge states are accessible, two sequential-tunneling processes transferring an electron from the central region into the leads can occur in a row, i.e., $P_2(t) \propto t^2$ and $z^2 P_2(t) \propto z^2 t^2$ is equally important for the position of the zeros of the generating function as $zP_1(t) \propto zt$. But still, terms with $P_{N\geq 3}(t) \propto t^{2N-2}$ are negligible since they involve at least $N-2$ tunneling-in events that are not counted. As a result, we get $\mathcal{M}_{\mathrm{F}}(t) \approx 1 + zP_1(t) + z^2 P_2(t)$ with two zeros

$$z_{1,2}(t) = -\frac{2}{P_1(t) \pm \sqrt{P_1^2(t) - 4P_2(t)}}\,, \tag{5.7}$$

which yields

$$C_{s,m}(t) = (-1)^{m-1}(m-1)!\,[P_1(t)]^m\, a_m \propto t^m\,, \tag{5.8}$$

where the coefficient a_m is independent of time

$$a_m = \sum_{j=\pm 1} \left(\frac{1}{2} + \frac{j}{2} \sqrt{1 - \frac{4P_2(t)}{P_1^2(t)}} \right)^m\,. \tag{5.9}$$

Again, in the short-time limit, $C_{s,m}(t)$ is s-independent and obeys the power law t^m. But now, the sign can be modified: for $4P_2(t) > P_1^2(t)$ there are some m for which $a_m < 0$ such that $C_{s,m}(t)$ has the opposite sign as for a Poisson binomial distribution of uncorrelated tunneling events. We conclude that for a detection of correlations in the full counting statistics of sequential tunneling more than two charge states are necessary.

It is straightforward to extend this procedure to include more charge states. For each extra charge state, one more term $z^N P_N(t) \propto z^N t^N$ needs to be kept in the generating function, Eq. (3.38), giving rise to one more zero $z_j(t) \propto 1/t$ such that $C_{s,m}(t)$ is independent of s and proportional to t^m, but with a sign that may or may not be given by $(-1)^{m-1}$.

5.2.3 Sequential and two-electron tunneling for three charge states

In this Section, we include the presence of two-electron processes such as Andreev tunneling, where two electrons are tunneling out of an island simultaneously. This will lead to a power-law behavior of the short-time generalized factorial cumulants different from t^m. Moreover, an s-dependence will emerge.

While $P_1(t) = \Gamma_1 t$ is given by sequential tunneling with rate Γ_1, $P_2(t) = \Gamma_2 t$ is dominated by two-electron tunneling with rate Γ_2. Sequential tunneling of two electrons is negligible since it is of order t^2. Keeping only those terms $\propto z^k t^l$ with the smallest ratio l/k, we approximate the generating function for the case of three charge states by $\mathcal{M}_{\mathrm{F}}(t) \approx 1 + z^2\Gamma_2 t$. Plugging the zeros

$$z_{1,2}(t) = \pm\frac{i}{\sqrt{\Gamma_2 t}} \tag{5.10}$$

into Eq. (3.42) yields, for even m, the short-time generalized factorial cumulants

$$C_{s,m}^{\mathrm{even}}(t) = -(m-1)!\,2\,(-\Gamma_2 t)^{\frac{m}{2}} \propto t^{\frac{m}{2}}\,, \tag{5.11}$$

independent of s and independent of $P_1(t)$. For odd m, however, the two zeros determined above cancel out each other when plugged into Eq. (3.42), indicating that for odd m the approximation of the generating function was too crude. We need to include the next-order correction. To identify which terms to include, we use that the zeros diverge with $z_j(t) \propto 1/\sqrt{t}$. Thus, the correction (of order $\sqrt{t}$) is introduced by terms $\propto zt$. Therefore, we get $\mathcal{M}_{\mathrm{F}}(t) \approx 1 + z\Gamma_1 t + (z^2 + 2z)\Gamma_2 t$, while all other terms can still be neglected. The corresponding zeros are

$$z_{1,2}(t) = \pm\frac{i}{\sqrt{\Gamma_2 t}} - \frac{\Gamma_1}{2\Gamma_2} - 1\,, \tag{5.12}$$

which yields $1/[z_{1,2}(t) - s + 1] = \mp i\sqrt{\Gamma_2 t} - (\Gamma_1/2 + s\Gamma_2)t$. Finally, we obtain

$$C_{s,m}^{\mathrm{odd}}(t) = m!\,(-\Gamma_2 t)^{\frac{m-1}{2}}\,(\Gamma_1 + 2s\Gamma_2)\,t \propto t^{\frac{m+1}{2}}\,. \tag{5.13}$$

We note that, in contrast to even m, the odd-m generalized factorial cumulants depend both on s and on the sequential-tunneling rate Γ_1.

Combining the results for even and odd m, we conclude that the time-dependence $C_{s,m}(t) \propto t^{\lceil m/2 \rceil}$, where $\lceil m/2 \rceil$ is the smallest integer larger or equal to $m/2$, is qualitatively different from a Poisson binomial distribution of uncorrelated tunneling and also from a Coulomb-blockade system in which only sequential tunneling occurs. Also the sign is different, for $s \gtrless -\Gamma_1/(2\Gamma_2)$ given by $(-1)^{\lceil \pm m/2 \rceil - 1}$. We remark that the relative strength of single- and two-electron tunneling, Γ_2/Γ_1, influences the time below which the short-time limit is applicable but, ultimately, two-electron tunneling will always dominate the generalized factorial cumulants.

5.2.4 Higher-order tunneling

The discussion can be easily extended to include fundamental tunneling processes in which up to $N_{\max}$ electrons tunnel simultaneously. We find that the tunneling processes with

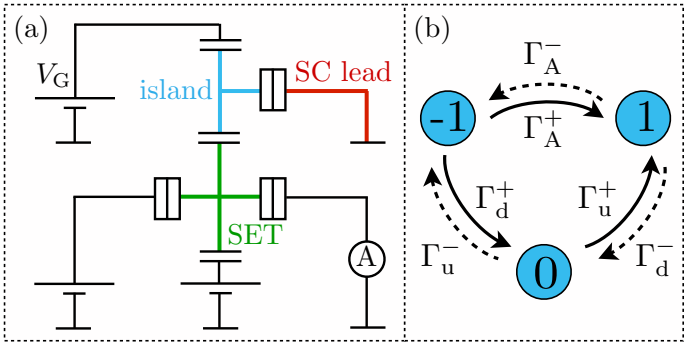

Figure 5.2: (a) Normal-state metallic island (blue) weakly tunnel coupled to a superconducting lead (red). Via the gate voltage V_G, the gate charge n_G of the island is tuned to zero. The current through a single-electron transistor (green) monitors the island charge n as a function of time. (b) Sketch of the states and transition rates.

$N_{\max}$, i.e., the largest number of simultaneously transferred electrons, dominate the short-time behavior of the generalized factorial cumulants. The time dependence is given by $C_{s,m}(t) \propto t^{\lceil m/N_{\max} \rceil}$. For $m = N_{\max}, 2N_{\max}, 3N_{\max}, \ldots$, the generalized factorial cumulants depend only on the leading order of the zeros $z_j(t) \propto t^{-1/N_{\max}}$ and they are independent of s. Otherwise next order corrections must be taken into account and generalized factorial cumulants become s-dependent. The zeros and, thus, the $p_j(t) = -1/z_j(t)$ are complex, and the electrons are transferred in a correlated manner.

5.3 Sequential and Andreev tunneling in a single-electron box

We illustrate our findings for a model system that has been experimentally realized in Refs. [5, 31, 32]. Its set-up is shown in Figure 5.2 (a).

A normal-metal island is tunnel coupled to a superconducting lead. This single-electron box (SEB) is characterized by the (normal-state) tunnel resistance R_T and the charging energy $E_C(n - n_G)^2$ for n electrons on the island. Via a gate voltage V_G, the gate charge n_G is tuned to the symmetry point $n_G = 0$. To monitor the charge n on the island, a single-electron transistor (SET) is electrostatically coupled: for each value of n there is a characteristic value of the current through the SET. At low temperature, only three charge states play a role, $n = -1, 0, 1$ (relative to some reference charge). Single-electron tunneling leads to transitions between $n = 0$ and ± 1, and Andreev tunneling imply direct changes between $n = +1$ and -1. The corresponding rates are $\Gamma_u^{\pm}$, $\Gamma_d^{\pm}$, and $\Gamma_A^{\pm}$, see Figure 5.2 (b).

In Ref. [5], the full counting statistics of Andreev tunneling (without distinguishing tunneling in from tunneling out and without counting sequential tunneling events) was measured. A strongly super-Poissonian distribution was found and attributed to avalanches of Andreev processes that form due to the interplay of Andreev and single-electron tunneling. By interpreting the data in terms of the cumulant generating function in the long-time limit, avalanches of up to 20 Andreev processes have been identified.

In the following, we consider the very same system but study the *short-time* charge-transfer statistics for *tunneling out* of the island via *both sequential and Andreev tunneling* and

characterize it via *generalized factorial cumulants*. Instead of calculating the tunneling rates $\Gamma_{\mathrm{u}}^{\pm}$, $\Gamma_{\mathrm{d}}^{\pm}$, and $\Gamma_{\mathrm{A}}^{\pm}$ in the presence of an electromagnetic environment [31, 99], we take the values $\Gamma_{\mathrm{u}}^{\pm} = \Gamma_{\mathrm{u}} = 12\,\mathrm{Hz}$, $\Gamma_{\mathrm{d}}^{\pm} = \Gamma_{\mathrm{d}} = 252\,\mathrm{Hz}$, and $\Gamma_{\mathrm{A}}^{\pm} = \Gamma_{\mathrm{A}} = 615\,\mathrm{Hz}$ that were experimentally measured in Ref. [5] at temperature 50 mK for $E_{\mathrm{C}} = 40\,\mu\mathrm{eV}$, $R_{\mathrm{T}} = 490\,\mathrm{k}\Omega$, and the superconducting gap $\Delta = 210\,\mu\mathrm{eV}$.

5.3.1 Numerical simulation

The charge-transfer dynamics can be simulated by the N-resolved master equation

$$\begin{aligned}
\dot{p}_N^{-1}(t) &= -\left(\Gamma_{\mathrm{A}} + \Gamma_{\mathrm{d}}\right) p_N^{-1}(t) + \Gamma_{\mathrm{u}} p_{N-1}^{0}(t) + \Gamma_{\mathrm{A}} p_{N-2}^{1}(t)\,, \\
\dot{p}_N^{0}(t) &= \Gamma_{\mathrm{d}} p_N^{-1}(t) - 2\Gamma_{\mathrm{u}} p_N^{0}(t) + \Gamma_{\mathrm{d}} p_{N-1}^{1}(t)\,, \\
\dot{p}_N^{1}(t) &= \Gamma_{\mathrm{A}} p_N^{-1}(t) + \Gamma_{\mathrm{u}} p_N^{0}(t) - \left(\Gamma_{\mathrm{A}} + \Gamma_{\mathrm{d}}\right) p_N^{1}(t),
\end{aligned} \tag{5.14}$$

for the probability $p_N^n(t)$ that at time t the island is in charge state n and N electrons have left the island in time interval $[0, t]$. Following Section 3.6, the generalized factorial cumulates are obtained from the generator

$$\mathbf{W}_z = \begin{pmatrix} -\Gamma_{\mathrm{A}} - \Gamma_{\mathrm{d}} & z\Gamma_{\mathrm{u}} & z^2\Gamma_{\mathrm{A}} \\ \Gamma_{\mathrm{d}} & -2\Gamma_{\mathrm{u}} & z\Gamma_{\mathrm{d}} \\ \Gamma_{\mathrm{A}} & \Gamma_{\mathrm{u}} & -\Gamma_{\mathrm{A}} - \Gamma_{\mathrm{d}} \end{pmatrix}. \tag{5.15}$$

Each counting factor z in the upper-right off-diagonal matrix elements correspond to counting an electron leaving the island. Since an Andreev-tunneling process transfers two electrons, Γ_{A} is multiplied with the square z^2 instead of a single z. The probability distribution $P_N(t)$ up to a certain order in t can be obtained by expanding Eq. (3.53) at $s = 0$ in powers of t

$$\mathcal{M}_0(z, t) = \sum_{j=0}^{\infty} \mathbf{e}^T \frac{(\mathbf{W}_z\, t)^j}{j!}\, \mathbf{p}_{\mathrm{stat}} \tag{5.16}$$

and taking advantage of Eq. (3.54) afterwards.

5.3.2 Factorial cumulants without Andreev tunneling

In order to identify the influence of Andreev tunneling on the full counting statistics, we, first, simulate the factorial cumulants ($s = 1$) in the absence of Andreev tunneling (we set $\Gamma_{\mathrm{A}} = 0$ but keep Γ_{u} and Γ_{d} unchanged).

The sign criterion (3.43) holds for every time t and order m, see Figure 5.3 (a). Moreover, in the short-time limit (given by $\Gamma_{\mathrm{d}} t \ll 1$), the time dependence matches Eq. (5.4). Indeed, the electrons are transported uncorrelated. In the long-time limit, all factorial cumulants are linear in time because $C_{1,m}(t) \to \partial_z^m [\lambda(z)]_{z=1} t$, where λ is the eigenvalue of $\mathbf{W}_z$ with the largest real part at $z = 1$. The long-time limit will be addressed in more detail in Section 6.2.

In the short-time limit, the numerical results even confirm the predicted dependence of the factorial cumulants on

$$P_1(t) = \frac{2\Gamma_{\mathrm{u}}\Gamma_{\mathrm{d}} t}{2\Gamma_{\mathrm{u}} + \Gamma_{\mathrm{d}}}\,, \quad P_2(t) = \frac{\Gamma_{\mathrm{u}}^2 \Gamma_{\mathrm{d}} t^2}{2(2\Gamma_{\mathrm{u}} + \Gamma_{\mathrm{d}})}\,, \tag{5.17}$$

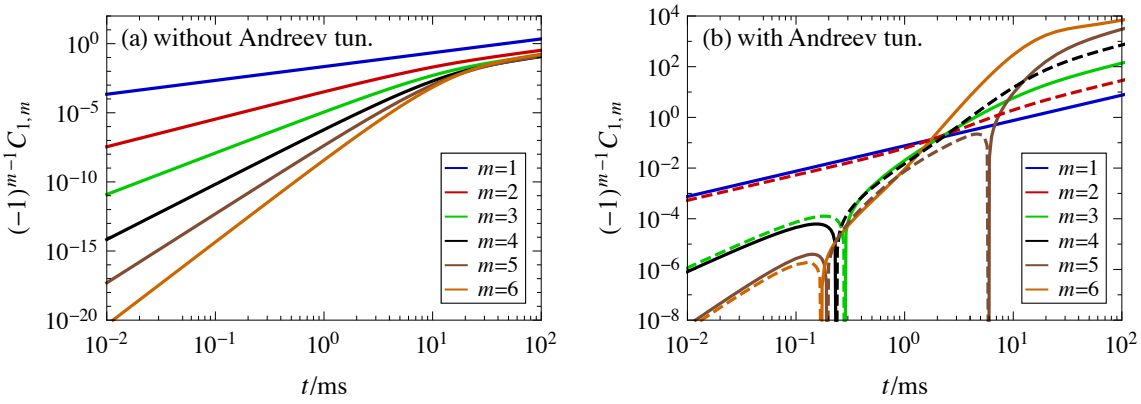

Figure 5.3: Factorial cumulants as a function of time (a) without and (b) with Andreev tunneling. The sign of $(-1)^{m-1}C_{1,m}$ is positive for continuous and negative for dashed lines.

see Eq. (5.8), which has been derived by a general argumentation in Section 5.2. We remark that the short-time (but not the long-time) factorial cumulants in the absence of Andreev tunneling are identical to those when Andreev tunneling processes are present but not counted. This could be immediately realized for the set-up of Ref. [5]. Furthermore, we mention that if we chose for the considered model $\Gamma_\mathrm{u} > \Gamma_\mathrm{d}/2$ then $4P_2(t) > P_1^2(t)$, and $(-1)^{m-1}C_{1,m}(t)$ would become negative for some m and t, in accordance to the discussion in Section 5.2.2.

5.3.3 Factorial cumulants with Andreev tunneling

In the presence of Andreev tunneling, the factorial cumulants are qualitatively different, see Figure 5.3 (b). The only common feature is the linear long-time behavior. We now find extended regions violating the sign criterion (3.43), indicated by dashed lines in Figure 5.3 (b). Moreover, in the short-time limit, the time dependence violates Eq. (5.4). Thus, both the sign and the time dependence prove the presence of correlations.

Again, we can confirm the validity of the general argumentation in Section 5.2. In the short-time limit, the numerical results coincide with Eqs. (5.11) and (5.13) with

$$\Gamma_1 = \frac{2\Gamma_\mathrm{u}\Gamma_\mathrm{d}}{2\Gamma_\mathrm{u}+\Gamma_\mathrm{d}}\,, \quad \Gamma_2 = \frac{\Gamma_\mathrm{u}\Gamma_\mathrm{A}}{2\Gamma_\mathrm{u}+\Gamma_\mathrm{d}}\,, \tag{5.18}$$

and the factorial cumulants follow the power law $C_{1,m}(t) \propto t^{\lceil m/2 \rceil}$.

5.3.4 Generalized factorial cumulants

Finally, we investigate the s-dependence of the generalized factorial cumulants in the short-time limit.

In the absence of Andreev tunneling, the numerical simulation yields s-independent generalized factorial cumulants. In Figure 5.4 (a), the chosen t is so small that only a weak

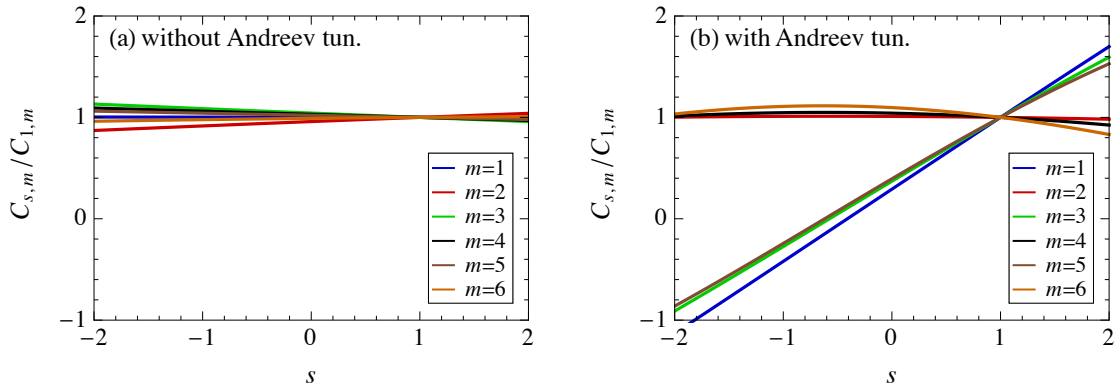

Figure 5.4: Generalized factorial cumulants $C_{s,m}$ normalized by $C_{1,m}$ as a function of s (a) without and (b) with Andreev tunneling at time (a) $t = 0.7\,\mathrm{ms}$ and (b) $t = 0.1\,\mathrm{ms}$. Both in (a) and (b), time is slightly above short-time limit such that all 6 cumulants can still be distinguished. In the short-time limit, all cumulants in (a) coincide and are s-independent. In contrast, factorial cumulants of odd order m display an s-dependence in (b).

s-dependence can still be observed, i.e., the short-time limit is nearly reached. Criterion (5.4) is fulfilled since electron transport is uncorrelated. The missing s-dependence is also in agreement with Eq. (5.8).

In the presence of Andreev tunneling, the generalized factorial cumulants of odd order m become s-dependent as shown in Figure 5.4 (b). Criterion (5.4) is violated and the presence of correlations is proven. The linear s-dependence for odd orders m and also the s-independence for even orders m is in agreement with the universal Eqs. (5.11) and (5.13).

We want to emphasize that already the generalized factorial cumulant of first order $C_{s,1}(t)$ indicates the correlations, whereas the first ordinary factorial cumulant $C_{1,1}(t)$ fails both for short and finite times. Moreover, the s-dependence can be used, in general, to obtain information about the next-to-leading order of the time dependence of the zeros $z_j(t)$ of the generating function, see Section 5.2.

5.4 Conclusions

In summary, we demonstrated that generalized factorial cumulants $C_{s,m}(t)$ of the full counting statistics of electron transport through Coulomb-blockade systems are even in the limit of short time intervals t a sensitive tool to detect correlations via the violation of Eq. (5.4). In addition to the criterion Eq. (5.4), also a different sign for odd m and $s < 0$, any s-dependence itself, or a time dependence different from $C_{s,m}(t) \propto t^m$ proves the presence of correlations.

We presented a general argumentation for what kind of Coulomb-blockade systems the criterion can be violated and in what sense. Our argumentation was just based on the number of accessible charge states and the appearance of different fundamental tunneling processes. Nevertheless, we obtained universal expressions for the generalized factorial cumulants $C_{s,m}(t)$ in the short-time limit.

We illustrated our theoretical findings for the example system of a normal-state island coupled to a superconducting lead [5]. The presence of Andreev tunneling leads to correlated electron transport which can already be identified by the s-dependence of the generalized factorial cumulant of first order $C_{s,1}(t)$. Higher-order (generalized) factorial cumulants show a characteristic power law $t^{\frac{m}{2}}$ for even and $t^{\frac{m+1}{2}}$ for odd orders m.

Finally, we emphasize that the experimental feasibility benefits from shorter times t since cutting the total measured time trace into shorter and, therefore, more time intervals reduces statistical errors.[2]

[2] In Ref. [19], factorial cumulants up to 12^{th} order have been measured down to intervals t so short that (in average) only 1 of 100 intervals includes a tunneling event.

6 Inverse counting statistics based on generalized factorial cumulants

In this chapter, we concentrate on the generalized factorial cumulants in the limit of long measuring-time intervals $[0, t]$. We propose a method to reconstruct, solely from these cumulants as input parameters, characteristic features of an otherwise unknown stochastic system, e.g., a lower bound for the system dimension and the full spectrum of relaxation rates [67–72].

Our method, denoted in the following by *inverse counting statistics*, can be applied to Coulomb-blockade systems as outlined in Section 3.6, but also to any other stochastic system governed by an N-resolved Markovian master equation (3.47). Thus, in addition to Section 3.6, we do not care about the physical nature of the states χ and allow the detector to count arbitrary many transitions of arbitrary sort increasing the detector counter by an arbitrary amount, see Figure 6.1. Inverse counting statistics covers, therefore, also fields as biological physics, where stochastic transitions like the steps of motor proteins [100, 101], intramolecular conformational changes [102–104], and enzymatic turnovers generating fluorescent products [105, 106] are studied. Detectors are optical tweezers [100, 107], atomic force, or fluorescence microscopes [107, 108].

A short introduction to inverse counting statistics is given in Section 6.1, where we elucidate the relation of our method to the previous work [109]. Details concerning the input and output parameters of inverse counting statistics are given in Section 6.2 and Section 6.3, respectively. We illustrate our procedure for two example systems. In Section 6.4, we consider a single-level quantum dot coupled to one normal-metal lead as introduced in Section 4.2. In Section 6.5, we study a normal-metal island coupled to a superconducting lead as introduced in Section 5.3. For the latter system, the generalized factorial cumulants reveal an additional dimension and relaxation rate which are both hidden to ordinary (factorial) cumulants. Finally, we give a short summary of the inverse-counting-statistics procedure in form of a step-by-step manual in Section 6.6.

The results of this chapter have been published, in parts verbatim, in Ref. [110].

6.1 Introduction

For a well-characterized system, the states, the rates between them, and the coupling to the detector are known. It is, then, straightforward to compute the full counting statistics (i.e., statistical moments, cumulants, or the probability distribution P_N) and compare the simulation with experimentally measured data. Suppose, however, that the underlying model for a stochastic system is unclear and the only information available is the counting statistics measured by the detector. It is, then, desirable to have a systematic approach to distill out of the measured counting statistics the relevant information for reconstructing

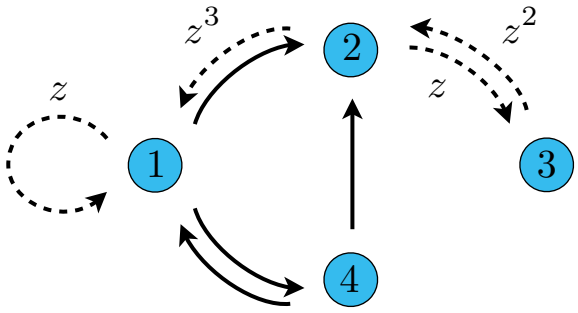

Figure 6.1: A stochastic system with $M = 4$ states. Transitions are indicated by arrows. Dashed arrows indicate transitions counted by the detector with counting factors z^k appearing in the corresponding generator $\mathbf{W}_z$.

properties of the underlying model, such as the number M of states of the stochastic system and the eigenvalues $\lambda_j(z)$ of the generator $\mathbf{W}_z$ of the time-evolution, cf. Section 3.6. Such an approach can be dubbed *inverse counting statistics* [109].

Of course, inverse counting statistics cannot distinguish between different stochastic systems that are equivalent in the sense that they produce the same counting statistics, even if the stochastic systems possess a different numbers of states. Therefore, inverse counting statistics can at most deliver the *minimal* number of system states necessary that is compatible with the observed counting statistics.

Given a measured distribution P_N, what are the input data for the inverse counting statistics? In [109], it was suggested to use the ordinary cumulants C_m in the long-time limit. Here, we propose to use generalized factorial cumulants $C_{s,m}$ instead. The advantage of the latter is that they depend on an arbitrarily chosen parameter s. The outcome of the inverse counting statistics (such as the number of system states or the spectrum of relaxation rates) should, however, not depend on this parameter s. Therefore, the s-independence of the results defines a powerful consistency criterion. Furthermore, as we will see in Section 6.5, there are special cases in which part of the relaxation-rate spectrum is not accessible by inverse counting statistics with ordinary cumulants but is detectable by using generalized factorial cumulants with properly chosen parameter s.

As another difference to [109], we allow for a more general system-detector coupling by introducing the *counting power* D. In [109], the detector is assumed to be sensitive to only a single transition between two specific states increasing the detector counter just by one, the counting power is $D = 1$. If this transition increases the detector counter by k, the counting power is $D = k$. If several transitions are counted by the detector, the counting power can be even larger. We allow for detectors counting arbitrarily many transitions between arbitrarily many states increasing the detector counter by an arbitrary amount. Therefore, our inverse counting procedure does not only test compatibility with the number M of system states but also with the counting power D.

6.2 Input of inverse counting statistics

Taking Eqs. (3.40) and (3.53) into account, the generalized factorial cumulants $C_{s,m}(t)$ at arbitrary time t can be written in the form

$$C_{s,m}(t) = \frac{\partial^m}{\partial z^m} \ln \left[\sum_{j=1}^{M} \left(\mathbf{e}^T \mathbf{r}_{z,j} \right) \left(\mathbf{l}_{z,j}^T \, \mathbf{p}_{\mathrm{stat}} \right) e^{\lambda_j(z) t} \right]_{z=s} . \tag{6.1}$$

We emphasize that only steady-state counting statistics is considered, i.e., we assume that the system has already relaxed to $\mathbf{p}_{\mathrm{stat}}$ before counting starts, cf. Section 3.6. This excludes studying transient behavior after a perturbation of the system. Such an approach has been recently used to experimentally measure some relaxation rate $\lambda_j(1)$ [111–115]. However, to determine the full spectrum of relaxation rates $\{\lambda_j(1)\}$, the approach would require the knowledge of how to perturb the system in order to probe a specific relaxation rate.

The summation over j complicates the time dependence of the generalized factorial cumulants. In the long-time limit, however, Eq. (6.1) becomes considerably simpler since the exponential factors suppress all terms of the sum except the ones with the largest real part $\mathrm{Re}\,[\lambda_j(z)]$ for $z = s$. For $z = 1$ and systems with a unique stationary state, the dominant eigenvalue is 0. All other eigenvalues have a negative real part.[1] Around $z = 1$, the dominant eigenvalue, denoted by $\lambda_{\max}(z)$, remains real and the limit

$$c_{s,m} := \lim_{t \to \infty} \frac{C_{s,m}(t)}{t} = \left. \frac{\partial^m \lambda_{\max}(z)}{\partial z^m} \right|_{z=s} , \tag{6.2}$$

provides well-defined constants, referred to as scaled long-time (generalized factorial) cumulants.

These scaled long-time cumulants $c_{s,m}$ define the input information for the inverse counting statistics. Of course, in an experiment, the time t is always finite and, moreover, $\lambda_{\max}(z)$ is not directly accessible. Therefore, one has to use scaled finite-time cumulants $C_{s,m}(t)/t$, with $C_{s,m}(t)$ obtained via Eqs. (3.38) and (3.40) from the measured $P_N(t)$. For large t, the scaled cumulants become time independent such that $C_{s,m}(t)/t \approx c_{s,m}$.

If s is chosen very negative, it may happen that the dominant eigenvalues are given by a complex-conjugated pair. In this case, the limit is not well defined and the inverse counting-statistics procedure derived below cannot be applied.

6.3 Output of inverse counting statistics

In Section 3.6, we have shown how to calculate for a given stochastic model defined by the generator $\mathbf{W}_z$ the respective cumulants. Inverse counting statistics deals with the opposite problem: how much can we learn about the stochastic system if only a few numbers, namely the experimentally determined values of the scaled long-time cumulants $c_{s,m}$ (up to some order), are given?

We aim at the following properties of the stochastic system. First, a very important feature of the system is the dimension M of $\mathbf{W}_z$, i.e., the number of participating states in the

[1] Otherwise, Eq. (3.50) would not lead to the unique stationary state $\mathbf{p}_{\mathrm{stat}}$ for arbitrary initial $\mathbf{p}_1(0)$.

stochastic process. Furthermore, the coupling to the detector is described by powers of z attached to some matrix elements of the generator. As a consequence, the characteristic polynomial $\det(\lambda\mathbf{1} - \mathbf{W}_z)$ is of order D in z. Thus, as a second feature, we identify the counting power D. We show below that the values of the first $(D+1)M$ scaled long-time cumulants are enough to check compatibility with a stochastic system of dimension M and the counting power D characterizing the coupling to the detector.

But, with inverse counting statistics, we can get much more. From the $(D+1)M$ input parameters $c_{s,m}$ it is possible to determine the full spectrum of $\mathbf{W}_z$, i.e., the full z-dependence of the eigenvalues $\lambda_j(z)$. To appreciate how remarkable this statement is, let us remind that the input parameters are only a finite $[(D+1)M]$ number of derivatives of only one eigenvalue $\lambda_{\max}$ at only one value of z, namely the arbitrarily chosen s. From this rather restricted amount of information, we aim at reconstructing also the other eigenvalues different from $\lambda_{\max}$ at all values of z different from s. How is this possible and how does it work in practice?

To answer this question, we observe that the characteristic function of the generator $\mathbf{W}_z$,

$$\chi(z,\lambda) = \det(\lambda\mathbf{1} - \mathbf{W}_z) = \prod_{j=1}^{M} [\lambda - \lambda_j(z)] \,, \tag{6.3}$$

is a polynomial both in λ (of order M) and in z (of order D). The eigenvalues $\lambda_j(z)$, i.e., the zeros of the characteristic function, $\chi(z,\lambda_j(z)) = 0$, are, in general, nonanalytic functions in z. The characteristic function $\chi(z,\lambda)$ itself, however, is a polynomial in z and can, therefore, be written in the form

$$\chi(z,\lambda) = \lambda^M + \sum_{\mu=0}^{D} \sum_{\nu=0}^{M-1} a_{\mu\nu} (z-s)^\mu \lambda^\nu \,, \tag{6.4}$$

where s is the arbitrarily chosen parameter of the generalized factorial cumulants. As a consequence, the (s-independent) characteristic function is fully determined by the $(D+1)M$ real (and s-dependent) coefficients $a_{\mu\nu}$. This fixes all z-dependent (but s-independent) eigenvalues $\lambda_j(z)$ of the generator $\mathbf{W}_z$. For this reason, $(D+1)M$ input parameters are enough to fully determine the spectrum of $\mathbf{W}_z$.

Suppose that M and D are already known (we will discuss below how this is done with the help of inverse counting statistics). How do we get the spectrum of $\mathbf{W}_z$? As input parameters, we use the scaled generalized factorial cumulants $c_{s,m}$ for $m = 0, \ldots, (D+1)M-1$ in the long-time limit. To determine the coefficients $a_{\mu\nu}$, we perform $l = 0, \ldots, (D+1)M-1$ times a derivative of $\chi(z,\lambda(z)) \equiv 0$ with respect to z and set $z = s$ afterwards. For technical reasons, it is convenient to divide the resulting equation by $l!$. Then, we arrive at the set of linear equations

$$0 = A_{l,0M} + \sum_{\mu=0}^{D} \sum_{\nu=0}^{M-1} A_{l,\mu\nu} a_{\mu\nu} \,, \tag{6.5}$$

for $l = 0, \ldots, (D+1)M-1$. The coefficients $A_{l,\mu\nu}$, defined for nonnegative l, μ, and ν, are given by

$$A_{l,\mu\nu} = \begin{cases} 0 & \text{for} \quad l < \mu \\ 1 & \text{for} \quad l = \mu, \nu = 0 \\ 0 & \text{for} \quad l > \mu, \nu = 0 \end{cases} \tag{6.6}$$

and otherwise (i.e., $l \geq \mu$ together with $\nu \geq 1$) by

$$A_{l,\mu\nu} = \sum_{\alpha_1+\ldots+\alpha_\nu=l-\mu} \frac{c_{s,\alpha_1}}{\alpha_1!} \cdot \frac{c_{s,\alpha_2}}{\alpha_2!} \cdots \frac{c_{s,\alpha_\nu}}{\alpha_\nu!} \,. \tag{6.7}$$

Obviously, $A_{l,\mu\nu}$ depends on l and μ only via the difference $l-\mu$ (this was the reason of dividing by $l!$). The multiple sum over the α is constrained by $\alpha_1 + \ldots + \alpha_\nu = l - \mu$. An alternative expression for the $A_{l,\mu\nu}$ can be found in Appendix A.3.1.

To be explicit, let us write down all the terms that are relevant for the case $M = 3$ and $D = 2$. We need ν up to 2 and l up to 8. For $\nu = 0$ we get $A_{l,\mu 0} = \delta_{l\mu}$, for $\nu = 1$ we have $A_{l,\mu 1} = c_{s,l-\mu}/(l-\mu)!$, and for $\nu = 2$ we find

$$\begin{aligned}
A_{\mu,\mu 2} &= c_{s,0}^2 \,, \\
A_{\mu+1,\mu 2} &= 2c_{s,0}c_{s,1} \,, \\
A_{\mu+2,\mu 2} &= c_{s,0}c_{s,2} + c_{s,1}^2 \,, \\
A_{\mu+3,\mu 2} &= \frac{c_{s,0}c_{s,3}}{3} + c_{s,1}c_{s,2} \,, \\
A_{\mu+4,\mu 2} &= \frac{c_{s,0}c_{s,4}}{12} + \frac{c_{s,1}c_{s,3}}{3} + \frac{c_{s,2}c_{s,2}}{4} \,, \\
A_{\mu+5,\mu 2} &= \frac{c_{s,0}c_{s,5}}{60} + \frac{c_{s,1}c_{s,4}}{12} + \frac{c_{s,2}c_{s,3}}{6} \,, \\
A_{\mu+6,\mu 2} &= \frac{c_{s,0}c_{s,6}}{360} + \frac{c_{s,1}c_{s,5}}{60} + \frac{c_{s,2}c_{s,4}}{24} + \frac{c_{s,3}c_{s,3}}{36} \,, \\
A_{\mu+7,\mu 2} &= \frac{c_{s,0}c_{s,7}}{2520} + \frac{c_{s,1}c_{s,6}}{360} + \frac{c_{s,2}c_{s,5}}{120} + \frac{c_{s,3}c_{s,4}}{72} \,, \\
A_{\mu+8,\mu 2} &= \frac{c_{s,0}c_{s,8}}{20160} + \frac{c_{s,1}c_{s,7}}{2520} + \frac{c_{s,2}c_{s,6}}{720} + \frac{c_{s,3}c_{s,5}}{360} + \frac{c_{s,4}c_{s,4}}{576} \,.
\end{aligned}$$

To obtain the full spectrum $\{\lambda_j(z)\}$, one first solves the set of linear Eqs. (6.5) for $a_{\mu\nu}$. Second, the result for $a_{\mu\nu}$ is inserted into Eq. (6.4) to get the characteristic function. Finally, the zeros of the characteristic function are determined. It all works because the characteristic function is fully determined by a finite number of coefficients $a_{\mu\nu}$ only.

It is important to remark that, in general, there is no guarantee that the set of linear Eqs. (6.5) provides a unique solution. There may be special situations (we will discuss such a case below) in which the generator $\mathbf{W}_z$ is separable in the sense that its characteristic function can be written as a product of two polynomials, the first one of order D' and M' in z and λ, the second one of order $D - D'$ and $M - M'$. Of course, it is trivial that the characteristic function can always be written as a product of two polynomials in λ, but separability requires that, in addition, the two polynomials in λ are polynomials in z as well. For separable generators, inverse counting statistics has only access to the part of the spectrum to which the eigenvalue $\lambda_{\max}(z)$ with the largest real part belongs, i.e., the effective problem has reduced dimensions M' and D'.

The remaining question to be answered is how to determine the dimensions M and D of the stochastic system. In the spirit of [109], one may suggest that after having determined $\lambda_{\max}(z)$ from the first $(D+1)M$ scaled long-time cumulants $c_{s,m}$ one can calculate the $c_{s,m}$ of higher order and compare them with experimentally measured values $C_{s,m}(t)/t$ in the long-time limit. If M and D were chosen correctly, then one expects a coincidence of calculated and measured values. This has, however, two downsides. First, measuring

cumulants of increasingly higher order may become more and more difficult. Second, comparing just numbers to establish a consistency criterion may be of only limited significance in view of experimentally unavoidable noise.

With the use of generalized factorial cumulants, however, we can do much better. Remember that the parameter s was chosen arbitrarily and the result, i.e., the spectrum of the generator, must be independent of this parameter s. Therefore, we can use the very same measured time trace of the detector to determine scaled cumulants $C_{s,m}(t)/t$ in the long-time limit for different values of s and, afterwards, run the inverse counting-statistics procedure for each s. If M and D were chosen correctly, then the *full* z-dependence of the *full* spectrum should be independent of the choice of s. This establishes a much stronger consistency check than comparing just a few numbers.

In the following Sections 6.4 and 6.5, we illustrate the inverse counting-statistics procedure for two example systems: a single-level quantum dot in a Zeeman field and a normal-metal island coupled to a superconducting lead.

6.4 Single-level quantum dot with Zeeman field

The first example system is the single-level quantum dot subjected to a Zeeman field as introduced in Sections 4.1 and 4.2. The system is depicted in Figure 4.1 (a) and its generator $\mathbf{W}_z$ takes the form presented in Eq. (4.7) with the transition rates from Eqs. (4.8) and (4.9). The characteristic function is a polynomial of order $M = 3$ in λ and of order $D = 1$ in z.

6.4.1 Nonvanishing magnetic field

We begin by discussing the case of nonvanishing magnetic field for which we choose $\varepsilon = -k_\mathrm{B}T$ and $\Delta = k_\mathrm{B}T/2$. As unit of time we chose the inverse of $\Gamma = \Gamma_{\sigma 0} + \Gamma_{0\sigma}$. The input information for the inverse counting statistics (for $M = 3$ and $D = 1$) is given by the scaled long-time generalized factorial cumulants $c_{s,m}$ from order 0 up to order $(D+1)M - 1 = 5$. Since in experiments, the measurement time is always finite, we do not take as input parameters the exact scaled long-time cumulants of the defined model but calculate, instead, the scaled finite-time cumulants $C_{s,m}(t)/t$ at some large but finite time t. Hence, the scaled cumulants are close but not identical to the exact values in the long-time limit. For the exact long-time scaled cumulants, a value for the dimension M that was assumed to be too large, can be immediately identified by trying to solve the system of linear Eqs. (6.5). Then, no unique solution for every $a_{\mu\nu}$ is obtained, i.e., the linear equations are not independent from each other. However, in the following, we stick to the experimental situation that, due to the finite measuring time or due to experimental noise, a unique solution for the system of linear Eqs. (6.5) is even obtained if M is assumed too large.

First, we determine the eigenvalue spectrum from the inverse counting statistics performed at $s = 1$ and assuming the correct values $M = 3$ and $D = 1$. As input parameters, we take the calculated scaled generalized factorial cumulants $C_{s,m}(t)/t$ at times $\Gamma t = 10, 20, 100$. The result is shown in Figure 6.2 (a). For $\Gamma t = 100$, the long-time limit is reached and

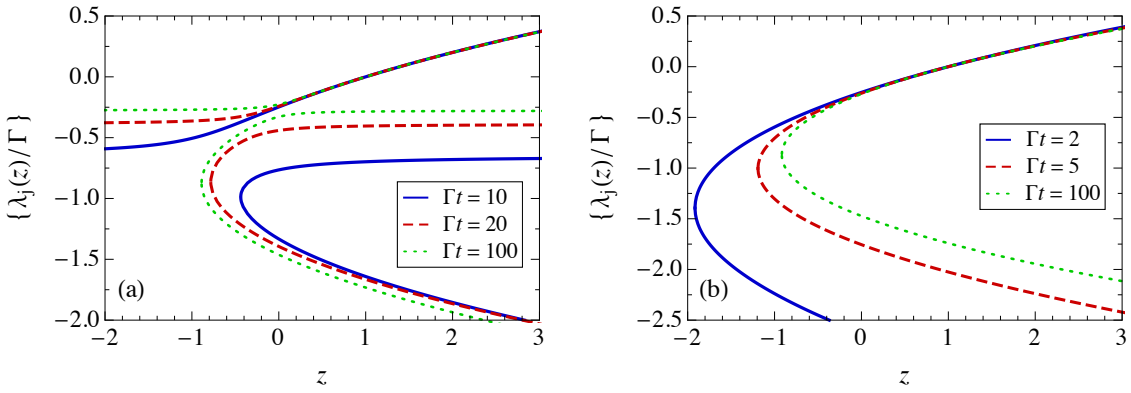

Figure 6.2: Eigenvalue spectrum obtained via inverse counting statistics for a single-level quantum dot $\varepsilon = -k_{\mathrm{B}}T$ (a) inside a magnetic field $\Delta = k_{\mathrm{B}}T/2$ and (b) without magnetic field. The input data are scaled cumulants $C_{s,m}(t)/t$ for finite times t. Only in the long-time limit $\Gamma t \gtrsim 100$, the output $\{\lambda_j\}$ is indeed the eigenvalue spectrum of the generator $\mathbf{W}_z$ given in Eq. (4.7). Values λ_j with a finite imaginary part (occurring for very negative z) are not depicted.

no difference to the exact eigenvalues can be noticed anymore. The green dotted lines are indeed the full eigenvalue spectrum of the generator $\mathbf{W}_z$.

Next, we demonstrate the consistency check for the dimensions M and D. For this, we check the required s-independence of the eigenvalue spectrum. In the following, we always use as input information the calculated scaled cumulants at $\Gamma t = 6000$ to ensure convergence to the asymptotic long-time behavior not only for $s = 1$ but also for other s.

To show simultaneously both the z- and the s-dependence of the eigenvalues, we plot in the following figures the contour lines for different selected values of λ (in units of Γ). Horizontal contour lines indicate that the eigenvalues are independent of s. If *all* eigenvalues are s-independent, then, the assumed dimensions M and D are compatible with the input data. In Figure 6.3 (a) and (b), we show the result for the choice $M = 2$ and $D = 1$. Since the dimension M of the stochastic systems is taken too small, the resulting eigenvalues display a strong s-dependence, especially the eigenvalue λ_1. However, if we take the proper values $M = 3$ and $D = 1$, see Figure 6.3 (c), (d), (e), we get s-independent results. The order $M = 3$ and $D = 1$ are lower bounds for the system's dimensions.

6.4.2 Vanishing magnetic field

The case of vanishing magnetic field $\Delta = 0$ is special because due to spin degeneracy $\varepsilon_\uparrow = \varepsilon_\downarrow$ only two different rates $\Gamma_{\uparrow 0} = \Gamma_{\downarrow 0} = \Gamma_{10}$ and $\Gamma_{0\uparrow} = \Gamma_{0\downarrow} = \Gamma_{01}$ appear. As a consequence, the characteristic function becomes separable,

$$\chi(z,\lambda) = \chi_{1,2}(z,\lambda)\cdot\chi_3(\lambda) \tag{6.8}$$

$$\chi_{1,2}(z,\lambda) = \lambda^2 + (\Gamma_{01}+2\Gamma_{10})\lambda - 2(1-z)\Gamma_{01}\Gamma_{10} \tag{6.9}$$

$$\chi_3(\lambda) = \lambda + \Gamma_{01}\,. \tag{6.10}$$

The first factor is a polynomial of order $M = 2$ in λ and of order $D = 1$ in z, while the second factor is of order $M = 1$ and independent of z. Due to the z-independency, the

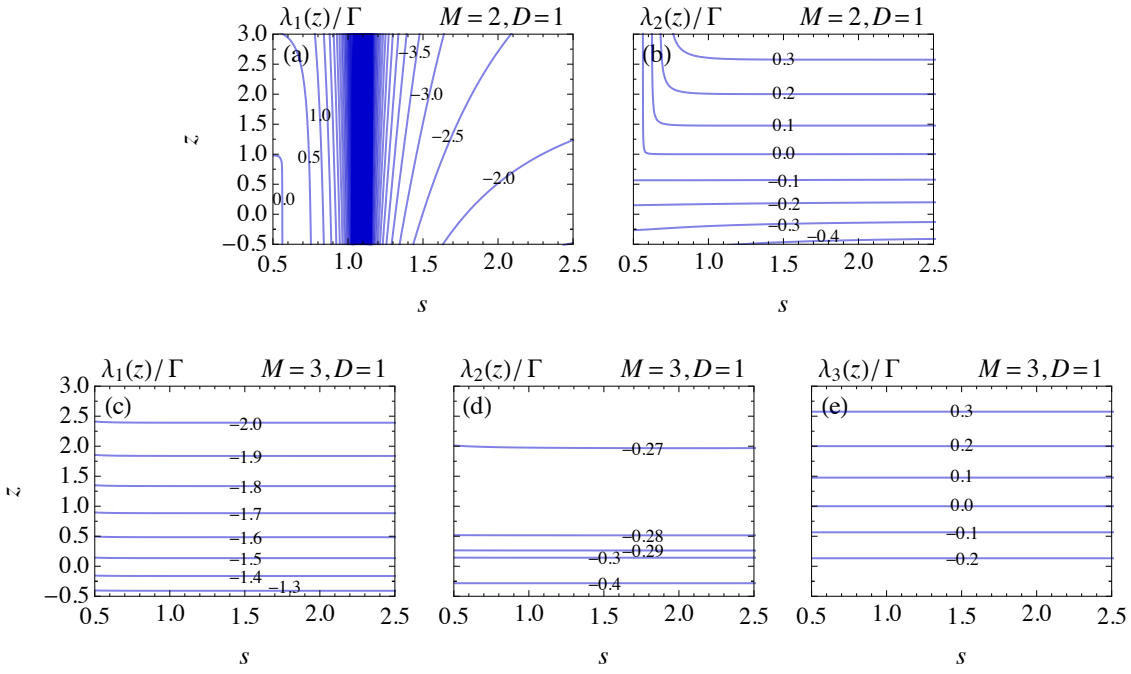

Figure 6.3: Consistency check of the number of system states M and the counting power D for the single-level quantum dot $\varepsilon = -k_{\mathrm{B}}T$ in a magnetic field $\Delta = k_{\mathrm{B}}T/2$ for time $\Gamma t = 6000$. Assuming different values for M and D, contour lines of the resulting $j = 1, \ldots, M$ eigenvalues $\lambda_j(z)/\Gamma$ are depicted. The eigenvalues for $M = 2$, $D = 1$ in (a), (b) show a strong s-dependence, the ones for $M = 3$, $D = 1$ in (c), (d), (e) are s-independent.

second factor does not influence counting statistics and thus cannot be detected anymore. The electron transfer can be completely described by a spinless orbital which is occupied with rate $\Gamma_{10} := \Gamma_{\uparrow 0} + \Gamma_{\downarrow 0}$ and emptied with rate $\Gamma_{01} := \Gamma_{0\uparrow} = \Gamma_{0\downarrow}$, cf. Appendix A.2.1. Note that a separable characteristic function does not always separate in a z-dependent and z-independent factor, an example will be given in Section 6.5.

Performing the inverse counting statistics at $s = 1$ with the correct values $M = 2$ and $D = 1$ of the spinless model gives the spectrum depicted in Figure 6.2 (b). The input information is given by the scaled finite-time cumulants $C_{s,m}(t)/t$ from order 0 to 3. For $\Gamma t = 100$, the long-time limit is reached and no difference to the exact eigenvalues can be recognized anymore.

For the consistency check of the dimensions M and D, we use as input information the calculated scaled cumulants at $\Gamma t = 200$. Horizontal contour lines in Figure 6.4 (a), (b) indicate that the eigenvalues are independent of s, i.e., the assumed dimensions $M = 2$ and $D = 1$ are compatible with the input data. In contrast for the choice $M = 3$ and $D = 1$, see Figure 6.4 (c), (d), (e), the eigenvalue λ_3 is strongly s-dependent. Since not the full spectrum is s-independent, the dimension $M = 3$ is too large.

For completeness, we discuss in Appendix A.3.2 how close the magnetic field has to be tuned to $\Delta = 0$ in order to observe the discussed behavior.

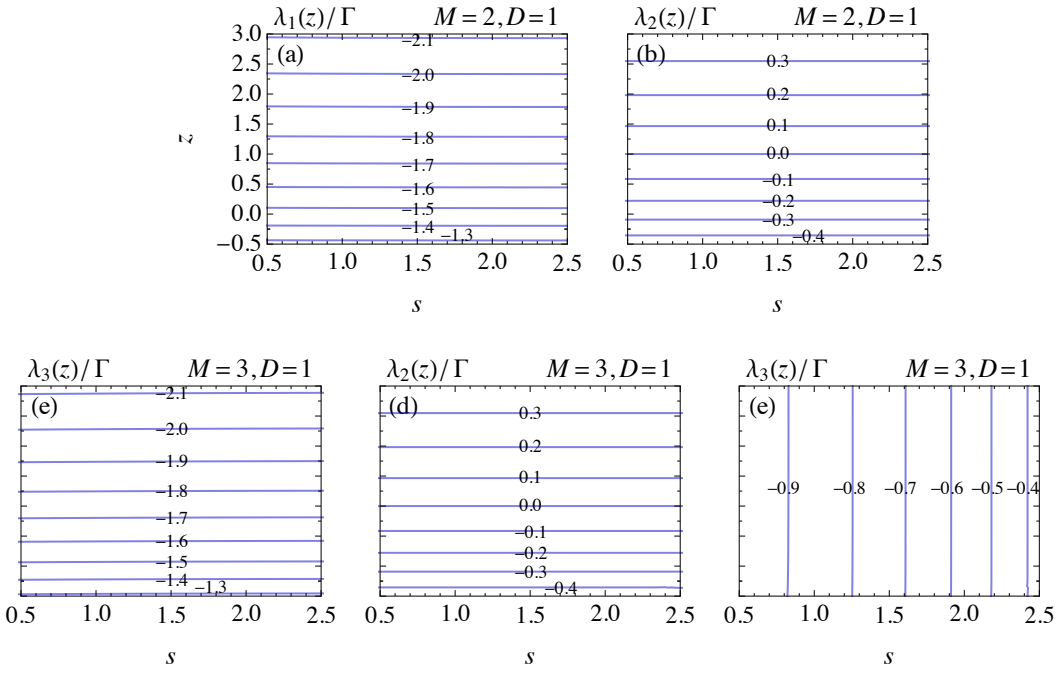

Figure 6.4: Consistency check of the number of system states M and the counting power D for the single-level quantum dot $\varepsilon = -k_\mathrm{B}T$ without magnetic field for time $\Gamma t = 200$. Assuming different values for M and D, contour lines of the resulting $j = 1, \ldots, M$ eigenvalues $\lambda_j(z)/\Gamma$ are depicted. The eigenvalues for $M = 2$, $D = 1$ in (a), (b) are s-independent, the ones for $M = 3$, $D = 1$ in (c), (d), (e) are *not* all s-independent.

6.5 Sequential and Andreev tunneling in a single-electron box

The second example illustrating the inverse counting-statistics procedure is the set-up introduced in Section 5.3 and depicted in Figure 5.2 (a). The corresponding stochastic system is depicted in Figure 5.2 (b). Its generator is given by

$$\mathbf{W}_z = \begin{pmatrix} -\Gamma_\mathrm{A}^+ - \Gamma_\mathrm{d}^+ & z\Gamma_\mathrm{u}^- & z^2\Gamma_\mathrm{A}^- \\ \Gamma_\mathrm{d}^+ & -\Gamma_\mathrm{u}^+ - \Gamma_\mathrm{u}^- & z\Gamma_\mathrm{d}^- \\ \Gamma_\mathrm{A}^+ & \Gamma_\mathrm{u}^+ & -\Gamma_\mathrm{A}^- - \Gamma_\mathrm{d}^- \end{pmatrix} . \tag{6.11}$$

Each counting factor z in the upper-right off-diagonal matrix elements correspond to counting an electron leaving the island. Since two electrons are transferred in each Andreev-tunneling process, Γ_A^- is multiplied with the square z^2 instead of a single z.

The characteristic function is a polynomial of order $M = 3$ in λ and of order $D = 2$ in z. In general, the inverse counting statistics should deliver all three z-dependent eigenvalues.

Instead of calculating the tunneling rates $\Gamma_\mathrm{u}^\pm$, $\Gamma_\mathrm{d}^\pm$, and $\Gamma_\mathrm{A}^\pm$ in the presence of an electromagnetic environment [31, 99], we rely on experimentally measured rates for $n_\mathrm{G} = 0.09$ in Ref. [32] and $n_\mathrm{G} = 0.00$ in Ref. [5]. In the former case, the experimental parameters are $n_\mathrm{G} = 0.09$, $E_\mathrm{C} = 43\,\mu\mathrm{eV}$, $R_\mathrm{T} = 2000\,\mathrm{k}\Omega$, and $\Delta = 216\,\mu\mathrm{eV}$ at 60 mK temperature. The measured rates are $\Gamma_\mathrm{u}^+ = 10.5\,\mathrm{Hz}$, $\Gamma_\mathrm{u}^- = 7.2\,\mathrm{Hz}$, $\Gamma_\mathrm{d}^+ = 1270\,\mathrm{Hz}$, $\Gamma_\mathrm{d}^- = 730\,\mathrm{Hz}$, $\Gamma_\mathrm{A}^+ = 460\,\mathrm{Hz}$, and $\Gamma_\mathrm{A}^- = 23.0\,\mathrm{Hz}$. In the latter case, the experimental parameters are

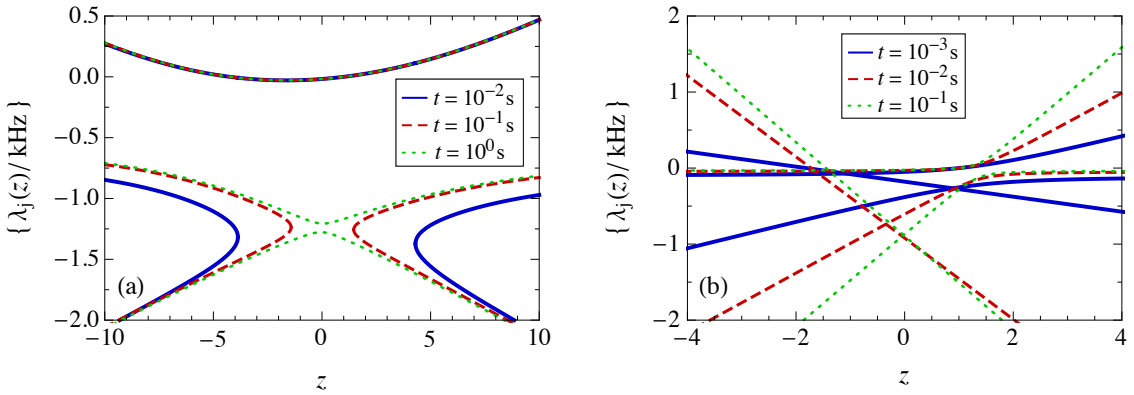

Figure 6.5: Eigenvalue spectrum obtained via inverse counting statistics for a normal-state metallic island weakly tunnel coupled to one superconducting lead. The gate charge is (a) $n_G = 0.09$ and (b) $n_G = 0.00$. The input data are scaled cumulants $C_{s,m}(t)/t$ for finite times t. Only in the long-time limit, (a) $t \gtrsim 10^0\,\mathrm{s}$ and (b) $t \gtrsim 10^{-1}\,\mathrm{s}$, the output $\{\lambda_j\}$ is indeed the eigenvalue spectrum of the generator Eq. (6.11). Values λ_j with a finite imaginary part [occurring near $z = 0$ in (a)] are not depicted.

$n_G = 0.00$, $E_C = 40\,\mu\mathrm{eV}$, $R_T = 490\,\mathrm{k\Omega}$, and $\Delta = 210\,\mu\mathrm{eV}$ at 50 mK temperature. The rates are $\Gamma_u^+ = \Gamma_u^- = \Gamma_u = 12\,\mathrm{Hz}$, $\Gamma_d^+ = \Gamma_d^- = \Gamma_d = 252\,\mathrm{Hz}$, and $\Gamma_A^+ = \Gamma_A^- = \Gamma_A = 615\,\mathrm{Hz}$.

6.5.1 Non-symmetric case

We start with discussing the generic, non-symmetric case, for which we choose the $n_G = 0.09$. The input information for the inverse counting statistics (for $M = 3$ and $D = 2$) is given by the scaled long-time generalized factorial cumulants $c_{s,m}$ from order 0 up to order $(D+1)M - 1 = 8$. Similar to the case of the single-level quantum dot discussed in Section 6.4, we take into account that the measurement time is always finite in an experiment and do not take as input parameters the exact scaled long-time cumulants of the defined model but calculate, instead, the scaled cumulants $C_{s,m}(t)/t$ at some large but finite time.

First, we determine the eigenvalue spectrum from the inverse counting statistics performed at $s = 1$ and assuming the correct values $M = 3$ and $D = 2$. As input parameters, we take the calculated scaled generalized factorial cumulants at times $t = 0.01, 0.1, 1\,\mathrm{s}$. The result is shown in Figure 6.5 (a). For $t = 1\,\mathrm{s}$, no difference to the exact eigenvalues can be recognized anymore.

Next, we demonstrate the consistency check for the dimensions M and D. For the correct values, all eigenvalues must be s-independent. In the following, we always use as input information the calculated scaled cumulants at $t = 10\,\mathrm{s}$. To show simultaneously both the z- and the s-dependence of the eigenvalues, we plot in the following figures contour lines for λ (in units of kHz). Horizontal contour lines indicate that the eigenvalues are independent of s, i.e., the assumed dimensions M and D are compatible with the input data.

In Figure 6.6 (a), (b), we show the result for the choice $M = 2$ and $D = 2$. Since the dimension M of the stochastic systems is taken too small, the resulting eigenvalues

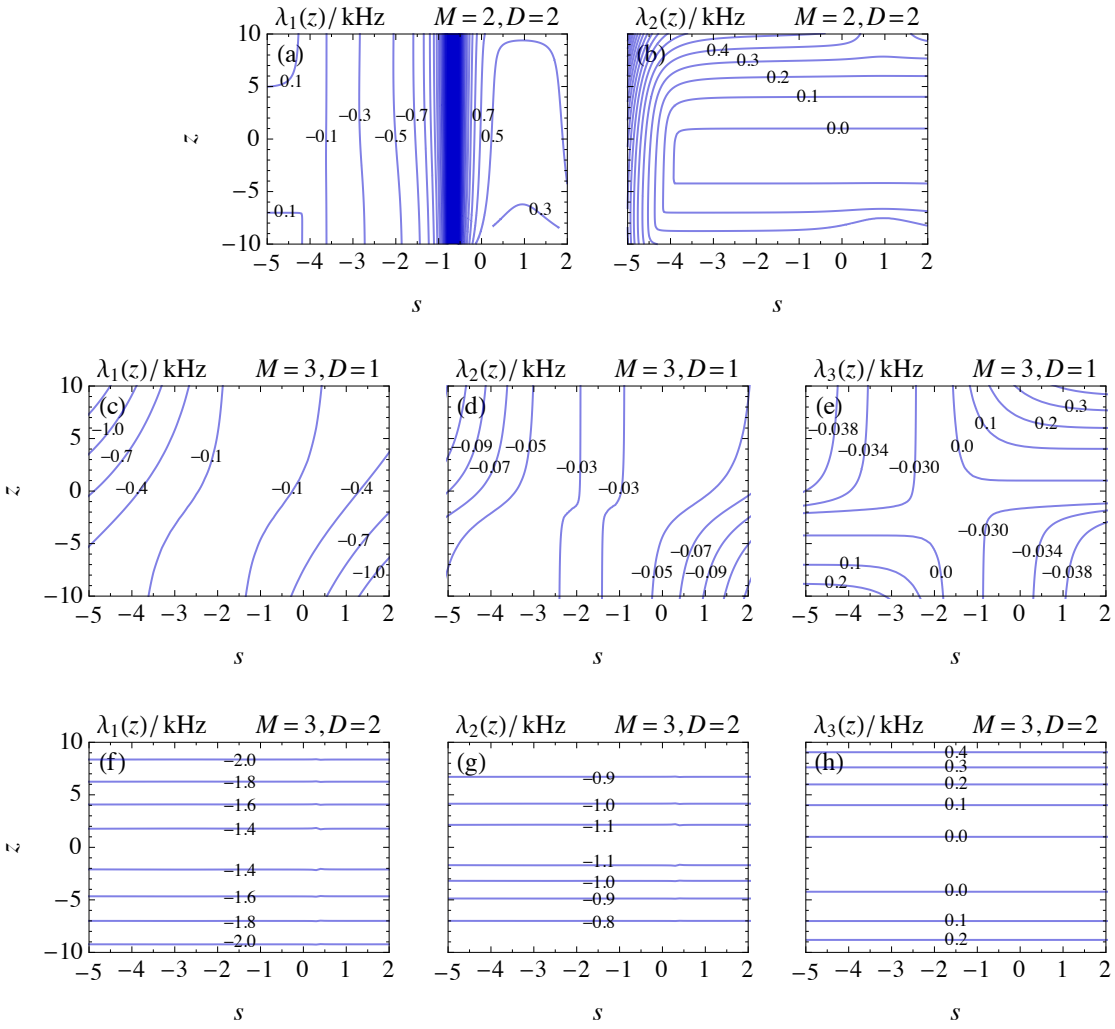

Figure 6.6: Consistency check of the number of system states M and the counting power D for the single-electron box with nonvanishing gate charge $n_\mathrm{G} = 0.09$ for time $t = 10\,\mathrm{s}$. Assuming different values for M and D, contour lines of the resulting $j = 1, \ldots, M$ eigenvalues $\lambda_j(z)/\,\mathrm{kHz}$ are depicted. The eigenvalues for $M = 2$, $D = 2$ in (a), (b) are strongly s-dependent, for $M = 3$, $D = 1$ in (c), (d), (e) as well, but the eigenvalues for $M = 3$, $D = 2$ in (f), (g), (h) are s-independent.

display a strong s-dependence. The same holds true for the choice $M = 3$ and $D = 1$, see Figure 6.6 (c), (d), (e). In this case, the counting power D characterizing the coupling to the detector is taken too small, and, again, the resulting eigenvalues are s-dependent. Only if we take the proper values $M = 3$ and $D = 2$, see Figure 6.6 (f), (g), (h), we get s-independent results.

6.5.2 Symmetric case

The symmetry point $n_\mathrm{G} = 0$ is special. At this point, there are only three different rates $\Gamma_\mathrm{A} = \Gamma_\mathrm{A}^+ = \Gamma_\mathrm{A}^-$, $\Gamma_\mathrm{d} = \Gamma_\mathrm{d}^+ = \Gamma_\mathrm{d}^-$, and $\Gamma_\mathrm{u} = \Gamma_\mathrm{u}^+ = \Gamma_\mathrm{u}^-$. As a consequence, the characteristic

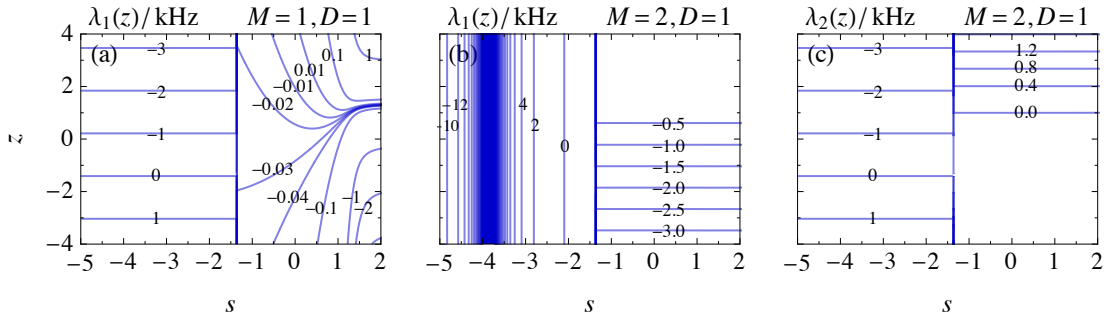

Figure 6.7: Consistency check of the number of system states M and the counting power D for the single-electron box with vanishing gate charge $n_\mathrm{G} = 0$ for time $t = 20\,\mathrm{s}$. Assuming different values for M and D, contour lines of the resulting $j = 1, \ldots, M$ eigenvalues $\lambda_j(z)/\,\mathrm{kHz}$ are depicted. The eigenvalue for $M = 1$, $D = 1$ in (a) and the two eigenvalues for $M = 2$, $D = 1$ in (b), (c).

function becomes separable,

$$\chi(z,\lambda) = \chi_{1,2}(z,\lambda)\cdot\chi_3(z,\lambda) \tag{6.12}$$

$$\chi_{1,2}(z,\lambda) = \lambda^2 + [(1-z)\Gamma_\mathrm{A} + \Gamma_\mathrm{d} + 2\Gamma_\mathrm{u}]\lambda + 2(1-z)\Gamma_\mathrm{u}(\Gamma_\mathrm{A} + \Gamma_\mathrm{d}) \tag{6.13}$$

$$\chi_3(z,\lambda) = \lambda + (1+z)\Gamma_\mathrm{A} + \Gamma_\mathrm{d}\,. \tag{6.14}$$

The first factor is a polynomial of order $M = 2$ in λ and of order $D = 1$ in z, while the second one is of order $M = 1$ and $D = 1$. Away from the symmetry point, $n_\mathrm{G} \neq 0$, the generator is not separable.

The choice of s determines whether the eigenvalue with the largest real part is a zero of the first or the second factor and, therefore, which and how many of the eigenvalues are accessible via the inverse counting statistics. If we choose $s = 1$ (corresponding to factorial cumulants), then we obtain only two of the three eigenvalues. For small $s < -1.36$ (for Figure 6.5 (b), we choose $s = -2$), we get only the third one. The number of required cumulants is 4 in the former and 2 in the latter case. The resulting spectrum of all three eigenvalues is depicted in Figure 6.5 (b) for the times $t = 0.001, 0.01, 0.1\,\mathrm{s}$. For $t = 0.1\,\mathrm{s}$, no difference to the exact eigenvalues can be recognized anymore.

The consistency check of the dimensions M and D (for $t = 20\,\mathrm{s}$) is depicted in Figure 6.7 (a) for $M = 1$ and $D = 1$ and in Figure 6.7 (b), (c) for $M = 2$ and $D = 1$. If we perform the inverse counting statistics around $s = 1$ (or for any $s > -1.36$), then we conclude that the dimension $M = 1$ is too small (no horizontal contour lines in Figure 6.7 (a) for $s > -1.36$), but $M = 2$ seems to be sufficient (horizontal contour lines in Figs. 6.7 (b) and (c) for $s > -1.36$). Thus, by employing only factorial cumulants ($s = 1$) one may be tempted to conclude that the dimension of the stochastic system is $M = 2$ only. If, on the other hand, inverse counting statistics is also done for $s < -1.36$, then the horizontal contour lines in Figure 6.7 (a) indicate that there is another eigenvalue. Since the obtained z-dependent eigenvalues are different from each other, we conclude that there must be, in total, three eigenvalues.

For completeness, we estimate in Appendix A.3.3 how close n_G has to be tuned to zero in order to observe the discussed behavior.

6.6 Inverse-counting-statistics manual

For practical use, we summarize the inverse-counting-statistics procedure introduced in this chapter in the following step-by-step manual:

(i) Some positive integer values for the number of system states M and the counting power D are assumed.

(ii) From the measured probability distribution $P_N(t)$, the scaled *finite time* cumulants $C_{s,m}(t)/t$ of order $m = 0, \ldots, (D+1)M - 1$ for some real s are calculated, see Eqs. (3.38) and (3.40). The time t is chosen large enough for $C_{s,m}(t)/t$ to become time independent such that $C_{s,m}(t)/t \approx c_{s,m}$.

(iii) From the $c_{s,m}$ the set of linear Eqs. (6.5) is derived.

(iv) Solving this set for the coefficients $a_{\mu\nu}$ yields the characteristic function $\chi(z, \lambda)$ defined in Eq. (6.3).

(v) Solving $\chi(z, \lambda_j) = 0$ yields the zeros $\lambda_j(z)$.

If the z-dependence of *each* zero $\lambda_j(z)$ is independent of the parameter s chosen in step (ii), the values assumed in step (i) are lower bounds for M and D. Moreover, the $\lambda_j(z)$ are, indeed, eigenvalues of the system's generator $\mathbf{W}_z$ and $\lambda - \lambda_j(z)$ linear factors of the generator's characteristic function. The $\lambda_j(1)$ are the system's relaxation rates. If the z-dependence is *not* independent of the parameter s, the assumption in (i) is falsified. One needs to start again at step (i) increasing, successively, from small values for M and/or D to larger values.

There are special cases of separable characteristic functions, see Section 6.5, where different intervals of s-values reveal different dimensions and eigenvalues of the generator. The total dimension and full spectrum is, then, obtained by combining the results from the different s-intervals.

6.7 Conclusions

In this chapter, we propose inverse counting statistics based on generalized factorial cumulants as a convenient and powerful tool to reconstruct characteristic features of a stochastic system from measured counting statistics of some of the system's transitions. Such a method is particularly useful in cases in which very little is a priori known about the stochastic system under investigation. As the only input information for the inverse counting-statistics procedure, we use a few experimentally determined numbers, namely the scaled generalized factorial cumulants in the long-time limit. Despite the limited amount of input, the inverse counting-statistics procedure yields a remarkable extended amount of output. First, we can determine a lower bound of M, the dimension of the stochastic system. Second, we can find a lower bound of the counting power D, which characterizes the coupling between stochastic system and detector. Third, we can reconstruct the characteristic function $\chi(z, \lambda)$ of the generator $\mathbf{W}_z$, which is a polynomial of order M in λ and a polynomial of order D in z. From the zeros of the characteristic function, we can, then, determine the full z-dependence of the full spectrum of eigenvalues of $\mathbf{W}_z$. This is quite a

remarkable result, since the long-time cumulants used as input depend only on one of the eigenvalues, $\lambda_{\max}$, determined around one value of z.

The use of generalized factorial cumulants instead of ordinary ones is crucial for our proposal. While the evaluation of generalized factorial cumulants from a measured time trace of the detector signal does not introduce any extra complication as compared to the evaluation of ordinary cumulants, the benefit of having a free parameter s in the definition of the generalized factorial cumulants is immense. First, the outcome of the inverse counting statistics must be s-independent. Therefore, an s-dependent outcome of the inverse counting statistics immediately indicates a wrong choice of M or D. Second, there are special cases of separable characteristic functions, for which the inverse counting statistics with ordinary cumulants would only reveal a part of the spectrum of eigenvalues of the generator, while the variation of s makes it possible to access the full spectrum.

The proposed inverse counting-statistics procedure is quite general and, therefore, applicable to a large variety of systems. To illustrate the procedure we chose two examples from electronic transport in nanostructures: a single-level quantum dot in a Zeeman field and a single-electron box subjected to sequential and Andreev tunneling. For the latter case, the full dimension of the system's state space and the full spectrum of eigenvalues can only be revealed by varying the parameter s.

7 Detection of coherent oscillations via generalized factorial cumulants

In this chapter, we discuss the detection of coherent oscillations for the electron transport through a quantum dot spin-valve.

In Section 7.1, we give an introduction to coherent oscillations typically observed in the waiting-time distribution $\omega(\tau)$, i.e., the probability that two subsequent events measured by some detector are separated by the time interval $[0, \tau]$. The waiting times oscillate due to the presence of quantum-mechanical coherences between different system states. We concentrate in this chapter on the single-level quantum-dot spin valve as introduced in Section 7.2. The coherent oscillations can be explained as the Larmor precession of the quantum-dot spin in a virtual magnetic field. Each oscillation in the waiting time corresponds to an oscillation between different directions of the spin.

In Section 7.3, we explain how coherent oscillations can be identified in the generalized factorial cumulants $C_{s,m}(t)$. The big advantage of the generalized factorial cumulants is that they can distill out of a large number of transferred electrons exactly those few being coherently transferred, i.e., those causing coherent oscillations. Other quantities typically used to detect coherent oscillations like the waiting times, charge current, finite-frequency noise, and ordinary cumulants miss this property. Thus, in comparison to these conventional quantities, we observe that the sensitivity increases dramatically if generalized factorial cumulants are studied.

The publication of the results presented in this chapter is in preparation.

7.1 Introduction

In the previous chapters, we have studied transport through nanostructures determined by the stochastic appearance of transitions between different states. Such analysis can be extended to any other system governed by stochastic transitions between some states, independent from the physical nature of these states. Quantum-mechanical effects need not to be relevant. In contrast, in this chapter, we study a completely quantum-mechanical effect: the contribution of coherences (i.e., quantum-mechanical superpositions of different states) to electron transport typically leading to oscillating waiting times. Such coherent oscillations can arise for the electron transport through double-quantum dots [116], where coherences between states localized in the different dots appear. If a quantum dot is contacted with a normal and a superconducting lead, coherent oscillations have been predicted [117, 118] due to the coherences between the empty and doubly occupied dot.

In the following, we concentrate on the quantum-dot spin valve depicted in Figure 7.1. Quantum-dot spin valves have been experimentally realized by metallic nanoparticles [119, 120], semiconductor quantum dots [121], molecules [122, 123], Ge/Si nanowires [124], InAs

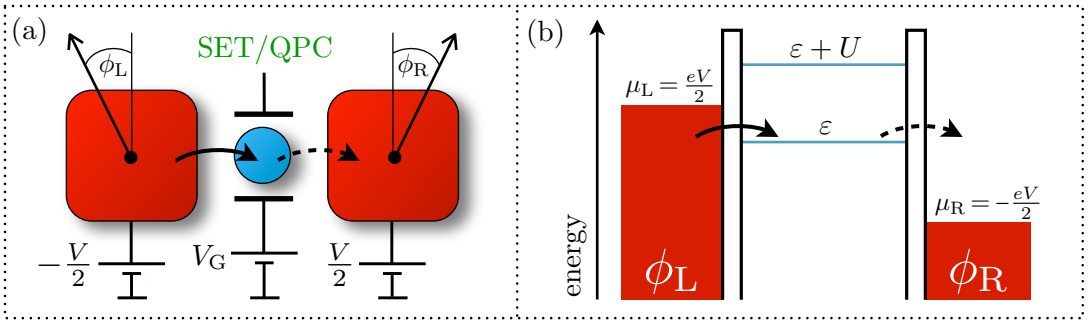

Figure 7.1: (a) Set-up and (b) energy levels of the studied spin-valve. A single-level quantum dot (blue) is weakly tunnel coupled to two ferromagnetic leads (red) with noncollinear magnetizations enclosing the angle $\phi = \phi_L - \phi_R$. The bias voltage V is so *large* that electrons are transferred unidirectionally through the dot. The level is either empty or singly occupied. The voltage V is so *small* that the doubly occupied level is only a virtual intermediate state. Dashed lines indicate transitions counted by a detector SET or QPC (green).

nanowires [125], and carbon nanotubes [126–130]. Coherent oscillations [131] are caused by the superposition between two different spin states of the quantum dot, the dot is either occupied by a single spin $\uparrow$ or single spin $\downarrow$ electron. Since coherences arise between different spin and *not* between different charge states (as it is the case for the double dot [116] and the superconducting [117, 118] system), charge detection by means of a single-electron transistor or quantum point contact does not destroy these coherences. In this sense, a quantum-dot spin valve is an ideal system to study coherent oscillation by means of full counting statistics or waiting times.

The coherent oscillations do not only manifest in the waiting times [131], but also in the charge current [132–140], zero- or finite-frequency current noise [141–143], and ordinary higher-order cumulants [144]. However, all these quantities detect the coherent oscillations only for a strongly spin-blockaded spin valve, i.e., large spin polarization p of the leads' magnetizations and large asymmetries between the tunnel-coupling strengths. Away from this parameter regime, they are not affected by coherent oscillations due to their minor contribution to overall electron transport. Thus, one may wonder if the coherences drop out of the transport situation?

In the present chapter, we point out that the sensitivity for coherent oscillations increases drastically if generalized factorial cumulants are studied. The presence of the coherent oscillations can be proven even for arbitrary weak polarizations (e.g, Fe, Co, Ni [145]) and small tunnel-coupling asymmetries. The advantage of generalized factorial cumulants is their dependence on the parameter s. By varying this parameter, the different electron-transport processes can be studied separately. Especially, the coherently transferred electrons can be distilled out of the total electron transport.

7.2 Model and technique

The quantum-dot spin valve studied in this chapter is depicted in Figure 7.1 (a). A single-level quantum dot is weakly tunnel coupled to a left $r = \mathrm{L}$ and right $r = \mathrm{R}$ ferromagnetic

lead. We assume in the following that the ferromagnets consist of the same material and therefore their degrees of spin polarizations are identical $p_{\mathrm{L}} = p_{\mathrm{R}} = p > 0$. The polarization for a normal metal is $p = 0$ and for a half-metallic ferromagnet with majority spins only $p = 1$. The tunnel-coupling strengths to the left and right lead $\Gamma_{\mathrm{L/R}} = (1 \pm a)\Gamma/2$ can be expressed by the asymmetry $a := (\Gamma_{\mathrm{L}} - \Gamma_{\mathrm{R}})/\Gamma$ with $\Gamma = \Gamma_{\mathrm{L}} + \Gamma_{\mathrm{R}}$. If we choose the inverse $1/\Gamma$ as unit of time, only the single parameter a determines the tunnel coupling between leads and dot.

The energy necessary to occupy the single-level quantum dot by one electron is denoted by ε, see Figure 7.1 (b). For the occupation with a second electron, the energy $\varepsilon + U$ has to be provided. The charging energy U accounts for the Coulomb interaction between the two electrons. The energy ε can be tuned by the gate voltage V_{G}, see Figure 7.1 (a). A bias voltage is symmetrically applied between the leads such that their electrochemical potentials become $\mu_{\mathrm{L}} = -\mu_{\mathrm{R}} = eV/2 > 0$.

Each lead is modeled as reservoirs of noninteracting electrons. The occupation probability of the corresponding levels is given by the Fermi function $f_r(x) = \{1 + \exp[(x - \mu_r)/k_{\mathrm{B}}T]\}^{-1}$. The bias voltage is so large that $f_r(\varepsilon)$ is one (zero) for the left (right) lead. However, the voltage is still so small that $f_r(\varepsilon + U) = 0$ and therefore the occupation probability of the dot with two excess electrons is vanishing. In summary, the bias voltage is chosen as $\varepsilon \ll eV/2 \ll \varepsilon + U$.

The precise details of the underlying microscopic model are given in Section 4.1. A nearly identical system has been studied in Section 4.3. There, the magnetization of leads have pointed in parallel $\mathbf{n}_{\mathrm{L}} \uparrow\uparrow \mathbf{n}_{\mathrm{R}}$ or antiparallel $\mathbf{n}_{\mathrm{L}} \uparrow\downarrow \mathbf{n}_{\mathrm{R}}$ directions, i.e., they have been collinear. Here, the leads' magnetizations point in arbitrary directions enclosing the angle $\phi = \phi_{\mathrm{L}} - \phi_{\mathrm{R}}$. Thus, the tunneling Hamiltonian given in Eq. (4.4) includes not a spin-1/2 rotation matrix $D^{1/2}(\alpha, \beta, \gamma)$ which is equal to the identity matrix anymore. We choose in the following the spin-quantization axis of each ferromagnetic lead parallel to the respective magnetization. For the dot, we choose a spin-quantization axis perpendicular to the leads' magnetizations. Hence, the Euler angle are $\alpha = 0$, $\beta = -\pi/2$, and $\gamma = -\phi_r$.

Starting with the Hamiltonian given in Eq. (4.1), the full counting statistics can be simulated by means of a master equation. The procedure outlined in Section 3.6 accounts for systems that can be characterized by the diagonal elements of the reduced density matrix of the dot $p^{\chi}(t) := p^{\chi\chi}(t) = \langle\chi| \operatorname{Tr}_{\mathrm{L}}\operatorname{Tr}_{\mathrm{R}}[\rho(t)] |\chi\rangle$, where the left and right leads' degrees of freedom have been traced out from the density matrix $\rho(t)$ of the full system. For noncollinear magnetizations $\phi \neq 0, \pi$, also coherences, i.e., off diagonal reduced density matrix elements $p^{\chi_1\chi_2}(t) = \langle\chi_1| \operatorname{Tr}_{\mathrm{L}}\operatorname{Tr}_{\mathrm{R}}[\rho(t)] |\chi_2\rangle$, have to be taken into account. Thus, the system is described by the *generalized* master equation

$$\dot{p}^{\chi_1\chi_2}(t) = \sum_{\chi_1',\chi_2'} \Gamma^{\chi_1\chi_1'}_{\chi_2\chi_2'} p^{\chi_1'\chi_2'}(t)\,, \tag{7.1}$$

with the generalized transition rates $\Gamma^{\chi_1\chi_1'}_{\chi_2\chi_2'}$, which can be obtained by a diagrammatic technique [89–93]. For the spin valve, the corresponding diagrammatic rules are given in Ref. [88, Section 4.5]. With the dot states $\chi = 0, \uparrow, \downarrow$, the generalized master equation

reads

$$\begin{aligned}
\dot{p}^{00}(t) &= -2\Gamma_{\mathrm{L}} p^{00}(t) + \Gamma_{\mathrm{R}} p^{\uparrow\uparrow}(t) + \Gamma_{\mathrm{R}} p^{\downarrow\downarrow}(t) + p\Gamma_{\mathrm{R}} e^{i\phi_{\mathrm{R}}} p^{\uparrow\downarrow}(t) + p\Gamma_{\mathrm{R}} e^{i\phi_{\mathrm{R}}} p^{\downarrow\uparrow}(t)\,, \\
\dot{p}^{\uparrow\uparrow}(t) &= \Gamma_{\mathrm{L}} p^{00}(t) - \Gamma_{\mathrm{R}} p^{\uparrow\uparrow}(t) + \gamma_{-+} p^{\uparrow\downarrow}(t) + \gamma_{+-} p^{\downarrow\uparrow}(t)\,, \\
\dot{p}^{\downarrow\downarrow}(t) &= \Gamma_{\mathrm{L}} p^{00}(t) - \Gamma_{\mathrm{R}} p^{\downarrow\downarrow}(t) + \gamma_{++} p^{\uparrow\downarrow}(t) + \gamma_{--} p^{\downarrow\uparrow}(t)\,, \\
\dot{p}^{\uparrow\downarrow}(t) &= p\Gamma_{\mathrm{L}} e^{-i\phi_{\mathrm{L}}} p^{00}(t) + \gamma_{--} p^{\uparrow\uparrow}(t) + \gamma_{+-} p^{\downarrow\downarrow}(t) - \Gamma_{\mathrm{R}} p^{\uparrow\downarrow}(t)\,, \\
\dot{p}^{\downarrow\uparrow}(t) &= p\Gamma_{\mathrm{L}} e^{-i\phi_{\mathrm{L}}} p^{00}(t) + \gamma_{++} p^{\uparrow\uparrow}(t) + \gamma_{-+} p^{\downarrow\downarrow}(t) - \Gamma_{\mathrm{R}} p^{\downarrow\uparrow}(t)\,,
\end{aligned} \tag{7.2}$$

with the generalized transition rates

$$\gamma_{\mu\nu} = \mu \frac{i}{2} \left(B_{\mathrm{L}} e^{\nu i \phi_{\mathrm{L}}} + B_{\mathrm{R}} e^{\nu i \phi_{\mathrm{R}}} + \mu i p \Gamma_{\mathrm{R}} e^{\nu i \phi_{\mathrm{R}}} \right)\,, \tag{7.3}$$

$$B_r = \frac{p\Gamma_r}{\pi} \mathrm{Re}\left[\Psi\left(\frac{1}{2} + i \frac{\varepsilon + U - \mu_r}{2\pi k_{\mathrm{B}} T} \right) - \Psi\left(\frac{1}{2} + i \frac{\varepsilon - \mu_r}{2\pi k_{\mathrm{B}} T} \right) \right] \tag{7.4}$$

given by the digamma function $\Psi(x)$. The energy $\varepsilon + U$ enters the master equation via Eq. (7.4) since the doubly occupied dot level must be taken into account as virtual intermediate state.

The role of the coherences can be analyzed in more detail by inspecting the average quantum-dot spin $\mathbf{S}(t) = (S_x, S_y, S_z)^T(t)$ with

$$S_x(t) = \frac{p^{\uparrow\downarrow}(t) + p^{\downarrow\uparrow}(t)}{2}, \quad S_y(t) = i\frac{p^{\uparrow\downarrow}(t) - p^{\downarrow\uparrow}(t)}{2}, \quad S_z(t) = \frac{p^{\uparrow\uparrow}(t) - p^{\downarrow\downarrow}(t)}{2}\,. \tag{7.5}$$

The generalized master equation (7.2) yields for the time evolution of the spin [132]

$$\dot{\mathbf{S}}(t) = \dot{\mathbf{S}}_{\mathrm{acc}}(t) + \dot{\mathbf{S}}_{\mathrm{rel}}(t) + \dot{\mathbf{S}}_{\mathrm{prec}}(t)\,, \tag{7.6}$$

with

$$\dot{\mathbf{S}}_{\mathrm{acc}}(t) = p\Gamma_{\mathrm{L}} p^{00}(t) \mathbf{n}_{\mathrm{L}} - p\Gamma_{\mathrm{R}} \frac{p^{\uparrow\uparrow}(t) + p^{\downarrow\downarrow}(t)}{2} \mathbf{n}_{\mathrm{R}}\,, \tag{7.7}$$

$$\dot{\mathbf{S}}_{\mathrm{rel}}(t) = -\Gamma_{\mathrm{R}} \mathbf{S}(t)\,, \tag{7.8}$$

$$\dot{\mathbf{S}}_{\mathrm{prec}}(t) = \mathbf{S}(t) \times \mathbf{B}\,. \tag{7.9}$$

The first term Eq. (7.7) describes the spin accumulation on the dot via tunneling in from the left lead and tunneling out to the right lead. The second term Eq. (7.8) accounts for the relaxation of the dot spin by tunneling out events. The last term Eq. (7.9) leads to a precession of the dot spin in the virtual magnetic field

$$\mathbf{B} = B_{\mathrm{L}} \mathbf{n}_{\mathrm{L}} + B_{\mathrm{R}} \mathbf{n}_{\mathrm{R}}\,. \tag{7.10}$$

It is also referred to as exchange field due to the virtual electron exchange between the dot and the leads. The origin of the coherent oscillations is this spin-precession term. Electrons entering the dot have a spin preferably parallel to $\mathbf{n}_{\mathrm{L}}$. Since the magnetization of the right lead points in the different direction $\mathbf{n}_{\mathrm{R}}$, the electron are hindered to leave the dot, i.e., the dot is in spin blockade [132]. Due to the precession in the virtual magnetic field, the dot spin periodically aligns with $\mathbf{n}_{\mathrm{R}}$ and the spin blockade is periodically lifted. As a result, some electrons are coherently transferred through the spin valve.

If the leads' magnetizations are aligned collinearly $\phi = 0, \pi$, the coherent oscillations vanish in the stationary limit. The reason is the spin becoming also collinear to $\mathbf{n}_r$. Thus, the precession term Eq. (7.9) can be neglected and the dynamics of the system can be described by a diagonal density matrix.

From the generalized master equation, cumulants can be derived as outlined in Section 3.6. The N-resolved generalized master equation can be obtained directly from Eq. (7.2). The z-transformed density-matrix elements $\mathbf{p}_z(t) = (p_z^{00}, p_z^{\uparrow\uparrow}, p_z^{\downarrow\downarrow}, p_z^{\uparrow\downarrow}, p_z^{\downarrow\uparrow})^T$ are determined by the generator

$$\mathbf{W}_z = \begin{pmatrix} -2\Gamma_\mathrm{L} & z\Gamma_\mathrm{R} & z\Gamma_\mathrm{R} & zp\Gamma_\mathrm{R}e^{i\phi_\mathrm{R}} & zp\Gamma_\mathrm{R}e^{-i\phi_\mathrm{R}} \\ \Gamma_\mathrm{L} & -\Gamma_\mathrm{R} & 0 & \gamma_{-+} & \gamma_{+-} \\ \Gamma_\mathrm{L} & 0 & -\Gamma_\mathrm{R} & \gamma_{++} & \gamma_{--} \\ p\Gamma_\mathrm{L}e^{-i\phi_\mathrm{L}} & \gamma_{--} & \gamma_{+-} & -\Gamma_\mathrm{R} & 0 \\ p\Gamma_\mathrm{L}e^{-i\phi_\mathrm{L}} & \gamma_{++} & \gamma_{-+} & 0 & -\Gamma_\mathrm{R} \end{pmatrix}. \tag{7.11}$$

Each counting factor z corresponds to counting an electron tunneling out of the quantum dot. The generating function takes the form presented in Eq. (3.53) with the vector $\mathbf{e}^T = (1, 1, 1, 0, 0)$ summing over the diagonal density-matrix elements. The stationary vector $\mathbf{p}_\mathrm{stat}$ is obtained from $\mathbf{W}_1\mathbf{p}_\mathrm{stat} = 0$ and $\mathbf{e}^T\mathbf{p}_\mathrm{stat} = 1$.

In the following section, we compare the sensitivity of the generalized factorial cumulants $C_{s,m}(t)$ for coherent oscillations to the commonly used quantities: ordinary (factorial) cumulants, finite-frequency current noise, and the waiting times.

The factorial cumulants $C_{1,m}$ can be calculated from the generating function Eq. (3.53) with $s = 1$. The ordinary cumulants are merely a linear combination of these cumulants, cf. Section 3.3. Therefore, we will discuss only the factorial cumulants in the next section.

The finite-frequency current noise is defined as the Fourier transform of the current auto-correlation function[1]

$$S(f) := \int_{-\infty}^{\infty} \mathrm{d}t \left[\langle I(t)I(0)\rangle + \langle I(0)I(t)\rangle\right] e^{-i2\pi ft}, \tag{7.12}$$

where the symmetrized current operator $I = (I_\mathrm{L} + I_\mathrm{R})/2$ is determined by the current operators of the left and right lead. The current noise can be simply obtained from the Fourier cosine transform of the second order ordinary cumulant, see Appendix A.4.1.

The waiting-time distribution $\omega(\tau)$ gives the probability that two subsequent tunneling out electrons are separated by the time interval τ. Similar to the cumulants, it can be directly obtained from a measured time trace. We simulate the waiting-time distribution by means of [116, Eq. (2.6)]

$$\omega(\tau) = \frac{\mathbf{e}^T\mathbf{W}^{(1)} \exp[(\mathbf{W}_1 - \mathbf{W}^{(1)})\tau]\mathbf{W}^{(1)}\mathbf{p}_\mathrm{stat}}{\mathbf{e}^T\mathbf{W}^{(1)}\mathbf{p}_\mathrm{stat}}, \tag{7.13}$$

with $\mathbf{W}^{(1)} = \partial_z\mathbf{W}_z$. In order to analyze the frequency spectrum of the waiting-time distribution, we study the amplitude of the Fourier transform [116, Eq. (2.11)]

$$\hat{\omega}(f) = \int_0^{\infty} \mathrm{d}\tau\omega(\tau)e^{-i2\pi f\tau} = \frac{\mathbf{e}^T\mathbf{W}^{(1)}[i2\pi f\mathbf{1} - (\mathbf{W}_1 - \mathbf{W}^{(1)})]^{-1}\mathbf{W}^{(1)}\mathbf{p}_\mathrm{stat}}{\mathbf{e}^T\mathbf{W}^{(1)}\mathbf{p}_\mathrm{stat}}. \tag{7.14}$$

[1] We avoid the symbol ω for the angular frequency since it also denotes the waiting-time distribution.

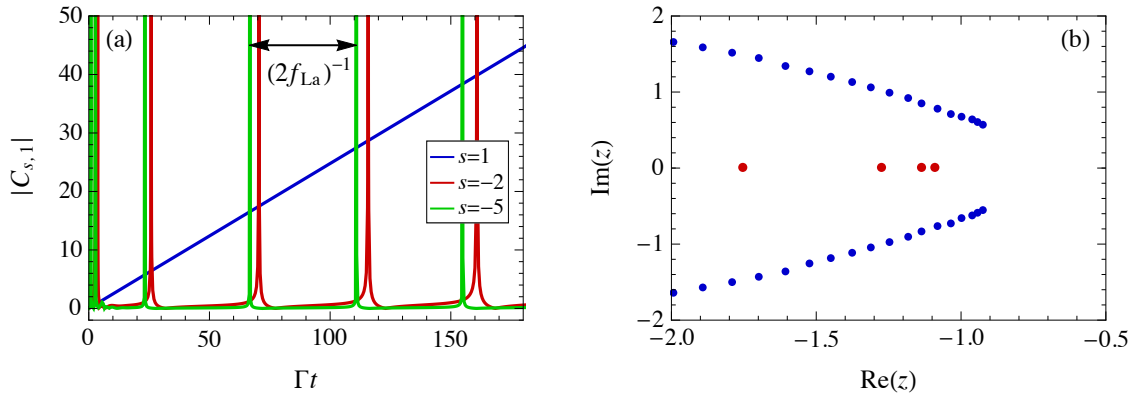

Figure 7.2: (a) Generalized factorial cumulants and (b) zeros z_j of $\mathcal{M}_{\mathrm{F}}(z,t)$. The parameters are $p = 3/10$, $a = 1/3$, $\phi = \phi_{\mathrm{L}} - \phi_{\mathrm{R}} = \pi/2$, $\varepsilon = 10\,k_{\mathrm{B}}T$, $U = 30\,k_{\mathrm{B}}T$, and $eV = 65\,k_{\mathrm{B}}T$. In (b), $t = 180/\Gamma$ with $\Gamma = \Gamma_{\mathrm{L}} + \Gamma_{\mathrm{R}}$. $C_{1,1} = \langle N\rangle = \langle I\rangle\, t$ is the mean number of transferred electrons. Each peak of the generalized factorial cumulants is due to one coherently transferred electron. For negative $s \lesssim -1$, these electrons [red zeros in (b)] are distilled out from the overwhelming number of other transfer events [blue zeros in (b)]. Other quantities in the literature are dominated by the blue zeros and therefore cannot detect the coherently transferred electrons.

7.3 Coherent oscillations in the spin valve

In Section 3.4, we have pointed out that the full counting statistics can always be decomposed into different zeros $z_j(t)$ of the factorial-moment generating function $\mathcal{M}_{\mathrm{F}}(z,t)$. By varying the parameter s of the generalized factorial cumulants $C_{s,m}(t)$, different zeros can be brought into focus, cf. Section 3.5. Especially, from an overwhelming number of different zeros, we can distill out those representing coherently transferred electrons. This is the main reason for the tremendous sensitivity of the $C_{s,m}$ for the coherent oscillations as illustrated in the following.

The generalized factorial cumulants for different parameters s in the case of a weak spin polarization $p = 0.3$ (e.g, Fe, Co, Ni [145]) are depicted in Figure 7.2 (a). The mean number of transferred electrons $C_{1,1}(t) = \langle N\rangle\,(t) = \langle I\rangle\, t \propto t$ shows no sign of oscillations. However, for $s \lesssim -1$, the behavior is different. After the decay of some initial fluctuations for $t \lesssim 10/\Gamma$,[2] we observe the periodic occurrence of peaks equidistantly in time. Their frequency does not change if we decrease s. By inspecting the eigenvalues of the generator Eq. (7.11), we obtain for the peaks' frequency

$$f_{\mathrm{La}} = \frac{|\mathbf{B}|}{2\pi} + \mathcal{O}\left(p^3\right)\,, \quad |\mathbf{B}| = \sqrt{B_{\mathrm{L}}^2 + B_{\mathrm{R}}^2 + 2B_{\mathrm{L}}B_{\mathrm{R}}\cos(\phi)}\,, \tag{7.15}$$

which is the Larmor frequency of the exchange field $\mathbf{B}$, cf. Appendix A.4.2. Each peak describes the coherent transfer of a single electron to the right lead by means of the exchange field. Out of the overall $\langle N\rangle \approx 40$ in average transferred electrons in time interval $[0, t \approx 180/\Gamma]$, we have distilled out the four coherently transferred electrons.

[2] The long-time limit is reached where $C_{1,m}/t$ are time independent.

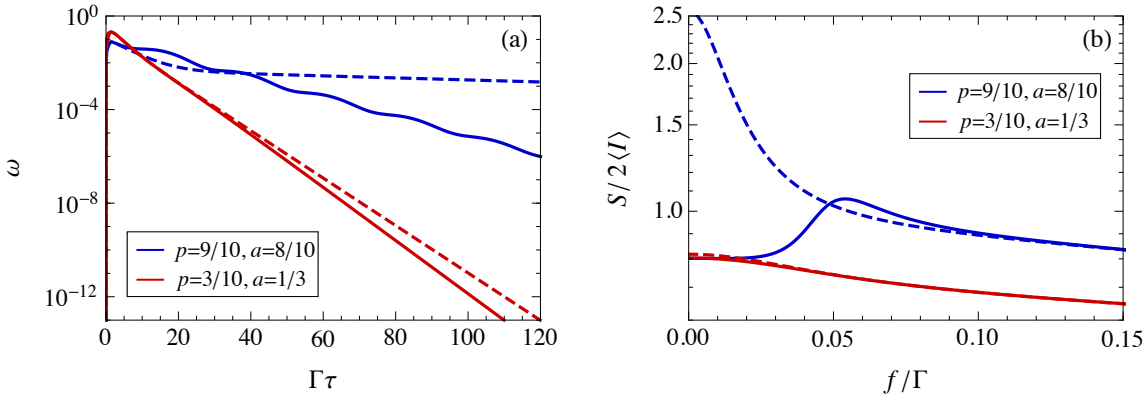

Figure 7.3: (a) Waiting-time distribution and (b) finite-frequency Fano factor. Two different choices for the polarization p and asymmetry a are depicted. Other parameters are as in Figure 7.2. For the dashed lines, coherences have been manually excluded ($B_\mathrm{L} = B_\mathrm{R} = 0$). For large p and a, coherent electron transfer is indicated by oscillating waiting times and a maximum in the Fano factor (solid blue lines). For small p and a, coherences cannot be recognized (nearly no difference between solid and dashed red line).

Such few coherently transferred electrons in the overall transport are hardly detected by ordinary (factorial) cumulants of higher order $m > 1$. This can be understood by inspecting the zeros $z_j(t)$ of the generating function $\mathcal{M}_\mathrm{F}(z,t)$. In Figure 7.2 (b), the 40 zeros with the smallest absolute value $|z_j(t)|$ are depicted. Each of the four red zeros represents one coherently transferred electron. The other blue zeros appear also for vanishing exchange field and have been studied already in Section 4.3. They describe incoherent electron transport processes. Taking Eq. (3.44) into account, we see that the factorial cumulants $C_{1,m}$ are dominated by the overwhelming number of blue zeros. With increasing order m, zeros with smaller absolute value become more relevant. However, since the blue zeros near $z = -0.9$ have the smallest absolute value, increasing the order m does not improve the sensitivity for the red zeros. In contrast, for $s \lesssim -1$, the red zeros yield the smallest values $|-z_j(t) + s - 1|$ and determine the $C_{s,m}$, i.e., the coherently transferred electrons are filtered out from the other electrons. With increasing order m, the dominating role of the red zeros is enhanced. However, the peaks as crucial feature appear independently of the order m. Thus, studying $C_{s,m}$ for $m = 1$ is completely sufficient.

For weak spin polarization, the number of incoherent blue zeros is typically larger than the number of coherent red zeros. We can even argue analytically that coherences enter the $C_{s,1}$ not before the order $\mathcal{O}\left(p^4\right)$ in the short- and long-time limit, see Appendix A.4.3. Especially for such low polarizations, it is necessary to decrease s.

Let us now comment on quantities commonly used to detect coherent oscillations: the waiting times and the finite-frequency noise. For large polarization p and asymmetry a, the coherent electron transfer can be identified by oscillating waiting times and a maximum of the finite-frequency Fano factor, see solid blue lines in Figure 7.3. If we manually exclude the coherences in our simulation, i.e., we set $B_\mathrm{L} = B_\mathrm{R} = 0$, such features vanish, see dashed blue lines in Figure 7.3. In contrast, for small p and a, taking coherences into account or not does not influence the waiting times and the finite-frequency Fano factor significantly. In this case, the solid and dashed red lines in Figure 7.3 are nearly identical.

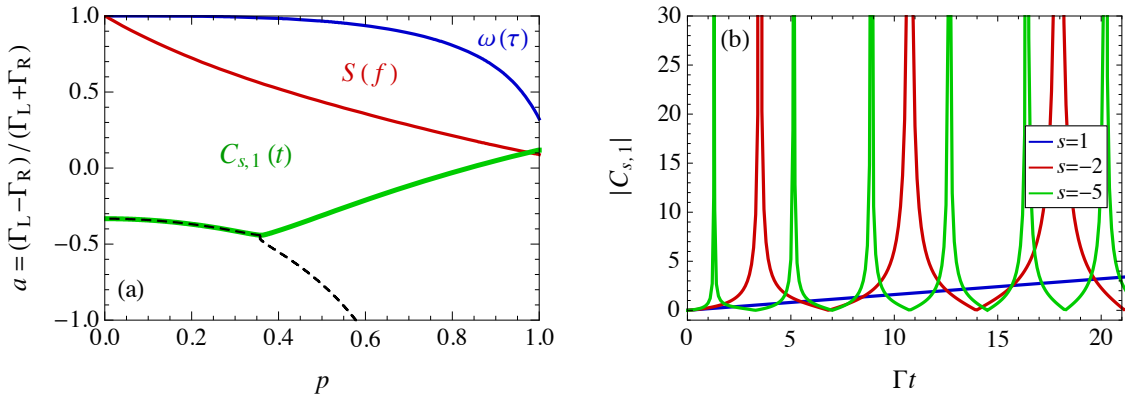

Figure 7.4: (a) Parameter space and (b) generalized factorial cumulants. Other parameters are as in Figure 7.2. For (b), $p = 3/10$ and $a = -8/10$. (a) Above the colored lines, coherent transport is detected by the respective quantity. Below the dashed line, peaks can be observed in $C_{s,1}(t)$ as illustrated in (b). Since their frequency is not s-independent, they are due to incoherent transport.

The capability of the waiting times $\omega(\tau)$, the finite-frequency noise $S(f)$, and the generalized factorial cumulants $C_{s,m}(t)$ to detect coherently transferred electrons is compared in Figure 7.4 (a) for different polarizations and asymmetries. Coherent transport is identified in the waiting times $\omega(\tau)$ if the amplitude of its Fourier transform $|\hat{\omega}(f)|$ shows one maximum at an $f \neq 0$. Similarly for the finite-frequency noise, a maximum at $f \neq 0$ indicates coherent transport at that frequency. The detection is possible via the waiting times for rather large polarizations and asymmetries above the blue line. The finite-frequency noise is more sensitive and detects coherent transport already above the red line. For small polarizations and asymmetries, both $\omega(\tau)$ and $S(f)$ do not indicate coherent transport anymore since the spin blockade becomes lifted, i.e., electrons leave the dot typically faster than f_{La}.

Coherently transferred electrons can be identified in the factorial cumulant $C_{s,m}$ as peaks. However, that does not imply that always peaks are due to coherences. We observe one class of peaks caused and one not caused by coherent transport.

For parameters above the green line, the peaks occur with an s-independent frequency for $s \ll -1$. It is the frequency presented in Eq. (7.15). The contributions of the higher orders in p can be formally expressed by the asymptotic expansion $\mathcal{O}\left(p^3\right) = \sum_{j=0}^{\infty} a_j(p)/\left|s\right|^j$, i.e., the s-dependence of f_{La} decays at least with $1/\left|s\right|$. These peaks represent the coherently transferred electrons and vanish if coherences are excluded manually ($B_{\mathrm{L}} = B_{\mathrm{R}} = 0$).

Below the dashed line, we observe peaks as illustrated in Figure 7.4 (b). They occur with the frequency

$$f = \frac{1}{2\pi}\sqrt{2\Gamma_{\mathrm{L}}\Gamma_{\mathrm{R}}\left|s\right|\left[1 + p^2\cos(\phi)\right]} + \mathcal{O}\left(\frac{1}{\sqrt{\left|s\right|}}\right), \tag{7.16}$$

independently if the coherences are excluded or not, cf. Appendix A.4.2. Such behavior is typical for Coulomb-blockade systems with two charge states and without coherences, cf. Chapter 4. In contrast to f_{La}, the frequency does not become s-independent for $s \ll -1$,

but grows with $\sqrt{|s|}$. If the parameter s is decreased in Figure 7.4 (b) from $s = -2$ to $s = -5$, the frequency increases and the number of observed peaks is doubled.

Thus, the presence of peaks in $C_{s,m}(t)$ with an s-independent frequency is a well defined indicator for the coherent transport. The detection succeeds in a much larger area of the parameter space than for the waiting times and finite-frequency current noise. Even for arbitrary small polarizations $p > 0$ and both vanishing or negative asymmetry, coherent transport can be identified.

7.4 Conclusions

In this chapter, we proposed a new method to detect coherently transferred electrons, also denoted by coherent oscillations, via generalized factorial cumulants. We discussed our method for the transport through a quantum-dot spin valve. Importantly, generic experimental detectors (single-electron transistor or quantum point contact) measuring the cumulants do not destroy the coherent oscillations in the spin-valve. Hence, our method can already be experimentally used for such systems.

The coherent oscillations are identified in the generalized factorial cumulants $C_{s,m}(t)$ as peaks occurring with an s-independent frequency as function of time t. Each peak is due to a single coherently transferred electron. The number of coherently transferred electrons in time t is therefore directly obtained by counting the number of occurred peaks.

Of crucial importance is the parameter s. For negative s, we get rid of an overwhelming number of incoherently transferred electrons and merely the remaining coherently transferred electrons determine the generalized factorial cumulants. Therefore, the sensitivity for coherent oscillations increases dramatically in comparison the commonly used quantities as the waiting times, finite-frequency noise, or ordinary (factorial) cumulants.

These common quantities detect the coherent oscillations for large spin polarizations p of the leads and large asymmetries between its tunnel coupling strengths Γ_r to the quantum dot. With generalized factorial cumulants, the detection succeeds already for leads fabricated out of Fe, Co, or Ni and small asymmetries. Even for arbitrary weak polarizations $p > 0$ and both vanishing $\Gamma_\mathrm{R} = \Gamma_\mathrm{L}$ or negative $\Gamma_\mathrm{R} > \Gamma_\mathrm{L}$ asymmetry, the coherent oscillations can still be detected.

Our detection method is especially convenient for spin valves experimental realized by a carbon-nanotube [126–130] or InAs-nanowire [125] dot. Ferromagnetic leads are typically made out of Ni or Pd alloys being ferromagnetic due to Ni impurities. Real-time charge counting has already been experimentally demonstrated both for the carbon-nanotube [35, 54] and InAs-nanowire [50–53] dot.

Finally, we want to note that our method does not only detect coherently transferred electrons, but also other kinds of electrons being transferred through a Coulomb-blockade system at some specific frequency.[3]

[3]The reason is the deterministic nature of electrons being transferred successively, cf. Section 3.4. Each electron transfer can be described by a probability $p_j(t)$ which is zero (finite) for times smaller (larger) than a certain time point.

8 Violation of detailed balance in Coulomb-blockade systems

In this chapter, we demonstrate how detailed balance can be violated in Coulomb-blockade systems. Detailed balance denotes the absence of net probability currents in the system's state space for the stationary limit. We explain that this violation is indicated by different charge-transfer statistics for tunneling in and out electrons.

The issue of detailed-balance violation has attracted much interest in the statistical-mechanics community [146, 147]. Stationary states that violate detailed balance are not fully characterized by the probability distribution alone since closed-loop probability currents occur. This has important implications for computer simulations of stochastic systems. Furthermore, the connection between closed-loop probability currents and entropy production has been investigated.

In Section 8.1, we discuss the necessary ingredients for a violation of detailed balance. By measuring the full counting statistics one acquires enough information to identify a violation of detailed balance as explained in Section 8.2. We discuss two example systems. In Section 8.3, we study the voltage-biased scenario of a quantum dot subjected to a Zeeman field and coupled to two metallic leads. In Section 8.4, we discuss the non-voltage biased scenario of a normal-state island coupled to one superconducting lead. We use factorial cumulants to detect a violation of detailed balance. Already low-order factorial cumulants are sufficient to identify the violation. Therefore, we do not apply generalized factorial cumulants in this chapter.

The results of this chapter have been published, in parts verbatim, in Ref. [148].

8.1 Detailed Balance

Charge transport through Coulomb-blockade systems can be simulated by a master equation (3.45). Starting at arbitrary initial probabilities $p^{\chi}(0)$, the system approaches a time independent limit. The corresponding stationary probabilities p^{χ}_{stat} are determined by

$$0 = \sum_{\chi'} [\Gamma_{\chi\chi'} p^{\chi'}_{\mathrm{stat}} - \Gamma_{\chi'\chi} p^{\chi}_{\mathrm{stat}}] \,. \tag{8.1}$$

The stationary state is said to obey detailed balance if not only the *sum* but *each summand* on the right-hand side of this equation vanishes,

$$\Gamma_{\chi\chi'} p^{\chi'}_{\mathrm{stat}} = \Gamma_{\chi'\chi} p^{\chi}_{\mathrm{stat}} \,, \tag{8.2}$$

for each pair χ, χ' [146, 147]. The combination $\Gamma_{\chi'\chi} p^{\chi}_{\mathrm{stat}}$ can be interpreted as the probability current from state χ to χ'. Detailed balance, then, means that the probability current

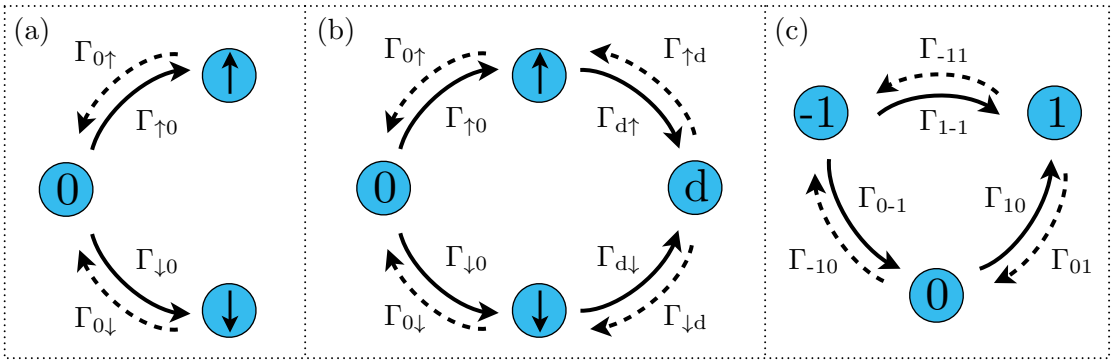

Figure 8.1: Three possible stochastic models realized in Coulomb-blockade systems. Solid (dashed) lines indicate transitions that are counted for the statistics of tunneling in (out). A violation of detailed balance, indicated by different counting statistics for tunneling in and tunneling out, is possible for model (b) and (c) but not for (a).

from χ to χ' minus the one from χ' to χ is zero, i.e., the net probability current

$$I_{\chi'\chi} = \Gamma_{\chi'\chi} p^{\chi}_{\mathrm{stat}} - \Gamma_{\chi\chi'} p^{\chi'}_{\mathrm{stat}} \tag{8.3}$$

is zero.[1]

To illustrate its implications, let us consider the following three Coulomb-blockade systems that will be discussed in more detail in the next sections.

In the first one, sketched in Figure 8.1 (a), some central region (e.g., quantum-dot or island) is empty $\chi = 0$ or occupied by an additional electron $\chi = \uparrow, \downarrow$. Transitions are allowed between 0 and $\uparrow$ as well as between 0 and $\downarrow$, but not directly between $\uparrow$ and $\downarrow$. Such a system has been studied in Chapter 4. In this case, the stationary state must obey detailed balance, as otherwise the net probability current $I_{\uparrow 0}$ or $I_{\downarrow 0}$ would be nonzero, which is incompatible with the steady-state condition.

Next, we extend the model by adding the fourth state of double occupancy $\chi = d$ with transition rates from and to the states $\uparrow$ and $\downarrow$, see Figure 8.1 (b). Depending on the values of the rates, this system can accommodate steady states that do not obey detailed balance. In such a state, there is a finite net probability current flowing around the loop $0 \to \uparrow \to \mathrm{d} \to \downarrow \to 0$ (or in the opposite direction $0 \to \downarrow \to \mathrm{d} \to \uparrow \to 0$).

Detailed-balance violating steady states are already possible for stochastic systems consisting of three states, but only if direct transitions between all the three charge states -1,

[1] We remark that, in the literature, the term 'detailed balance' is often defined in a different way: a stochastic system is said to obey detailed balance if the ratio $\Gamma_{\chi\chi'}/\Gamma_{\chi'\chi}$ of transition rates is given by $e^{-\beta(E_\chi - E_{\chi'})}$, where E_χ is the energy of state χ and β the inverse temperature. It, then, follows that the stationary (equilibrium) probability distribution is described by the Boltzmann factors, $p_\chi \sim e^{-\beta E_\chi}$ and Eq. (8.2) holds.

However, this alternative definition of detailed balance is not useful for systems for which the equilibrium probability distribution is *not* given by the Boltzman factors. This is, e.g., the case for the exactly-solvable model of a spinless single-level quantum dot coupled to one lead beyond the weak-coupling limit [91]. There, higher-order tunneling leads to quantum-fluctuation induced broadening such that $\Gamma_{10}/\Gamma_{01} \neq e^{-\beta(E_1 - E_0)}$ but Eq. (8.2) still holds. Another example is the single-electron box discussed in Section 8.4.

0, 1 (relative to some reference charge) are allowed, see Figure 8.1 (c), and the tunneling rates are chosen properly.

8.2 Detection of detailed-balance violation

In Coulomb-blockade devices, a detector measures the charge on some central region as function of time. In the recorded time trace, one can count each electron tunneling *in* (solid lines in Figure 8.1) to obtain the probability distribution $P_N^{\mathrm{in}}(t)$. Alternatively, one may decide to count only electrons tunneling *out* (dashed lines in Figure 8.1) to obtain the distribution $P_N^{\mathrm{out}}(t)$.

If a transition $\chi \to \chi'$ increases the counter of tunneled *out* electrons, the counter of tunneling *in* electrons does not increase. In contrast, the opposite transition $\chi' \to \chi$ increases the counter of tunneled *in* electrons, but not of tunneled *out* electrons.

In the case of detailed balance, the probability to find a given sequence of states, $\chi_1 \to \chi_2 \to \ldots \to \chi_k$, is the same as finding the opposite sequence, $\chi_k \to \ldots \to \chi_2 \to \chi_1$. Thus, the distributions $P_N^{\mathrm{in}}(t)$ and $P_N^{\mathrm{out}}(t)$ are identical.

Therefore, a difference between $P_N^{\mathrm{in}}(t)$ and $P_N^{\mathrm{out}}(t)$ signals the violation of detailed balance. However, the reverse statement is not necessarily true, e.g., a detailed-balance violation between different microscopic realizations of one charge state may be not revealed in the charge-counting statistics.

In the following two sections, we discuss the violation of detailed balance for two example systems. Instead of comparing the distributions $P_N^{\mathrm{in}}(t)$ and $P_N^{\mathrm{out}}(t)$ directly, we conveniently study the corresponding cumulants, i.e., scalars which are easier to illustrate. The cumulants characterize the form of the probability distribution, cf. Section 3.2. Hence, a difference in the probability distributions is equivalent to a difference in some of the cumulants. Since the variable N of the probability distribution is discrete, we study the factorial cumulants $C_{\mathrm{F},m}^{\mathrm{in}}(t)$ and $C_{\mathrm{F},m}^{\mathrm{out}}(t)$, cf. Section 3.3. For the studied example systems, it will be sufficient to study low-order factorial cumulants. Therefore, we do not apply generalized factorial cumulants. The cumulants are simulated accordingly to Section 3.6.

8.3 Single-level quantum dot with Zeeman field

The first system is an example for the stochastic model depicted in Figure 8.1 (b). The precise details of the underlying microscopic model are given in Section 4.1. We consider a single-level quantum dot subject to a magnetic field and weakly tunnel coupled to two leads $r = \mathrm{L}, \mathrm{R}$ with tunnel-coupling strength Γ_r, see Figure 8.2 (a). The Zeeman field Δ splits the orbital level ε into $\varepsilon_\uparrow = \varepsilon + \Delta/2$ and $\varepsilon_\downarrow = \varepsilon - \Delta/2$ for spin $\sigma = \uparrow, \downarrow$. The level ε may be tuned by a gate voltage. The charging energy for double occupancy is denoted by U. A bias voltage V is symmetrically applied to the two leads, described by the electrochemical potentials $\mu_{\mathrm{L}} = eV/2$ and $\mu_{\mathrm{R}} = -eV/2$ for the left and right lead, respectively. If the electrons entering the quantum dot are counted, the probability vector

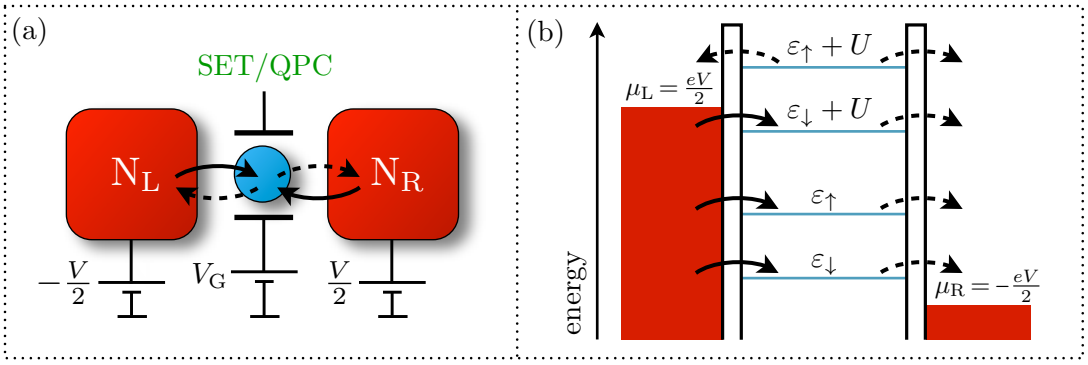

Figure 8.2: (a) Single-level quantum dot (blue) subjected to a Zeeman field and weakly tunnel coupled to two metallic leads (red). A bias voltage V is applied between the leads. The dot charge as function of time is monitored via a nearby single-electron transistor or quantum point contact (green). (b) Energy levels of the leads and the dot. For the depicted dot levels, detailed balance is violated. Since the transition $\downarrow \rightarrow$ d is not possible, a finite net probably current is flowing around the loop $0 \rightarrow \uparrow \rightarrow \mathrm{d} \rightarrow \downarrow \rightarrow 0$.

$\mathbf{p}_z = (p_z^0, p_z^\uparrow, p_z^\downarrow, p_z^\mathrm{d})^T$ is determined by the generator

$$\mathbf{W}_z^\mathrm{in} = \begin{pmatrix} -\Gamma_{\uparrow 0} - \Gamma_{\downarrow 0} & \Gamma_{0\uparrow} & \Gamma_{0\downarrow} & 0 \\ z\Gamma_{\uparrow 0} & -\Gamma_{0\uparrow} - \Gamma_{\mathrm{d}\uparrow} & 0 & \Gamma_{\uparrow \mathrm{d}} \\ z\Gamma_{\downarrow 0} & 0 & -\Gamma_{0\downarrow} - \Gamma_{\mathrm{d}\downarrow} & \Gamma_{\downarrow \mathrm{d}} \\ 0 & z\Gamma_{\mathrm{d}\uparrow} & z\Gamma_{\mathrm{d}\downarrow} & -\Gamma_{\uparrow \mathrm{d}} - \Gamma_{\downarrow \mathrm{d}} \end{pmatrix} . \tag{8.4}$$

If the electrons leaving the quantum dot are counted, the generator $\mathbf{W}_z^\mathrm{out}$ is obtained from Eq. (8.4) by removing the factors z from the lower-left off-diagonal matrix elements and attaching them, instead, to the upper-right elements. Fermi's golden rule yields for the tunneling rates

$$\Gamma_{\sigma 0} = \sum_{r=\mathrm{L,R}} \Gamma_r f_r(\varepsilon_\sigma) , \tag{8.5}$$

$$\Gamma_{0\sigma} = \sum_{r=\mathrm{L,R}} \Gamma_r [1 - f_r(\varepsilon_\sigma)] , \tag{8.6}$$

$$\Gamma_{\mathrm{d}\sigma} = \sum_{r=\mathrm{L,R}} \Gamma_r f_r(\varepsilon_{\bar\sigma} + U) , \tag{8.7}$$

$$\Gamma_{\sigma \mathrm{d}} = \sum_{r=\mathrm{L,R}} \Gamma_r [1 - f_r(\varepsilon_{\bar\sigma} + U)] , \tag{8.8}$$

with the Fermi function $f_r(x) = 1/\{\exp[(x - \mu_r)/k_\mathrm{B}T] + 1\}$ and $\bar\sigma$ is the spin opposite to σ.

In Figure 8.3 (a), the current as a function of level energy ε and bias voltage V is depicted. In the white region, the dot remains in its ground state due to Coulomb blockade. In the colored regions, transitions to other states become possible. In most areas of the parameter space, detailed balance holds. However, as depicted in Figure 8.3 (b), there are also areas where detailed balance is violated, which is indicated by a nonvanishing difference $C_{\mathrm{F},2}^\mathrm{in} - C_{\mathrm{F},2}^\mathrm{out}$.

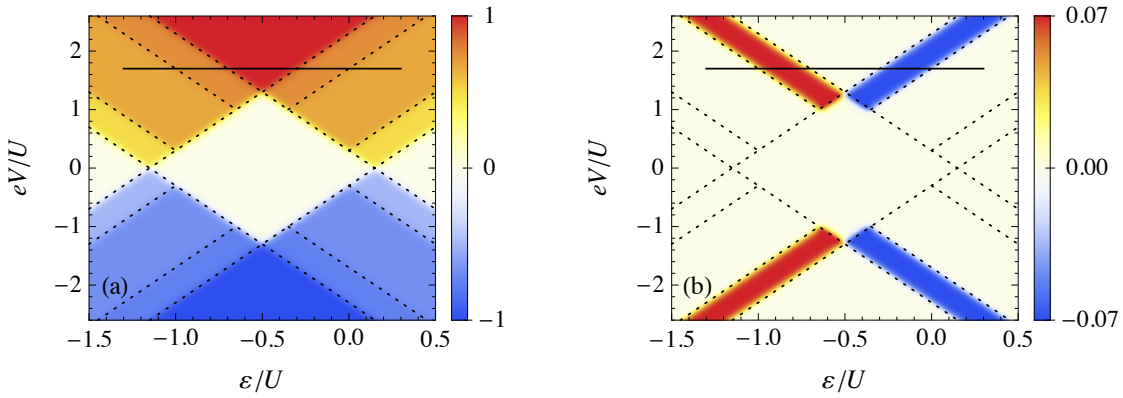

Figure 8.3: (a) Current in units of $e\Gamma_\mathrm{L}$ through the quantum-dot system depicted in Figure 8.2 (a). (b) The difference $C^{\mathrm{in}}_{\mathrm{F},2} - C^{\mathrm{out}}_{\mathrm{F},2}$ of the second factorial cumulant as function of the level energy ε and bias voltage V. The parameters are $\Delta = 0.3\,U$, $k_\mathrm{B}T = 0.02\,U$, $\Gamma_\mathrm{L} = \Gamma_\mathrm{R}$, and $t = 2/\Gamma_\mathrm{L}$. The solid line marks values for ε and V used in Figure 8.4. The dotted lines mark positions of the resonances of the quantum-dot excitation energies with the Fermi level of the source or drain electrode. A nonvanishing value of $C^{\mathrm{in}}_{\mathrm{F},2} - C^{\mathrm{out}}_{\mathrm{F},2}$ in (b) indicates the violation of detailed balance.

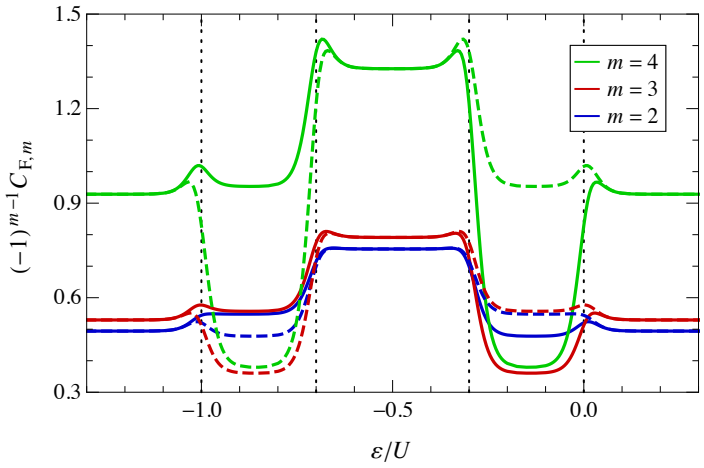

Figure 8.4: Factorial cumulants of tunneling in $C^{\mathrm{in}}_{\mathrm{F},m}$ (solid lines) and tunneling out events $C^{\mathrm{out}}_{\mathrm{F},m}$ (dashed lines). The parameters are the same as in Figure 8.3 with $eV = 1.7\,U$. The dotted vertical lines indicate the positions of the resonances of the quantum-dot excitation energies with the the Fermi level of the source or drain electrode.

In Figure 8.4, we depict the factorial cumulants $C^{\mathrm{in}}_{\mathrm{F},m}(t)$ (solid lines) and $C^{\mathrm{out}}_{\mathrm{F},m}(t)$ (dashed lines) as a function of the orbital level energy ε for a given bias voltage indicated by the black line in Figure 8.3. For $0 < \varepsilon/U$, double occupation of the quantum dot is suppressed such that the device is a realization of the stochastic model shown in Figure 8.1 (a), for which detailed balance is expected to be fulfilled. Thus, the factorial cumulants are the same for the tunneling-in and tunneling-out statistics.

This is qualitatively different for $-0.3 < \varepsilon/U < 0$. All transitions depicted in Figure 8.1 (b) are possible, except the transition from $\downarrow$ to d as illustrated in Figure 8.2 (b), i.e., $\Gamma_{\mathrm{d}\downarrow} = 0$. Since both the probabilities $p_\downarrow$ and p_d are finite, detailed balance Eq. (8.2) is violated. We find a clear difference between the factorial cumulants of the tunneling-in and the tunneling-out statistics for all cumulants of order $m \geq 2$, see Figure 8.4. Of course, the first cumulants of tunneling in and tunneling out are identical, which is a consequence of the system being in a steady state (note that the first cumulant is equal to the mean number $\langle N \rangle$).

For $-0.7 < \varepsilon/U < -0.3$, also the transition $\downarrow$ to d becomes possible and detailed balance is reestablished. Factorial cumulants are the same for the tunneling-in and tunneling-out statistics. For even smaller level positions ε, the upper discussion can be repeated due to particle hole symmetry.

We remark that in order to violate detailed balance, it was crucial to break the symmetry between spin $\uparrow$ and $\downarrow$ as well as the symmetry between 0 and d. Without a Zeeman field $\Delta = 0$ or Coulomb interaction $U = 0$, detailed balance is recovered. Only with a finite Zeeman field and Coulomb interaction, there are the regions in parameter space, as depicted in Figure 8.3 (b), where detailed balance is violated.

Furthermore, we emphasize that for the proposed quantum-dot system, a finite bias voltage was applied to achieve a violation of detailed balance, because, otherwise, we could not overcome the charging energy to occupy three different charge states with a finite probability. There is, however, no fundamental reason to require a bias voltage for breaking detailed balance. In fact, in the next section, we are going to show an example that already works without bias voltage.

8.4 Sequential and Andreev tunneling in a single-electron box

The second system is an example for the stochastic model depicted in Figure 8.1 (c). Its set-up has been introduced in Section 5.3 and depicted in Figure 5.2 (a). If electrons are counted tunneling into the normal-metal island, the generator takes the form

$$\mathbf{W}_z^{\mathrm{in}} = \begin{pmatrix} -\Gamma_\mathrm{A}^+ - \Gamma_\mathrm{d}^+ & \Gamma_\mathrm{u}^- & \Gamma_\mathrm{A}^- \\ z\Gamma_\mathrm{d}^+ & -\Gamma_\mathrm{u}^+ - \Gamma_\mathrm{u}^- & \Gamma_\mathrm{d}^- \\ z^2\Gamma_\mathrm{A}^+ & z\Gamma_\mathrm{u}^+ & -\Gamma_\mathrm{A}^- - \Gamma_\mathrm{d}^- \end{pmatrix} . \tag{8.9}$$

Since an Andreev-tunneling process transfers two electrons, Γ_A^+ is multiplied with the square z^2 instead of a single z. The matrix $\mathbf{W}_z^{\mathrm{out}}$ is given in Eq. (6.11).

The tunneling rates depend on the (normal-state) tunnel resistance, the energies of the different charge states and the coupling to the electromagnetic environment [31, 99]. In order to make close contact to possible experimental realizations, we do not calculate the tunneling rates for some assumed electromagnetic environment, but rather use experimentally measured values taken from Fig. 3b of Ref. [32]. We do this for two different choices of the gate voltage.

First, we consider the symmetric case, $n_\mathrm{G} = 0$, for which the charge states -1 and 1 are energetically degenerate. The transition rates are $\Gamma_\mathrm{d}^+ = \Gamma_\mathrm{d}^- = 960\,\mathrm{Hz}$, $\Gamma_\mathrm{u}^+ = \Gamma_\mathrm{u}^- = 9.4\,\mathrm{Hz}$, and $\Gamma_\mathrm{A}^+ = \Gamma_\mathrm{A}^- = 150\,\mathrm{Hz}$. The symmetry guarantees detailed balance, as demonstrated

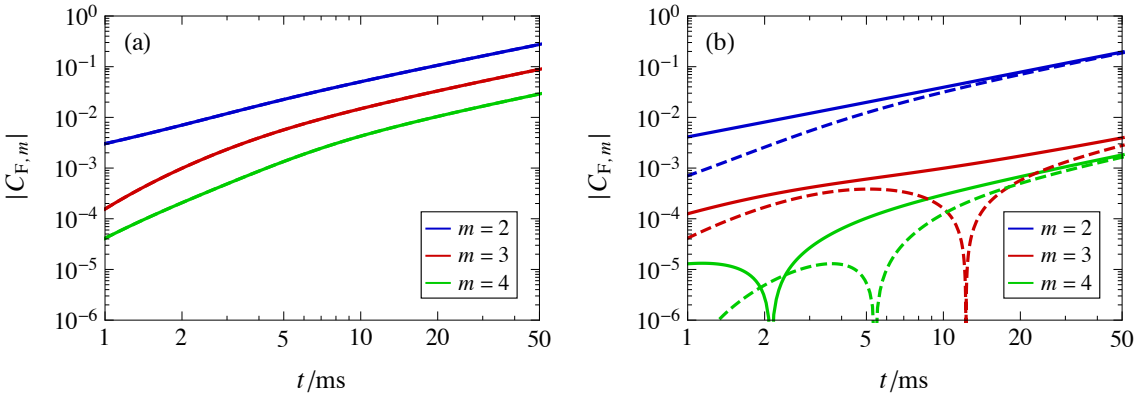

Figure 8.5: Factorial cumulants for the single-electron-box system depicted in Figure 5.2. Solid lines show $C^{\mathrm{in}}_{\mathrm{F},m}$ of tunneling-in events and dashed lines represent $C^{\mathrm{out}}_{\mathrm{F},m}$ of tunneling-out events. In (a), the gate charge is chosen $n_{\mathrm{G}} = 0$ such that the charge states -1 and 1 are degenerate. Detailed balance is fulfilled and thus solid and dashed lines coincide, $C^{\mathrm{in}}_{\mathrm{F},m} = C^{\mathrm{out}}_{\mathrm{F},m}$. In (b), we chose $n_{\mathrm{G}} = 0.12$. Violation of detailed balance is indicated by $C^{\mathrm{in}}_{\mathrm{F},m} \neq C^{\mathrm{out}}_{\mathrm{F},m}$.

in Figure 8.5 (a). This contrasts with the asymmetric case, for which we choose $n_{\mathrm{G}} = 0.12$. The transition rates are $\Gamma^{+}_{\mathrm{d}} = 1280\,\mathrm{Hz}$, $\Gamma^{-}_{\mathrm{d}} = 650\,\mathrm{Hz}$, $\Gamma^{+}_{\mathrm{u}} = 11.5\,\mathrm{Hz}$, $\Gamma^{-}_{\mathrm{u}} = 6.5\,\mathrm{Hz}$, $\Gamma^{+}_{\mathrm{A}} = 630\,\mathrm{Hz}$, and $\Gamma^{-}_{\mathrm{A}} = 10.8\,\mathrm{Hz}$. In this case, the factorial cumulants of order $m \geq 2$ for tunneling in and tunneling out differ from each other, see Figure 8.5 (b). The dips shown in Figure 8.5 (b) indicate sign changes of $C^{\mathrm{in}}_{\mathrm{F},m}$ and $C^{\mathrm{out}}_{\mathrm{F},m}$. They occur independently of each other. At long times, e.g. $t = 50\,\mathrm{ms}$, the signs of $C^{\mathrm{in}}_{\mathrm{F},m}$ and $C^{\mathrm{out}}_{\mathrm{F},m}$ coincide.

We emphasize that, for this device, Andreev tunneling is crucial to establish steady states that violate detailed balance. Without this charge-transfer channel, there would be no possibility for a finite net probability current around a closed loop.

8.5 Conclusions

Time-resolved measurements of electron tunneling into and out of a quantum dot or a single-electron box in the steady-state limit define a suitable tool to test whether or not detailed balance is fulfilled. To generate a steady state that violates detailed balance, one needs to realize a stochastic model with at least three different states and tunneling rates that allow for a finite net probability current around a closed loop. We have suggested two devices in which such detailed-balance-violating steady states can be established: a spin-split, single-level quantum dot at large bias voltage and a metallic single-electron box coupled to a superconductor. Both suggestions seem experimentally feasible with nowadays technology. Moreover, for some of the performed counting experiments referred to in Section 2.3, the collected data may already be sufficient to prove the violation of detailed balance.

9 Conclusions

In this thesis, we have introduced generalized factorial cumulants as a new tool to probe the full counting statistics of electron transport through Coulomb-blockade systems.

Recent progress in nanotechnology, as summarized briefly in Chapter 2, has led to the development of electrometers with a resolution that could not be attained before: transport of individual electrons can be observed in real time. The electrometer inspects the total charge on some mesoscopic region of the studied device. It detects charge changes on the scale of single electrons and thereby resolves the transport of individual electrons.

To reach such a sensitivity, the probed system must fulfill some requirements. First, only a small number of electrons can leave or enter in comparison to some reference charge on the inspected region. Due to the Coulomb interaction, most charge states are not accessible and transport via theses states is blocked out. Second, the electrons stay on the region at least for times on the millisecond scale, i.e., the resistance is larger than the inverse of one conductance quantum $h/e^2 \approx 26\,\mathrm{k}\Omega$. Therefore, the region is only weakly tunnel coupled to the rest of the system. An additional consequence is that the electron transport can be simulated by an *N-resolved master equation* taking only tunneling processes of leading order in the tunnel-coupling strength into account. We have referred to such a system as *Coulomb-blockade system*. Two fundamental examples of Coulomb-blockade systems are the single-electron box (SEB) and the single-electron transistor (SET).

In this thesis, we have aimed at results that can be used already with the current level of technology. We have presented results valid for any kind of Coulomb-blockade system, but have also illustrated these results for concrete examples like the transport through single metallic islands and quantum dots tunnel coupled to superconducting, ferromagnetic, or normal metallic electrodes. For all these example systems, it has been demonstrated already in experiments that electron transport can be observed in real time. Thus, our results can be applied immediately to such experimental realizations of a Coulomb-blockade system.

From the real-time measurement, one obtains the full counting statistics of electron transport. The statistics is characterized by the probability distribution $P_N(t)$ that N electrons have been transferred in a time interval $[0,t]$. Instead of dealing with all information contained in $P_N(t)$ simultaneously, one typically analyses cumulants calculated from $P_N(t)$. These scalars accumulate information from $P_N(t)$ into one meaningful statement which should lead to a better understanding of the electron transport. In literature, ordinary cumulants $C_m(t)$ and factorial cumulants $C_{\mathrm{F},m}(t)$ of order m are already known. In Chapter 3, we have introduced *generalized factorial cumulants* $C_{s,m}(t)$ as a much more convenient tool to study the electron transport. For $s=1$, the cumulants $C_{1,m}(t)$ are equal to the factorial cumulants $C_{\mathrm{F},m}(t)$. The first factorial cumulant $C_{1,1}(t)$ yields the current and the second $C_{1,2}(t)$ the current noise. By tuning the parameter s, different electron transfer process can be probed, including those hidden for the factorial cumulants $C_{\mathrm{F},m}(t)$. In Chapters 3 - 8, we have elucidated what kind of conclusions can be drawn from the $C_{s,m}(t)$ leading to a

better understanding of the electron transport. We have observed that other quantities accumulate relevant information from $P_N(t)$ in a less effective manner than the $C_{s,m}(t)$ or are even completely insensitive to the relevant information.

In Chapter 3, we have explained how *correlations* can be detected by the generalized factorial cumulants $C_{s,m}(t)$. First, we have studied uncorrelated electron transport, i.e., the probability distribution is determined by independent single-electron tunneling events and therefore takes the form of a Poisson binomial distribution. We have proven that for $s \geq 0$ the generalized factorial cumulants fulfill the sign criterion $(-1)^{m-1}C_{s,m}(t) \geq 0$. For $s < 0$, the sign criterion still holds for all even orders m. Thus, a violation of this criterion for any time t, order m, or real s indicates correlations, i.e., at least one subprocess contributes to transport, but can not be decomposed into single-electron tunneling events.

In Chapter 4, we have tested this criterion for two example systems. We have simulated a counting experiment for a SEB in a Zeeman-field (see experiments in Section 2.2) and a SET with ferromagnetic leads [124]. In these examples, correlations are induced by the Coulomb interaction. We have found that with decreasing s the generalized factorial cumulants $C_{s,m}(t)$ detect the correlations at lower order m and at earlier time t than the factorial cumulants $C_{\mathrm{F},m}(t)$. This may be crucial to overcome experimental limitations since the error of experimentally determined cumulants typically increases both with m and t [19, 20]. Furthermore, since the $C_{s,m}(t)$ have access to additional processes, we have observed parameter regimes in which only the generalized factorial cumulants can detect correlations while all the $C_{\mathrm{F},m}(t)$, including the current noise, fail.

In Chapter 5, we have concentrated on the detection of correlations for Coulomb-blockade systems in the limit of time intervals $[0, t]$ being short in comparison to the average waiting time between two successive tunneling events. In addition to the sign criterion given in Chapter 3, the presence of correlations is proven by a different sign for odd m and $s < 0$, any s-dependence itself, or a time dependence different from $C_{s,m}(t) \propto t^m$. Moreover, we derived the necessary ingredients for the presence of correlations. If each tunneling process transfers only a single electron, at least three charge states must be accessible. If tunneling processes can transfer multiple electrons, electron transport is always correlated. Furthermore, we have deduced universal formulas for the $C_{s,m}(t)$ in the short-time limit. Thereby, we could explain the power-law dependence t^m observed in a recent experiment [19]. Moreover, we have simulated the counting experiment recently performed for a SEB subjected to Andreev tunneling [5]. Already the s-dependence of $C_{s,1}(t)$ indicates the presence of correlations. Additionally, for the higher-order cumulants, we observed the characteristic power law $t^{\frac{m}{2}}$ for even and $t^{\frac{m+1}{2}}$ for odd orders m, which also indicates correlations.

In Chapter 6, we have suggested to use experimental measured $C_{s,m}(t)$ to reconstruct characteristic features of an a priori unknown stochastic system which is determined by an N-resolved master equation. A precise manual of the mathematical procedure referred to as *inverse counting statistics* is given in Section 6.6. The input information of the procedure is $C_{s,m}(t)/t$ at such a long time t that $C_{s,m}(t)/t$ is time independent. The output information is as follows. First, it yields a lower bound for the dimension M of the stochastic system. Second, it gives a lower bound for the counting power D characterizing the coupling between the stochastic system and the detector. Third, it yields the characteristic function $\chi(z, \lambda)$ of the generator $\mathbf{W}_z$ of the N-resolved master equation. Each zero of the characteristic function is an eigenvalue $\lambda_j(z)$ of $\mathbf{W}_z$. We obtain the full spectrum of eigenvalues including the full spectrum of relaxation rates $\{\lambda_j(1)\}$ which have been recently

studied extensively [67–72]. In contrast to other experimental methods [111–115], the inverse counting statistics yields *all* rates and not *some* due to a certain initial perturbation of the system. The parameter s of the $C_{s,m}(t)$ is used to sensitively test for the lower bounds of M and D. Furthermore, it can be crucial to obtain the full spectrum of eigenvalues. We have demonstrated the procedure for two example systems. We have simulated a counting experiment for a SEB in a Zeeman-field (see experiments in Section 2.2) and a SEB subjected to Andreev tunneling [5, 32].

In Chapter 7, we have used the $C_{s,m}(t)$ to detect coherently transferred electrons in the transport through a quantum-dot spin valve, also denoted by *coherent oscillations*. These electrons are identified in the $C_{s,m}(t)$ with negative s as peaks occurring with a specific frequency in time t, the Larmor frequency of a virtual magnetic field. By counting the number of peaks, the number of coherently transferred electrons is obtained. Of crucial importance is the parameter s. For negative s, one gets rid of an arbitrary large number of incoherently transferred electrons and only the remaining coherently transferred electrons determine the generalized factorial cumulants. Therefore, the sensitivity for coherent oscillations increases dramatically in comparison to the commonly used quantities as the waiting times, finite-frequency noise, or ordinary (factorial) cumulants. The increased sensitivity is especially convenient to discover the coherent oscillations in the existing experimental set-ups [124–130] in combination with the real-time measurement techniques demonstrated in Refs. [35, 50–54]. We remark that our method does not only detect the coherently transferred electrons in the transport through a quantum-dot spin valve, but also other kinds of electrons being transferred through a Coulomb-blockade system at some specific frequency.

Finally, in Chapter 8, we have explained how *detailed balance* can be violated in Coulomb-blockade systems and how the violation can be detected. Detailed balance means the absence of net probability currents in the system's state space for the stationary limit. It can be violated if the state space consist of more than two states connected by tunneling rates in such a way that a closed loop forms. Real-time measurements of electron transfer resolve different parts of the net probability current, i.e., those partial currents corresponding to the tunneling in and those corresponding to tunneling out electrons. A difference in the tunneling in and out statistics indicates that a net probability current flows, i.e., detailed balance is violated. The difference in the statistics can be identified conveniently in the generalized factorial cumulants. We have illustrated our findings by simulating the counting experiment of a SET in a Zeeman-field (see experiments in Section 2.2) and a SEB subjected to Andreev tunneling [32]. In this Chapter, it has not been necessary to study parameters different from $s = 1$ because already the factorial cumulants indicate the violation of detailed balance.

A Appendix

A.1 Factorization of the generating function

In the following, we give a short derivation of Eq. (3.7)

$$\mathcal{M}(z,t) = \prod_j \mathcal{M}(z,t,j)\,, \tag{A.1}$$

where $\mathcal{M}(z,t,j) = \sum_N e^{Nz} P_N(t,j)$ is the generating function of a subprocess j. We start with a probability distribution which separates into two independent subprocesses

$$P_N(t) = \sum_{N_1=0}^{N} P_{N_1}(t,1) P_{N-N_1}(t,2)\,. \tag{A.2}$$

The moment-generating function takes the form

$$\mathcal{M}(z,t) = \sum_{N=0}^{\infty} \sum_{N_1=0}^{N} e^{N_1 z} P_{N_1}(t,1)\, e^{(N-N_1)z} P_{N-N_1}(t,2)\,. \tag{A.3}$$

Since the probability distribution $P_{N-N_1}(t,2) = 0$ for $N_1 > N$, we can extend the summation over N_1 to ∞

$$\mathcal{M}(z,t) = \sum_{N_1=0}^{\infty} e^{N_1 z} P_{N_1}(t,1) \sum_{N=0}^{\infty} e^{(N-N_1)z} P_{N-N_1}(t,2)\,. \tag{A.4}$$

Again, we use $P_{N-N_1}(t,2) = 0$ for $N_1 > N$ to start the summation over N not at $N = 0$, but at $N = N_1$. An index shift of N yields finally

$$\mathcal{M}(z,t) = \sum_{N_1=0}^{\infty} e^{N_1 z} P_{N_1}(t,1) \sum_{N_2=0}^{\infty} e^{N_2 z} P_{N_2}(t,2) = \mathcal{M}(z,t,1)\mathcal{M}(z,t,2)\,. \tag{A.5}$$

The extension to more subprocesses is straight forward.

A.2 Additional details concerning the transport through a quantum dot

In this section, we present some mathematical details which have not been presented in Chapter 4 or Ref. [63].

A.2.1 Two-state system

The generalized factorial cumulants discussed in Chapter 4 are obtained from the master equation (4.6). However, in the two special cases[1]

$$\Gamma_{0\uparrow} = \Gamma_{0\downarrow}\,, \tag{A.6}$$

$$\Gamma_{0\uparrow} = \frac{\Gamma_{0\downarrow}\Gamma_{\downarrow 0}}{\Gamma_{0\downarrow} - \Gamma_{\uparrow 0}}\,, \tag{A.7}$$

the same moment-generating function can, alternatively, be obtained from the master equation

$$\begin{aligned} \dot{p}^0_N(t) &= -\Gamma_{10} p^0_N(t) + \Gamma_{01} p^1_{N-1}(t), \\ \dot{p}^1_N(t) &= \Gamma_{10} p^0_N(t) - \Gamma_{01} p^1_N(t), \end{aligned} \tag{A.8}$$

describing transitions between the two states $\chi = 0, 1$. The probability vector $\mathbf{p}_z = (p^0_z, p^1_z)$ is determined by the matrix

$$\mathbf{W}_z = \begin{pmatrix} -\Gamma_{10} & z\Gamma_{01} \\ \Gamma_{10} & -\Gamma_{01} \end{pmatrix}. \tag{A.9}$$

In the first case $\Gamma_{\uparrow 0} = \Gamma_{\downarrow 0}$, the effective rates must be

$$\Gamma_{10} := \Gamma_{\uparrow 0} + \Gamma_{\downarrow 0}\,, \quad \Gamma_{01} := \Gamma_{0\downarrow}\,. \tag{A.10}$$

In the second case $\Gamma_{0\uparrow} = \Gamma_{0\downarrow}\Gamma_{\downarrow 0}/(\Gamma_{0\downarrow} - \Gamma_{\uparrow 0})$, the rates take the form

$$\Gamma_{10} := \Gamma_{0\uparrow}\,, \quad \Gamma_{01} := \Gamma_{0\downarrow}\,. \tag{A.11}$$

The two-state master equation describes the filling and depleting of a single spinless quantum-dot level. Double occupation is forbidden by the Pauli exclusion principle. Thus, the Coulomb interaction, being the source of correlations between the tunneling events, can be neglected. The counted electrons tunnel in an uncorrelated manner, see Chapter 3.4, and all zeros $z_j(t)$ of the factorial moment-generating function lie in the interval $(-\infty, -1]$ as illustrated in the following.

Taking Eq. (3.53) into account, the factorial moment-generating function can be written in the form

$$\begin{aligned} &\mathcal{M}_{\mathrm{F}}(z,t) = c_1(z) e^{\lambda_1(z)t}(z) + c_2(z) e^{\lambda_2(z)t}, \\ &\lambda_{1,2} = \frac{1}{2}\left(-\Gamma \pm \sqrt{\Gamma^2 + 4z\Gamma_{10}\Gamma_{01}}\right), \quad c_{1,2} = \pm \frac{\left(\Gamma \pm \sqrt{\Gamma^2 + 4z\Gamma_{10}\Gamma_{01}}\right)^2}{4\Gamma\sqrt{\Gamma^2 + 4z\Gamma_{10}\Gamma_{01}}}, \quad \Gamma = \Gamma_{10} + \Gamma_{01}. \end{aligned} \tag{A.12}$$

If $z > -\Gamma^2/(4\Gamma_{10}\Gamma_{01})$, the eigenvalues $\lambda_{1,2}(z)$ and coefficients $c_{1,2}(z)$ are real and the generating function is always positive. For $z < -\Gamma^2/(4\Gamma_{10}\Gamma_{01})$, the eigenvalues and coefficients have imaginary contributions which lead to oscillations around zero, see Figure A.1 (a).

[1] As discussed in Section 6.4, one of the three eigenvalues $\lambda_j(z)$ becomes z-independent for such special rates of the quantum-dot system. Thus, an ansatz for these rates is, e.g., obtained by equalizing the eigenvalue spectrum of $\mathbf{W}_z$ at $z = 1$ with the eigenvalue given in Eq. (A.22) for $z \to -\infty$. The correctness of the ansatz is proven by inspecting the resulting moment-generating function.

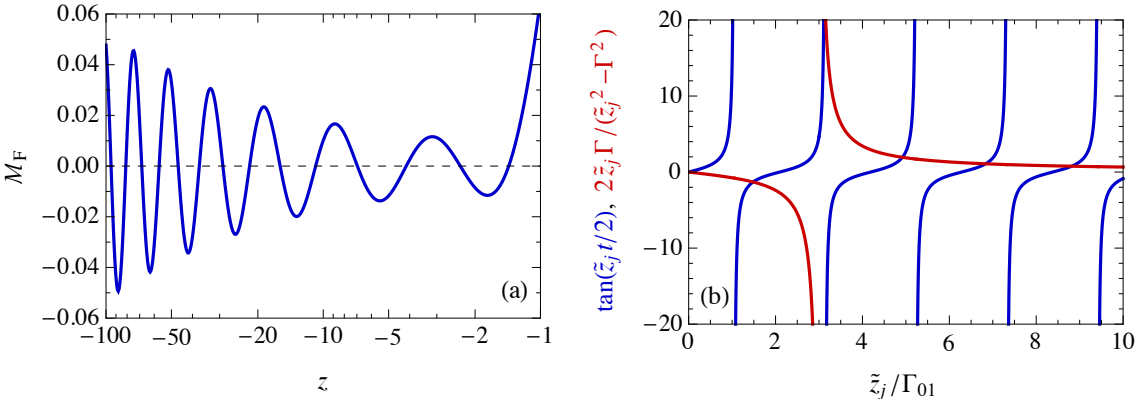

Figure A.1: The factorial moment-generating function for a single spinless quantum-dot level (a) with the rate $\Gamma_{10} = 2\Gamma_{01}$, time $t = 3/\Gamma_{01}$, and negative real z. The positions of the corresponding zeros z_j are given by the intersections of the two functions depicted in (b).

All possible zeros $z_j(t)$ lie on the negative real axis and are due to these oscillations. Since $-\Gamma^2/(4\Gamma_{10}\Gamma_{01})$ is always smaller than -1, the zeros are indeed confined to the interval $(-\infty, -1]$. The zeros z_j can be expressed by the transcendental equation

$$\tan\left(\frac{\tilde{z}_j t}{2}\right) = \frac{2\tilde{z}_j\Gamma}{\tilde{z}_j{}^2 - \Gamma^2}, \quad z_j = -\frac{\Gamma^2}{4\Gamma_{10}\Gamma_{01}} - \frac{\tilde{z}_j{}^2}{4\Gamma_{10}\Gamma_{01}} \tag{A.13}$$

depicted in Figure A.1 (b). In the short-time limit, the equation can be simplified by expanding the branches of the tangent up to first order

$$-j\pi + \frac{\tilde{z}_j t}{2} = -\frac{2\tilde{z}_j\Gamma}{\tilde{z}_j{}^2 - \Gamma^2}, \quad z_j = -\frac{\Gamma^2}{4\Gamma_{10}\Gamma_{01}} - \frac{\tilde{z}_j{}^2}{4\Gamma_{10}\Gamma_{01}}\,. \tag{A.14}$$

Taking only the leading orders in $1/t$ into account, we obtain

$$z_j(t) \approx \begin{cases} -\frac{\Gamma}{\Gamma_{10}\Gamma_{01}t}, & j = 0 \\ -\frac{(j\pi)^2}{\Gamma_{10}\Gamma_{01}t^2}, & j = 1, 2, \ldots \end{cases}. \tag{A.15}$$

With increasing time, the branches of the tangent move closer to the origin $\tilde{z}_j = 0$. Hence, the dominant zeros can approximated by expanding Eq. (A.13) up to linear order in $\tilde{z}_j$

$$-(j+1)\pi + \frac{\tilde{z}_j t}{2} = -\frac{2\tilde{z}_j}{\Gamma}, \quad z_j = -\frac{\Gamma^2}{4\Gamma_{10}\Gamma_{01}} - \frac{\tilde{z}_j{}^2}{4\Gamma_{10}\Gamma_{01}}\,, \tag{A.16}$$

which leads to

$$z_j(t) \approx -\frac{\Gamma^2}{4\Gamma_{10}\Gamma_{01}} - \frac{\big(\{j+1\}\pi\Gamma\big)^2}{\Gamma_{10}\Gamma_{01}(4+\Gamma t)^2}, \quad j = 0, 1, 2\ldots\,. \tag{A.17}$$

With increasing time, the approximation holds up to an increasing number j. However, even if the linear approximation is not justified, the absolute deviation from Eq. (A.17) is merely of first order in j.

A.2.2 (Un)correlated parameter regimes

If the rates $\Gamma_{\sigma 0}$ and $\Gamma_{0\sigma}$ do not obey Eq. (A.6) or (A.7), electrons can tunnel in a correlated manner, i.e., zeros $z_j(t)$ leave the interval $(-\infty, -1]$. In this section, we sketch the mathematical procedure how parameter regimes can be identified, each yielding a topologically different arrangement of zeros $z_j(t)$ in the complex plane. Especially, we comment on the derivation of the boundary conditions between the different regimes given in Eqs. (4.10), (4.13), and (4.14).

Again, we start with the generating function, see Eq. (3.53), written in the form

$$\mathcal{M}_{\mathrm{F}}(z,t) = c_1(z)e^{\lambda_1(z)t} + c_2(z)e^{\lambda_2(z)t} + c_3(z)e^{\lambda_3(z)t}\,. \tag{A.18}$$

We still obtain closed-form expressions for the coefficients and eigenvalues. However, the expressions are too large to explicitly write them down here. In the limit $|z| \gg 1$, the eigenvalues $\lambda_{1,2}(z)$ and coefficients $c_{1,2}(z)$ acquire forms similar to Eq. (A.12), especially $\mathrm{Re}[\lambda_{1,2}(z)]$ becomes z-independent and $c_{1,2}(z) \propto \sqrt{z}$. In contrast, the term $c_3(z)e^{\lambda_3(z)t}$ with real $\lambda_3(z)$ and $c_3(z)$ can be neglected for $|z| \gg 1$ since both $\lambda_3(z)$ and $c_3(z)$ become z-independent. In the short-time limit, the zeros of the generating function fulfill $|z_j(t)| \gg 1$. Thus, in accordance to Appendix A.2.1, the zeros remain on the real axis for short times. However, with increasing time, the exponential term $c_3(z)e^{\lambda_3(z)t}(z)$ can become relevant. If the real $\lambda_3(z)$ is larger than the real part of $\lambda_{1,2}(z)$, zeros are shifted away from the negative real axis into the complex plane.

In this sense, an eigenvalue discussion can reveal different arrangements of zeros in the complex plane and the corresponding necessary parameters. As an example, we illustrate in the following how such a discussion reveals the three arrangements depicted in Figure 4.8.

For the parameter regime illustrated in Figure A.2 (a), the value $\lambda_3(z)$ is smaller than $\mathrm{Re}[\lambda_{1,2}(z)]$. The oscillating term $c_1(z)e^{\lambda_1(z)t} + c_2(z)e^{\lambda_2(z)t}$ dominates the generating function also for finite times. The zeros remain on the real axis as depicted in Figure 4.8 (a). To see that the zeros are always smaller than -1, we take into account that with increasing time the zeros move towards square-root branch points [64, Section 5] of the two larges eigenvalues. For the studied system, square-root branch points on the real axis are always smaller than -1. Thus, we see that for the parameter regime illustrated in Figure A.2 (a), the zeros are indeed confined to the interval $(-\infty, -1]$.

In the second parameter regime illustrated in Figure A.2 (b), the value $\lambda_3(z)$ is smaller than $\mathrm{Re}[\lambda_{1,2}(z)]$ only near $z = -1$. In contrast, for $z \ll -1$, $\lambda_3(z)$ is the largest eigenvalue. Thus, the zeros remain real in the former case, but leave the real axis in the latter case, see Figure 4.8 (b). The boundary condition between the regimes (a) and (b) is given by

$$\lim_{z\to-\infty} \lambda_3(z) = \lim_{z\to-\infty} \mathrm{Re}[\lambda_{1,2}(z)]\,. \tag{A.19}$$

To obtain the correct limits, we apply the ansatz

$$\lambda(z) = a_{-1}\sqrt{z} + \sum_{j=0}^{\infty} a_j \frac{1}{z^{j/2}}\ . \tag{A.20}$$

If the ansatz is correct, the characteristic polynomial of $\mathbf{W}_z$, see Eq. (4.7), vanishes in every order in z. The highest order $z^{3/2}$ depends only on the coefficient a_{-1} and thus

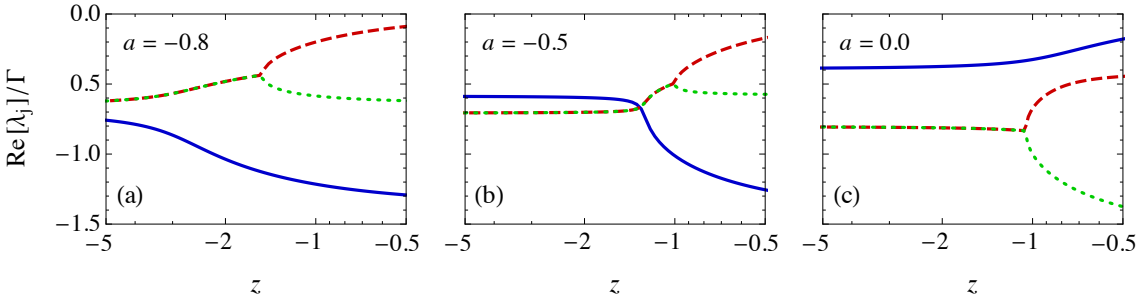

Figure A.2: Real part of the eigenvalues of $\mathbf{W}_z$ for a single-level quantum dot with ferromagnetic leads. The parameters are the same as in Figure 4.8 with $\Gamma = \Gamma_\mathrm{L} + \Gamma_\mathrm{R}$. For $a = -0.8$, the eigenvalues $\lambda_{1,2}$ (dashed and dotted line) are larger than λ_3 (solid line). For $a = 0.0$, the situation is reversed. For $a = -0.5$, λ_3 is the largest eigenvalue for $z \lesssim -1.3$, otherwise $\lambda_\pm$.

completely determines the first term of the eigenvalues $\lambda_j(z)$. The order $z^{2/2}$ depends on the coefficients a_{-1} and a_0, i.e., we obtain the second term of $\lambda_j(z)$. Each additional order becomes vanishing if an additional coefficient a_j is chosen properly. Thus, the ansatz has been correct. The eigenvalues take the form

$$\lambda_{1,2}(z) = \pm\sqrt{z\textstyle\sum_\sigma \Gamma_{0\sigma}\Gamma_{\sigma 0}} - \frac{\sum_\sigma \Gamma_{0\sigma}\Gamma_{\sigma 0}(\Gamma_{0\sigma}+\Gamma_{\sigma 0}+\Gamma_{\bar\sigma 0})}{2\sum_\sigma \Gamma_{0\sigma}\Gamma_{\sigma 0}} + \mathcal{O}\left(\frac{1}{\sqrt{z}}\right), \tag{A.21}$$

$$\lambda_3(z) = -\frac{\Gamma_{0\uparrow}\Gamma_{0\downarrow}\sum_\sigma \Gamma_{\sigma 0}}{\sum_\sigma \Gamma_{0\sigma}\Gamma_{\sigma 0}} + \mathcal{O}\left(\frac{1}{z}\right), \tag{A.22}$$

where $\bar\sigma$ is the spin opposite to $\sigma = \uparrow, \downarrow$. Inserting the two formulas into Eq. (A.19) yields the boundary condition presented in Eq. (4.13).

In the third parameter regime illustrated in Figure A.2 (c), the value $\lambda_3(z)$ is larger than $\mathrm{Re}[\lambda_{1,2}(z)]$ everywhere on the real axis. All zeros leave the real axis, see Figure 4.8 (c). The derivation of the boundary condition between regime (b) and (c), is quite challenging. The correct procedure is to inspect the square-root branch point depicted in Figure 4.8 (b) near $z = -1$. The parameters for which this point leaves the real axis determines the boundary condition. However, if we additionally take into account that on the boundary the system can be described by a two-state master equation, we can obtain Eq. (4.14) also by means of Eq. (A.7). This additional assumptions is justified in Section 4.3. However, for the system discussed in Section 4.2, this assumption does not hold at the boundary condition (4.10). To obtain this condition, we indeed must inspect the square-root branch point of the two largest eigenvalues.

A.3 Additional details for the inverse counting statistics

In this section, we present some additional detail concerning the inverse counting statistics discussed in Chapter 6.

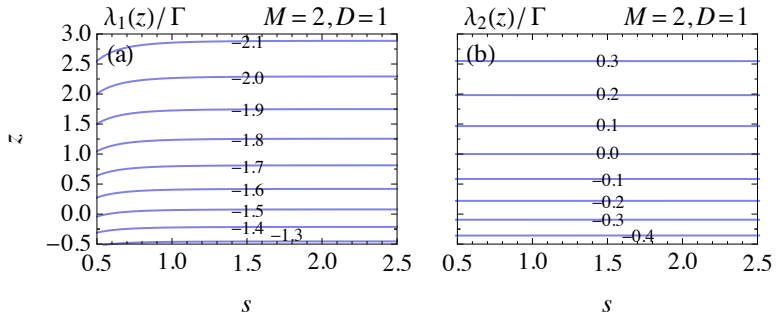

Figure A.3: Consistency check of the number of system states M and the counting power m for the single-level quantum dot $\varepsilon = -k_\mathrm{B}T$ in an external magnetic field $\Delta = 0.03\,k_\mathrm{B}T$ for time $\Gamma t = 100$. Assuming $M = 2$ and $m = 1$, contour lines of the resulting two eigenvalues $\lambda_1(z)/\Gamma$ and $\lambda_2(z)/\Gamma$ are depicted. Compare with Figure 6.4.

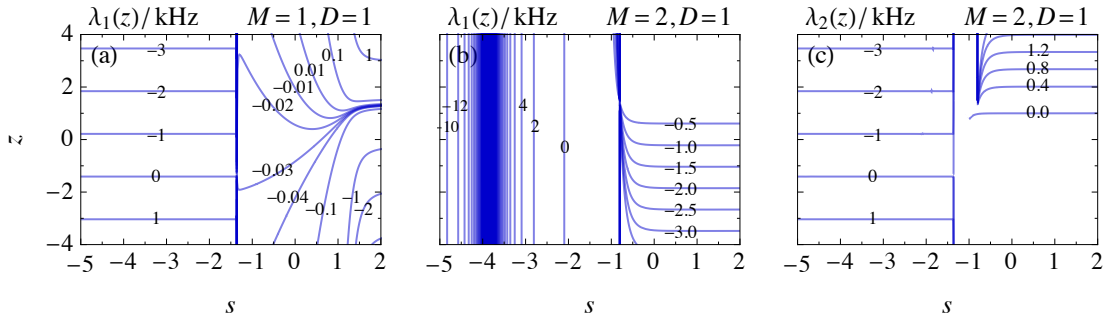

Figure A.4: Consistency check of the number of system states M and the counting power D for the single-electron box with gate charge $n_\mathrm{G} = 0.001$ for time $t = 20\,\mathrm{s}$. Assuming different values for M and D, contour lines of the resulting $j = 1, \ldots, M$ eigenvalues $\lambda_j(z)/\,\mathrm{kHz}$ are depicted. The eigenvalue for $M = 1$, $D = 1$ in (a) and the two eigenvalues for $M = 2$, $D = 1$ in (b), (c). Compare with Figure 6.7

A.3.1 Alternative expression for $A_{l,\mu\nu}$

In the sum (6.7)

$$A_{l,\mu\nu} = \sum_{\alpha_1+\ldots+\alpha_\nu=l-\mu} \frac{c_{s,\alpha_1}}{\alpha_1!} \cdot \frac{c_{s,\alpha_2}}{\alpha_2!} \cdots \frac{c_{s,\alpha_\nu}}{\alpha_\nu!}\,, \tag{A.23}$$

identical terms may occur related by permutation of the indices $(\alpha_1, \ldots, \alpha_\nu)$, e.g., $A_{\mu+2,\mu 2} = c_{s,0}c_{s,2}/2! + c_{s,1}c_{s,1} + c_{s,2}c_{s,0}/2! = c_{s,0}c_{s,2} + c_{s,1}^2$. If one wants to combine them, one obtains the alternative representation

$$A_{l,\mu\nu} = \sum_{\substack{\beta_0+\beta_1+\ldots+\beta_\nu=\nu \\ \beta_1+2\beta_2\ldots+\nu\beta_\nu=l-\mu}} \frac{\nu!}{\beta_0! \cdot \beta_1! \cdots \beta_\nu!} \left(\frac{c_{s,0}}{0!}\right)^{\beta_0} \cdot \left(\frac{c_{s,1}}{1!}\right)^{\beta_1} \cdots \left(\frac{c_{s,\nu}}{\nu!}\right)^{\beta_\nu}. \tag{A.24}$$

A.3.2 Consistency check for $\Delta = 0.03\,k_\mathrm{B}T$

For completeness, we check how close the Zeeman field must be tuned to zero in order to observe the discussed behavior of Section 6.4.2. We find that for $\Delta \lesssim 0.03\,k_\mathrm{B}T$, the eigenvalues obtained for $M = 2, D = 1$ are still almost s-independent (compare Figure A.3 with Figure 6.4), with slight deviations appearing for very negative s.

A.3.3 Consistency check for $n_\mathrm{G} = 0.001$

For the single-electron box, we estimate that at least for $|n_\mathrm{G}| \lesssim 0.001$ the $n_\mathrm{G} = 0$ case is already reached in good approximation for $s \lesssim -1.5$ or $s \gtrsim -0.5$ (compare Figure A.4 with Figure 6.7). For Figure A.4, the Andreev-tunneling rates are approximated by $\Gamma_\mathrm{A}^\pm \approx (615.11 \pm 11.42)\,\mathrm{Hz}$ [95]. The sequential tunneling rates are estimated via an interpolation between the experimental values of Ref. [32]: $\Gamma_\mathrm{u}^\pm \approx (12.00 \pm 0.03)\,\mathrm{Hz}$ and $\Gamma_\mathrm{d}^\pm \approx (252.00 \pm 0.83)\,\mathrm{Hz}$.

A.4 Additional details for the detection of coherences

In this section, we present some additional details concerning the detection of coherences in a quantum-dot spin valve as discussed in Chapter 7.

A.4.1 Current noise

The current noise Eq. (7.12) is related to the second-order ordinary cumulant by the *MacDonald formula* [149, Eq. (20)]

$$S(\omega) = 2 \lim_{\eta \to 0^+} \int_0^\infty \mathrm{d}t\, [\omega \sin(\omega t) + \eta \cos(\omega t)]\, e^{-\eta t} \frac{\mathrm{d}}{\mathrm{d}t} C_2(t)\,. \tag{A.25}$$

The cumulant $C_2(t)$ can be obtained from the time trace measured by a detector. To account for the symmetrized current operator, both the electrons tunneling in and out of the quantum dot increase the detector counter each by $1/2$. The cumulant $C_2(t)$ can be simulated by means of the generator $\mathcal{M}(z,t) = \mathbf{e}^T \exp\left[\mathbf{W}_{\exp(z/2)} t\right] \mathbf{p}_\mathrm{stat}$ with

$$\mathbf{W}_z = \begin{pmatrix} -2\Gamma_\mathrm{L} & z\Gamma_\mathrm{R} & z\Gamma_\mathrm{R} & zp\Gamma_\mathrm{R} e^{i\phi_\mathrm{R}} & zp\Gamma_\mathrm{R} e^{-i\phi_\mathrm{R}} \\ z\Gamma_\mathrm{L} & -\Gamma_\mathrm{R} & 0 & \gamma_{-+} & \gamma_{+-} \\ z\Gamma_\mathrm{L} & 0 & -\Gamma_\mathrm{R} & \gamma_{++} & \gamma_{--} \\ zp\Gamma_\mathrm{L} e^{-i\phi_\mathrm{L}} & \gamma_{--} & \gamma_{+-} & -\Gamma_\mathrm{R} & 0 \\ zp\Gamma_\mathrm{L} e^{-i\phi_\mathrm{L}} & \gamma_{++} & \gamma_{-+} & 0 & -\Gamma_\mathrm{R} \end{pmatrix}. \tag{A.26}$$

For zero frequency $\omega = 0$, Eq. (A.25) yields in accordance to the *final value theorem* of the Laplace transform

$$S(0) = 2 \left.\frac{\mathrm{d}}{\mathrm{d}t} C_2(t)\right|_{t \to \infty}. \tag{A.27}$$

For finite frequency $\omega > 0$, we take into account that $C_2(t)/t$ relaxes exponentially to a time-independent limit, see Section 6.2. Thus, we obtain

$$S(\omega) = 2 \lim_{t' \to \infty} \left[\omega \sin(\omega t') C_2(t') + \cos(\omega t') \frac{C_2(t')}{t'} - \omega^2 \int_0^{t'} \mathrm{d}t \cos(\omega t)\, C_2(t) \right] . \quad \text{(A.28)}$$

In an experiment, the time t' is always finite. Therefore, the asymptotic limit is approximated by such a large t' that the measured ratio $C_2(t')/t'$ is time independent. To simulate the finite-frequency noise, instead of calculating $C_2(t)$ and afterwards applying Eq. (A.28), it is more convenient to utilize the expression [150, Eq. (34)]

$$S(\omega) = 2\mathbf{e}^T \mathbf{W}_0^{(2)} \mathbf{p}_{\mathrm{stat}} + 2\mathbf{e}^T \mathbf{W}_0^{(1)} \left[\mathbf{\Omega}(i\omega) + \mathbf{\Omega}(-i\omega) \right] \mathbf{W}_0^{(1)} \mathbf{p}_{\mathrm{stat}} \quad \text{(A.29)}$$

with $\mathbf{W}_0^{(j)} = \partial_z^j \mathbf{W}_{\exp(z/2)}|_{z \to 0}$ and $\mathbf{\Omega}(z) = (z\mathbf{1} - \mathbf{W}_1)^{-1}$.

A.4.2 Peaks' frequencies

In the long-time limit, the generalized factorial cumulants $C_{s,m}$ are dominated by the eigenvalues with the largest real part $\mathrm{Re}[\lambda_j(z)]$ for $z = s$, cf. Section 6.2. Near $s \approx 1$, always a single real eigenvalue $\lambda_{\max}$ determines the cumulants, see Eq. (6.2). For negative s, the dominating eigenvalues may be given by a complex-conjugated pair $\lambda_1(z)$ and $\lambda_2(z)$. Taking into account that also the $c_j(z) = \left(\mathbf{e}^T \mathbf{r}_{z,j}\right) \left(\mathbf{l}_{z,j}^T \mathbf{p}_{\mathrm{stat}}\right)$ are complex-conjugated pairs, we can express the generating function in the long-time limit by

$$\mathcal{M}_z(t) = 2e^{\mathrm{Re}[\lambda_1(z)]\, t} \Big\{ \mathrm{Re}\big[c_1(z)\big] \cos\big[\mathrm{Im}\, \lambda_1(z)\, t\big] - \mathrm{Im}\big[c_1(z)\big] \sin\big[\mathrm{Im}\, \lambda_1(z)\, t\big] \Big\} . \quad \text{(A.30)}$$

Thus, the generating function has real zeros $z_j(t)$ leading to the peaks illustrated in Figs. 7.2 (a) and 7.4 (b). Since in each period $T = 2\pi/\mathrm{Im}[\lambda_1(s)]$ the generating function has two zero-crossings, the peaks occur with the frequency $2/T$.

The eigenvalues $\lambda_j(z)$ of the generator Eq. (7.11) can be calculated numerically for arbitrary parameters. However, for a better understanding of the electron transport, we need $\lambda_j(z)$ to the leading orders in the polarizations p and the counting parameter z.

To obtain the leading orders in p, we apply the ansatz

$$\lambda(z) = \sum_{j=0}^{\infty} a_j(z) p^j . \quad \text{(A.31)}$$

to solve the characteristic polynomial. If the ansatz is correct, the polynomial vanishes in every order in p. The lowest order p^0 depends only on the coefficient $a_0(z)$ and thus completely determines the first term of the eigenvalue $\lambda_j(z)$. The higher orders in p vanish accordingly for proper chosen coefficients. Thus, the ansatz has been correct. The eigenvalues take the form

$$\lambda_1(z) = -\Gamma_{\mathrm{R}} + \mathcal{O}\left(p^2\right) , \quad \text{(A.32)}$$

$$\lambda_{2,3}(z) = -\Gamma_{\mathrm{R}} \pm i\,|\mathbf{B}| + \mathcal{O}\left(p^2\right) , \quad \text{(A.33)}$$

$$\lambda_{4,5}(z) = \frac{1}{2} \left(-\Gamma' \pm \sqrt{\Gamma'^2 + (z-1) 8 \Gamma_{\mathrm{L}} \Gamma_{\mathrm{R}}} \right) + \mathcal{O}\left(p^2\right) , \quad \text{(A.34)}$$

with $\Gamma' = 2\Gamma_\mathrm{L} + \Gamma_\mathrm{R}$. The terms of order p^3 are already to long to be explicitly presented here. This order is completely real for $\lambda_1(z)$, $\lambda_2(z)$, and $\lambda_3(z)$. Hence, we obtain Eq. (7.15).

To see which eigenvalues dominate in the long-time limit for $z \ll -1$, we apply the ansatz Eq. (A.20). The leading order of $\mathrm{Re}[\lambda_j(z)]$ is independent of z and determines the dashed and green line in Figure 7.4 (a). The leading order of $\mathrm{Im}[\lambda_j(z)]$ is only independent of z for three of the five eigenvalues. For the other two, we find a dependence on $\sqrt{z}$ as presented in Eq. (7.16).

A.4.3 Factorial cumulants to leading order in p

In the short-time limit, the cumulants can be derived via Eq. (5.6)

$$C_{s,m} = (-1)^{m-1}(m-1)! \left\{1 + \frac{2\,m\,p^2\,\Gamma_\mathrm{L}[\cos(\phi)-1]}{2\Gamma_\mathrm{L}+\Gamma_\mathrm{R}}\right\} \left(\frac{2\Gamma_\mathrm{L}\Gamma_\mathrm{R}}{2\Gamma_\mathrm{L}+\Gamma_\mathrm{R}}\,t\right)^m + \mathcal{O}(p^4). \quad \text{(A.35)}$$

In the long-time limit, the factorial cumulants are given by Eq. (6.2)

$$\begin{aligned}\lim_{t\to\infty}\frac{C_{1,m}(t)}{t} = &-\frac{4^{m-1}}{\sqrt{\pi}}\left(m-\frac{3}{2}\right)!\,(2\Gamma_\mathrm{L}+\Gamma_\mathrm{R})\,x^m \\ &-\left[\frac{4^{m-1}}{\sqrt{\pi}}\,(2m\Gamma_\mathrm{L}-m\Gamma_\mathrm{R}+\Gamma_\mathrm{R})\cos(\phi)\left(m-\frac{3}{2}\right)!\right. \\ &\left.+\sum_{j=0}^{m}\left(\frac{m+1}{2}\delta_{j,0}-1\right)\frac{(2j+1)m!(2m)!\Gamma_\mathrm{R}}{(m-j)!(m+j+1)!}\left(\frac{2\Gamma_\mathrm{L}}{\Gamma_\mathrm{R}}\right)^j\right]p^2\,x^m + \mathcal{O}(p^4)\,,\end{aligned} \quad \text{(A.36)}$$

where $x = -2\Gamma_\mathrm{L}\Gamma_\mathrm{R}/(2\Gamma_\mathrm{L}+\Gamma_\mathrm{R})^2$. The Gamma function defines $m!$ for half-integer values. In both limits, the coherent oscillations enter beginning with the forth order in the polarization p. For the first three orders, the same expression is obtained if coherences are completely neglected $B_\mathrm{L} = B_\mathrm{R} = 0$ or if effectively parallel leads' magnetizations are assumed with $p_\mathrm{L} = \cos(\phi)p$ and $p_\mathrm{R} = p$.

Bibliography

[1] Y. Blanter and M. Büttiker. Shot noise in mesoscopic conductors. Physics Reports **336**, 1 (2000).

[2] C. Rössler, T. Krähenmann, S. Baer, T. Ihn, K. Ensslin, C. Reichl, and W. Wegscheider. Tunable charge detectors for semiconductor quantum circuits. New J. Phys. **15**, 033011 (2013).

[3] S. Gustavsson, R. Leturcq, M. Studer, I. Shorubalko, T. Ihn, K. Ensslin, D. Driscoll, and A. Gossard. Electron counting in quantum dots. Surface Science Reports **64**, 191 (2009).

[4] S. Gustavsson, R. Leturcq, B. Simovič, R. Schleser, P. Studerus, T. Ihn, K. Ensslin, D. C. Driscoll, and A. C. Gossard. Counting statistics and super-Poissonian noise in a quantum dot: Time-resolved measurements of electron transport. Phys. Rev. B **74**, 195305 (2006).

[5] V. F. Maisi, D. Kambly, C. Flindt, and J. P. Pekola. Full Counting Statistics of Andreev Tunneling. Phys. Rev. Lett. **112**, 036801 (2014).

[6] W. Belzig. Full counting statistics of super-Poissonian shot noise in multilevel quantum dots. Phys. Rev. B. **71**, 161301 (2005).

[7] J. Börlin, W. Belzig, and C. Bruder. Full Counting Statistics of a Superconducting Beam Splitter. Phys. Rev. Lett. **88**, 197001 (2002).

[8] J. C. Cuevas and W. Belzig. Full Counting Statistics of Multiple Andreev Reflections. Phys. Rev. Lett. **91**, 187001 (2003).

[9] G. Johansson, P. Samuelsson, and Å. Ingerman. Full Counting Statistics of Multiple Andreev Reflection. Phys. Rev. Lett. **91**, 187002 (2003).

[10] S. Pilgram and P. Samuelsson. Noise and Full Counting Statistics of Incoherent Multiple Andreev Reflection. Phys. Rev. Lett. **94**, 086806 (2005).

[11] J. P. Morten, D. Huertas-Hernando, W. Belzig, and A. Brataas. Full counting statistics of crossed Andreev reflection. Phys. Rev. B **78**, 224515 (2008).

[12] A. Braggio, M. Governale, M. G. Pala, and J. König. Superconducting proximity effect in interacting quantum dots revealed by shot noise. Solid State Commun. **151**, 155 (2011).

[13] A. Braggio, J. König, and R. Fazio. Full Counting Statistics in Strongly Interacting Systems: Non-Markovian Effects. Phys. Rev. Lett. **96**, 026805 (2006).

[14] T. L. Schmidt and A. Komnik. Charge transfer statistics of a molecular quantum dot with a vibrational degree of freedom. Phys. Rev. B **80**, 041307 (2009).

[15] C. Flindt, T. Novotný, A. Braggio, and A.-P. Jauho. Counting statistics of transport through Coulomb blockade nanostructures: High-order cumulants and non-Markovian effects. Phys. Rev. B **82**, 155407 (2010).

[16] R. Seoane Souto, R. Avriller, R. C. Monreal, A. Martín-Rodero, and A. Levy Yeyati. Transient dynamics and waiting time distribution of molecular junctions in the polaronic regime. Phys. Rev. B **92**, 125435 (2015).

[17] C. Fricke, F. Hohls, C. Flindt, and R. J. Haug. High cumulants in the counting statistics measured for a quantum dot. Physica E **42**, 848 (2010).

[18] C. Fricke, F. Hohls, N. Sethubalasubramanian, L. Fricke, and R. J. Haug. High-order cumulants in the counting statistics of asymmetric quantum dots. Appl. Phys. Lett. **96**, 202103 (2010).

[19] Y. Komijani, T. Choi, F. Nichele, K. Ensslin, T. Ihn, D. Reuter, and A. D. Wieck. Counting statistics of hole transfer in a *p*-type GaAs quantum dot with dense excitation spectrum. Phys. Rev. B **88**, 035417 (2013).

[20] C. Flindt, C. Fricke, F. Hohls, T. Novotný, K. Netočný, T. Brandes, and R. J. Haug. Universal oscillations in counting statistics. PNAS **106**, 10116 (2009).

[21] N. L. Johnson, A. W. Kemp, and S. Kotz, *Univariate Discrete Distributions* (Wiley, Hoboken, 2005).

[22] D. Kambly, C. Flindt, and M. Büttiker. Factorial cumulants reveal interactions in counting statistics. Phys. Rev. B **83**, 075432 (2011).

[23] J. von Delft and D. Ralph. Spectroscopy of discrete energy levels in ultrasmall metallic grains. Phys. Rep. **345**, 61 (2001).

[24] H. Bruus and K. Flensberg, *Many-Body Quantum Theory in Condensed Matter Physics: An Introduction* (Oxford University Press, New York, 2010).

[25] J. M. Martinis, M. Nahum, and H. D. Jensen. Metrological accuracy of the electron pump. Phys. Rev. Lett. **72**, 904 (1994).

[26] P. D. Dresselhaus, L. Ji, S. Han, J. E. Lukens, and K. K. Likharev. Measurement of single electron lifetimes in a multijunction trap. Phys. Rev. Lett. **72**, 3226 (1994).

[27] R. J. Schoelkopf, P. Wahlgren, A. A. Kozhevnikov, P. Delsing, and D. E. Prober. The Radio-Frequency Single-Electron Transistor (RF-SET): A Fast and Ultrasensitive Electrometer. Science **280**, 1238 (1998).

[28] S. V. Lotkhov, H. Zangerle, A. B. Zorin, and J. Niemeyer. Storage capabilities of a four-junction single-electron trap with an on-chip resistor. Appl. Phys. Lett. **75**, 2665 (1999).

[29] O. Astafiev, Y. A. Pashkin, T. Yamamoto, Y. Nakamura, and J. S. Tsai. Single-shot measurement of the Josephson charge qubit. Phys. Rev. B **69**, 180507 (2004).

[30] J. Bylander, T. Duty, and P. Delsing. Current measurement by real-time counting of single electrons. Nature **434**, 361 (2005).

[31] O.-P. Saira, M. Möttönen, V. F. Maisi, and J. P. Pekola. Environmentally activated tunneling events in a hybrid single-electron box. Phys. Rev. B **82**, 155443 (2010).

[32] V. F. Maisi, O.-P. Saira, Y. A. Pashkin, J. S. Tsai, D. V. Averin, and J. P. Pekola. Real-Time Observation of Discrete Andreev Tunneling Events. Phys. Rev. Lett. **106**, 217003 (2011).

[33] L. P. Kouwenhoven, D. G. Austing, and S. Tarucha. Few-electron quantum dots. Rep. Prog. Phys. **64**, 701 (2001).

[34] J. Güttinger, J. Seif, C. Stampfer, A. Capelli, K. Ensslin, and T. Ihn. Time-resolved charge detection in graphene quantum dots. Phys. Rev. B **83**, 165445 (2011).

[35] G. Gotz, G. A. Steele, W.-J. Vos, and L. P. Kouwenhoven. Real Time Electron Tunneling and Pulse Spectroscopy in Carbon Nanotube Quantum Dots. Nano Lett. **8**, 4039 (2008).

[36] W. Lu, Z. Ji, L. Pfeiffer, K. W. West, and A. J. Rimberg. Real-time detection of electron tunnelling in a quantum dot. Nature **423**, 422 (2003).

[37] T. Fujisawa, T. Hayashi, Y. Hirayama, H. D. Cheong, and Y. H. Jeong. Electron counting of single-electron tunneling current. Appl. Phys. Lett. **84**, 2343 (2004).

[38] L. M. K. Vandersypen, J. M. Elzerman, R. N. Schouten, L. H. W. van Beveren, R. Hanson, and L. P. Kouwenhoven. Real-time detection of single-electron tunneling using a quantum point contact. Appl. Phys. Lett. **85**, 4394 (2004).

[39] S. Gustavsson, R. Leturcq, B. Simovič, R. Schleser, T. Ihn, P. Studerus, K. Ensslin, D. C. Driscoll, and A. C. Gossard. Counting Statistics of Single Electron Transport in a Quantum Dot. Phys. Rev. Lett. **96**, 076605 (2006).

[40] T. Fujisawa, T. Hayashi, R. Tomita, and Y. Hirayama. Bidirectional Counting of Single Electrons. Science **312**, 1634 (2006).

[41] S. Gustavsson, R. Leturcq, T. Ihn, K. Ensslin, M. Reinwald, and W. Wegscheider. Measurements of higher-order noise correlations in a quantum dot with a finite bandwidth detector. Phys. Rev. B **75**, 075314 (2007).

[42] C. Fricke, F. Hohls, W. Wegscheider, and R. J. Haug. Bimodal counting statistics in single-electron tunneling through a quantum dot. Phys. Rev. B **76**, 155307 (2007).

[43] N. Ubbelohde, C. Fricke, C. Flindt, F. Hohls, and R. J. Haug. Measurement of finite-frequency current statistics in a single-electron transistor. Nat. Commun. **3**, 612 (2012).

[44] M. Thalakulam, C. B. Simmons, B. J. Van Bael, B. M. Rosemeyer, D. E. Savage, M. G. Lagally, M. Friesen, S. N. Coppersmith, and M. A. Eriksson. Single-shot measurement and tunnel-rate spectroscopy of a Si/SiGe few-electron quantum dot. Phys. Rev. B **84**, 045307 (2011).

[45] C. B. Simmons, J. R. Prance, B. J. Van Bael, T. S. Koh, Z. Shi, D. E. Savage, M. G. Lagally, R. Joynt, M. Friesen, S. N. Coppersmith, and M. A. Eriksson. Tunable Spin Loading and T_1 of a Silicon Spin Qubit Measured by Single-Shot Readout. Phys. Rev. Lett. **106**, 156804 (2011).

[46] J. R. Prance, Z. Shi, C. B. Simmons, D. E. Savage, M. G. Lagally, L. R. Schreiber, L. M. K. Vandersypen, M. Friesen, R. Joynt, S. N. Coppersmith, and M. A. Eriksson. Single-Shot Measurement of Triplet-Singlet Relaxation in a Si/SiGe Double Quantum Dot. Phys. Rev. Lett. **108**, 046808 (2012).

[47] M. Yuan, Z. Yang, D. E. Savage, M. G. Lagally, M. A. Eriksson, and A. J. Rimberg. Charge sensing in a Si/SiGe quantum dot with a radio frequency superconducting single-electron transistor. Appl. Phys. Lett. **101**, 142103 (2012).

[48] C. Stampfer, J. Güttinger, S. Hellmüller, F. Molitor, K. Ensslin, and T. Ihn. Energy Gaps in Etched Graphene Nanoribbons. Phys. Rev. Lett. **102**, 056403 (2009).

[49] T. Müller, J. Güttinger, D. Bischoff, S. Hellmüller, K. Ensslin, and T. Ihn. Fast detection of single-charge tunneling to a graphene quantum dot in a multi-level regime. Appl. Phys. Lett. **101**, 012104 (2012).

[50] D. Wallin, A. Fuhrer, L. E. Fröberg, L. Samuelson, H. Q. Xu, S. Hofling, and A. Forchel. Detection of charge states in nanowire quantum dots using a quantum point contact. Appl. Phys. Lett. **90**, 172112 (2007).

[51] I. Shorubalko, R. Leturcq, A. Pfund, D. Tyndall, R. Krischek, S. Schön, and K. Ensslin. Self-Aligned Charge Read-Out for InAs Nanowire Quantum Dots. Nano Lett. **8**, 382 (2008).

[52] S. Gustavsson, I. Shorubalko, R. Leturcq, T. Ihn, K. Ensslin, and S. Schön. Detecting terahertz current fluctuations in a quantum point contact using a nanowire quantum dot. Phys. Rev. B **78**, 035324 (2008).

[53] T. Choi, T. Ihn, S. Schön, and K. Ensslin. Counting statistics in an InAs nanowire quantum dot with a vertically coupled charge detector. Appl. Phys. Lett. **100**, 072110 (2012).

[54] M. J. Biercuk, D. J. Reilly, T. M. Buehler, V. C. Chan, J. M. Chow, R. G. Clark, and C. M. Marcus. Charge sensing in carbon-nanotube quantum dots on microsecond timescales. Phys. Rev. B **73**, 201402 (2006).

[55] A. Morello, J. J. Pla, F. A. Zwanenburg, K. W. Chan, K. Y. Tan, H. Huebl, M. Mottonen, C. D. Nugroho, C. Yang, J. A. van Donkelaar, A. D. C. Alves, D. N. Jamieson, C. C. Escott, L. C. L. Hollenberg, R. G. Clark, and A. S. Dzurak. Single-shot readout of an electron spin in silicon. Nature **467**, 687 (2010).

[56] S. Mahapatra, H. Büch, and M. Y. Simmons. Charge Sensing of Precisely Positioned P Donors in Si. Nano Lett. **11**, 4376 (2011).

[57] T. F. Watson, B. Weber, H. Büch, M. Fuechsle, and M. Y. Simmons. Charge sensing of a few-donor double quantum dot in silicon. Appl. Phys. Lett. **107**, 233511 (2015).

[58] T. Ihn, *Semiconductor Nanostructures: Quantum states and electronic transport* (Oxford University Press, New York, 2010).

[59] P. Schuster, *Stochasticity in Processes: Fundamentals and Applications to Chemistry and Biology* (Springer, Basel, 2016).

[60] Y. H. Wang. On the number of successes in independent trials. Stat. Sin. **3**, 295 (1993).

[61] H. Lee, L. S. Levitov, and A. Y. Yakovets. Universal statistics of transport in disordered conductors. Phys. Rev. B **51**, 4079 (1995).

[62] M. Reznikov, M. Heiblum, H. Shtrikman, and D. Mahalu. Temporal Correlation of Electrons: Suppression of Shot Noise in a Ballistic Quantum Point Contact. Phys. Rev. Lett. **75**, 3340 (1995).

[63] P. Stegmann, B. Sothmann, A. Hucht, and J. König. Detection of interactions via generalized factorial cumulants in systems in and out of equilibrium. Phys. Rev. B **92**, 155413 (2015).

[64] D. Kambly and C. Flindt. Time-dependent factorial cumulants in interacting nanoscale systems. J. Comput. Electron. **12**, 331 (2013).

[65] C. Flindt, T. Novotný, A. Braggio, M. Sassetti, and A.-P. Jauho. Counting Statistics of Non-Markovian Quantum Stochastic Processes. Phys. Rev. Lett. **100**, 150601 (2008).

[66] B. Sothmann and J. König. Nonequilibrium current and noise in inelastic tunneling through a magnetic atom. New J. Phys. **12**, 083028 (2010).

[67] J. Splettstoesser, M. Governale, J. König, and M. Büttiker. Charge and spin dynamics in interacting quantum dots. Phys. Rev. B **81**, 165318 (2010).

[68] L. D. Contreras-Pulido, J. Splettstoesser, M. Governale, J. König, and M. Büttiker. Time scales in the dynamics of an interacting quantum dot. Phys. Rev. B **85**, 075301 (2012).

[69] J. Schulenborg, J. Splettstoesser, M. Governale, and L. D. Contreras-Pulido. Detection of the relaxation rates of an interacting quantum dot by a capacitively coupled sensor dot. Phys. Rev. B **89**, 195305 (2014).

[70] J. Schulenborg, R. B. Saptsov, F. Haupt, J. Splettstoesser, and M. R. Wegewijs. Fermion-parity duality and energy relaxation in interacting open systems. Phys. Rev. B **93**, 081411 (2016).

[71] R.-P. Riwar, B. Roche, X. Jehl, and J. Splettstoesser. Readout of relaxation rates by nonadiabatic pumping spectroscopy. Phys. Rev. B **93**, 235401 (2016).

[72] J. Vanherck, J. Schulenborg, R. B. Saptsov, J. Splettstoesser, and M. R. Wegewijs. Relaxation of quantum dots in a magnetic field at finite bias – Charge, spin, and heat currents. Phys. Status Solidi B **254**, 1600614 (2017).

[73] A. Cottet, W. Belzig, and C. Bruder. Positive Cross Correlations in a Three-Terminal Quantum Dot with Ferromagnetic Contacts. Phys. Rev. Lett. **92**, 206801 (2004).

[74] H.-A. Engel and D. Loss. Asymmetric Quantum Shot Noise in Quantum Dots. Phys. Rev. Lett. **93**, 136602 (2004).

[75] T. Novotný, A. Donarini, C. Flindt, and A.-P. Jauho. Shot Noise of a Quantum Shuttle. Phys. Rev. Lett. **92**, 248302 (2004).

[76] J. Koch and F. von Oppen. Franck-Condon Blockade and Giant Fano Factors in Transport through Single Molecules. Phys. Rev. Lett. **94**, 206804 (2005).

[77] A. Thielmann, M. H. Hettler, J. König, and G. Schön. Cotunneling Current and Shot Noise in Quantum Dots. Phys. Rev. Lett. **95**, 146806 (2005).

[78] R. Sánchez, G. Platero, and T. Brandes. Resonance Fluorescence in Transport through Quantum Dots: Noise Properties. Phys. Rev. Lett. **98**, 146805 (2007).

[79] B. Sothmann, J. König, and Y. Gefen. Mesoscopic Stoner Instability in Metallic Nanoparticles Revealed by Shot Noise. Phys. Rev. Lett. **108**, 166603 (2012).

[80] S. S. Safonov, A. K. Savchenko, D. A. Bagrets, O. N. Jouravlev, Y. V. Nazarov, E. H. Linfield, and D. A. Ritchie. Enhanced Shot Noise in Resonant Tunneling via Interacting Localized States. Phys. Rev. Lett. **91**, 136801 (2003).

[81] E. Onac, F. Balestro, B. Trauzettel, C. F. J. Lodewijk, and L. P. Kouwenhoven. Shot-Noise Detection in a Carbon Nanotube Quantum Dot. Phys. Rev. Lett. **96**, 026803 (2006).

[82] P. Barthold, F. Hohls, N. Maire, K. Pierz, and R. J. Haug. Enhanced Shot Noise in Tunneling through a Stack of Coupled Quantum Dots. Phys. Rev. Lett. **96**, 246804 (2006).

[83] Y. Chen and R. A. Webb. Positive Current Correlations Associated with Super-Poissonian Shot Noise. Phys. Rev. Lett. **97**, 066604 (2006).

[84] O. Zarchin, Y. C. Chung, M. Heiblum, D. Rohrlich, and V. Umansky. Electron Bunching in Transport through Quantum Dots in a High Magnetic Field. Phys. Rev. Lett. **98**, 066801 (2007).

[85] Y. Zhang, L. DiCarlo, D. T. McClure, M. Yamamoto, S. Tarucha, C. M. Marcus, M. P. Hanson, and A. C. Gossard. Noise Correlations in a Coulomb-Blockaded Quantum Dot. Phys. Rev. Lett. **99**, 036603 (2007).

[86] G. Kießlich, E. Schöll, T. Brandes, F. Hohls, and R. J. Haug. Noise Enhancement due to Quantum Coherence in Coupled Quantum Dots. Phys. Rev. Lett. **99**, 206602 (2007).

[87] M. E. Rose, *Elementary theory of angular momentum* (Wiley, New York, 1957).

[88] P. Stegmann, *Spin dynamics in nanoparticles in the mesoscopic Stoner regime*, Master thesis (Universität Duisburg-Essen, 2013).

[89] J. König, *Resonanztunneln in mesoskopischen Systemen*, Diploma thesis (Universität Karlsruhe, 1995).

[90] J. König, H. Schoeller, and G. Schön. Zero-Bias Anomalies and Boson-Assisted Tunneling Through Quantum Dots. Phys. Rev. Lett. **76**, 1715 (1996).

[91] J. König, J. Schmid, H. Schoeller, and G. Schön. Resonant tunneling through ultrasmall quantum dots: Zero-bias anomalies, magnetic-field dependence, and boson-assisted transport. Phys. Rev. B. **54**, 16820 (1996).

[92] H. Schoeller, *Mesoscopic Electron Transport* (Kluwer, Dordrecht, 1997).

[93] J. König, *Quantum Fluctuations in the Single-Electron Transistor* (Shaker, Aachen, 1999).

[94] P. Stegmann and J. König. Short-time counting statistics of charge transfer in Coulomb-blockade systems. Phys. Rev. B **94**, 125433 (2016).

[95] D. V. Averin and J. P. Pekola. Nonadiabatic Charge Pumping in a Hybrid Single-Electron Transistor. Phys. Rev. Lett. **101**, 066801 (2008).

[96] W. Belzig and Y. V. Nazarov. Full Counting Statistics of Electron Transfer between Superconductors. Phys. Rev. Lett. **87**, 197006 (2001).

[97] H. Soller and A. Komnik. Full counting statistics of interacting quantum dots contacted by a normal metal and a superconductor. Europhys. Lett. **106**, 37009 (2014).

[98] A. F. Andreev. The thermal conductivity of the intermediate state in superconductors. Sov. Phys. JETP **19**, 1228 (1964).

[99] J. P. Pekola, V. F. Maisi, S. Kafanov, N. Chekurov, A. Kemppinen, Y. A. Pashkin, O.-P. Saira, M. Möttönen, and J. S. Tsai. Environment-Assisted Tunneling as an Origin of the Dynes Density of States. Phys. Rev. Lett. **105**, 026803 (2010).

[100] A. B. Kolomeisky and M. E. Fischer. Molecular Motors: A Theorist's Perspective. Annu. Rev. Phys. Chem. **58**, 675 (2007).

[101] Y. R. Chemla, J. R. Moffitt, and C. Bustamante. Exact Solutions for Kinetic Models of Macromolecular Dynamics. J. Phys. Chem. B **112**, 6025 (2008).

[102] R. Zhou, S. Kunzelmann, M. R. Webb, and T. Ha. Detecting Intramolecular Conformational Dynamics of Single Molecules in Short Distance Range with Subnanometer Sensitivity. Nano Lett. **11**, 5482 (2011).

[103] Y. Choi, I. S. Moody, P. C. Sims, S. R. Hunt, B. L. Corso, I. Perez, G. A. Weiss, and P. G. Collins. Single-Molecule Lysozyme Dynamics Monitored by an Electronic Circuit. Science **335**, 319 (2012).

[104] H. S. Chung, K. McHale, J. M. Louis, and W. A. Eaton. Single-Molecule Fluorescence Experiments Determine Protein Folding Transition Path Times. Science **335**, 981 (2012).

[105] B. P. English, W. Min, A. M. van Oijen, K. T. Lee, G. Luo, H. Sun, B. J. Cherayil, S. C. Kou, and X. S. Xie. Ever-fluctuating single enzyme molecules: Michaelis-Menten equation revisited. Nat. Chem. Biol. **2**, 87 (2006).

[106] J. R. Moffitt and C. Bustamante. Extracting signal from noise: kinetic mechanisms from a Michaelis–Menten-like expression for enzymatic fluctuations. FEBS J. **281**, 498 (2014).

[107] P. V. Cornish and T. Ha. A Survey of Single-Molecule Techniques in Chemical Biology. ACS Chem. Biol. **2**, 53 (2007).

[108] H. Kim and T. Ha. Single-molecule nanometry for biological physics. Rep. Prog. Phys. **76**, 016601 (2013).

[109] M. Bruderer, L. D. Contreras-Pulido, M. Thaller, L. Sironi, D. Obreschkow, and M. B. Plenio. Inverse counting statistics for stochastic and open quantum systems: the characteristic polynomial approach. New J. Phys. **16**, 033030 (2014).

[110] P. Stegmann and J. König. Inverse counting statistics based on generalized factorial cumulants. New J. Phys. **19**, 023018 (2017).

[111] G. Fève, A. Mahé, J.-M. Berroir, T. Kontos, B. Plaçais, D. C. Glattli, A. Cavanna, B. Etienne, and Y. Jin. An On-Demand Coherent Single-Electron Source. Science **316**, 1169 (2007).

[112] A. Mahé, F. D. Parmentier, E. Bocquillon, J.-M. Berroir, D. C. Glattli, T. Kontos, B. Plaçais, G. Fève, A. Cavanna, and Y. Jin. Current correlations of an on-demand single-electron emitter. Phys. Rev. B **82**, 201309 (2010).

[113] A. Beckel, A. Kurzmann, M. Geller, A. Ludwig, A. D. Wieck, J. König, and A. Lorke. Asymmetry of charge relaxation times in quantum dots: The influence of degeneracy. Europhys. Lett. **106**, 47002 (2014).

[114] A. Hofmann, V. F. Maisi, C. Gold, T. Krähenmann, C. Rössler, J. Basset, P. Märki, C. Reichl, W. Wegscheider, K. Ensslin, and T. Ihn. Measuring the Degeneracy of Discrete Energy Levels Using a GaAs/AlGaAs Quantum Dot. Phys. Rev. Lett. **117**, 206803 (2016).

[115] A. Kurzmann, B. Merkel, B. Marquardt, A. Beckel, A. Ludwig, A. D. Wieck, A. Lorke, and M. Geller. Electron dynamics in transport and optical measurements of self-assembled quantum dots. Phys. Status Solidi B **254**, 1600625 (2017).

[116] T. Brandes. Waiting times and noise in single particle transport. Ann. Phys. **17**, 477 (2008).

[117] L. Rajabi, C. Pöltl, and M. Governale. Waiting Time Distributions for the Transport through a Quantum-Dot Tunnel Coupled to One Normal and One Superconducting Lead. Phys. Rev. Lett. **111**, 067002 (2013).

[118] S. Droste, J. Splettstoesser, and M. Governale. Finite-frequency noise in a quantum dot with normal and superconducting leads. Phys. Rev. B **91**, 125401 (2015).

[119] M. M. Deshmukh and D. C. Ralph. Using Single Quantum States as Spin Filters to Study Spin Polarization in Ferromagnets. Phys. Rev. Lett. **89**, 266803 (2002).

[120] A. Bernand-Mantel, P. Seneor, K. Bouzehouane, S. Fusil, C. Deranlot, F. Petroff, and A. Fert. Anisotropic magneto-Coulomb effects and magnetic single-electron-transistor action in a single nanoparticle. Nat. Phys. **5**, 920 (2009).

[121] K. Hamaya, M. Kitabatake, K. Shibata, M. Jung, S. Ishida, T. Taniyama, K. Hirakawa, Y. Arakawa, and T. Machida. Spin-Related Current Suppression in a Semiconductor Quantum Dot Spin-Diode Structure. Phys. Rev. Lett. **102**, 236806 (2009).

[122] A. N. Pasupathy, R. C. Bialczak, J. Martinek, J. E. Grose, L. A. K. Donev, P. L. McEuen, and D. C. Ralph. The Kondo Effect in the Presence of Ferromagnetism. Science **306**, 86 (2004).

[123] K. Yoshida, I. Hamada, S. Sakata, A. Umeno, M. Tsukada, and K. Hirakawa. Gate-Tunable Large Negative Tunnel Magnetoresistance in Ni–C60–Ni Single Molecule Transistors. Nano Lett. **13**, 481 (2013).

[124] Y. Hu, H. O. H. Churchill, D. J. Reilly, J. Xiang, C. M. Lieber, and C. M. Marcus. A Ge/Si heterostructure nanowire-based double quantum dot with integrated charge sensor. Nat Nano **2**, 622 (2007).

[125] L. Hofstetter, A. Geresdi, M. Aagesen, J. Nygård, C. Schönenberger, and S. Csonka. Ferromagnetic Proximity Effect in a Ferromagnet–Quantum-Dot–Superconductor Device. Phys. Rev. Lett. **104**, 246804 (2010).

[126] A. Jensen, J. R. Hauptmann, J. Nygård, J. Sadowski, and P. E. Lindelof. Hybrid Devices from Single Wall Carbon Nanotubes Epitaxially Grown into a Semiconductor Heterostructure. Nano Lett. **4**, 349 (2004).

[127] S. Sahoo, T. Kontos, J. Furer, C. Hoffmann, M. Graber, A. Cottet, and C. Schonenberger. Electric field control of spin transport. Nat. Phys. **1**, 99 (2005).

[128] J. R. Hauptmann, J. Paaske, and P. E. Lindelof. Electric-field-controlled spin reversal in a quantum dot with ferromagnetic contacts. Nat. Phys. **4**, 373 (2008).

[129] M. Gaass, A. K. Hüttel, K. Kang, I. Weymann, J. von Delft, and C. Strunk. Universality of the Kondo Effect in Quantum Dots with Ferromagnetic Leads. Phys. Rev. Lett. **107**, 176808 (2011).

[130] A. D. Crisan, S. Datta, J. J. Viennot, M. R. Delbecq, A. Cottet, and T. Kontos. Harnessing spin precession with dissipation. Nat. Commun. **7**, 10451 (2016).

[131] B. Sothmann. Electronic waiting-time distribution of a quantum-dot spin valve. Phys. Rev. B **90**, 155315 (2014).

[132] M. Braun, J. König, and J. Martinek. Theory of transport through quantum-dot spin valves in the weak-coupling regime. Phys. Rev. B **70**, 195345 (2004).

[133] I. Weymann and J. Barnaś. Cotunneling through quantum dots coupled to magnetic leads: Zero-bias anomaly for noncollinear magnetic configurations. Phys. Rev. B **75**, 155308 (2007).

[134] R. Hornberger, S. Koller, G. Begemann, A. Donarini, and M. Grifoni. Transport through a double-quantum-dot system with noncollinearly polarized leads. Phys. Rev. B **77**, 245313 (2008).

[135] M. M. E. Baumgärtel, M. Hell, S. Das, and M. R. Wegewijs. Transport and Accumulation of Spin Anisotropy. Phys. Rev. Lett. **107**, 087202 (2011).

[136] B. Muralidharan and M. Grifoni. Thermoelectric spin accumulation and long-time spin precession in a noncollinear quantum dot spin valve. Phys. Rev. B **88**, 045402 (2013).

[137] S. Göttel, F. Reininghaus, and H. Schoeller. Generic fixed point model for pseudo-spin-$\frac{1}{2}$ quantum dots in nonequilibrium: Spin-valve systems with compensating spin polarizations. Phys. Rev. B **92**, 041103 (2015).

[138] S. Hoffman and Y. Tserkovnyak. Magnetic exchange and nonequilibrium spin current through interacting quantum dots. Phys. Rev. B **91**, 245427 (2015).

[139] S. Weiss, J. Brüggemann, and M. Thorwart. Spin vibronics in interacting nonmagnetic molecular nanojunctions. Phys. Rev. B **92**, 045431 (2015).

[140] S. Wenderoth, J. Bätge, and R. Härtle. Sharp peaks in the conductance of a double quantum dot and a quantum-dot spin valve at high temperatures: A hierarchical quantum master equation approach. Phys. Rev. B **94**, 121303 (2016).

[141] M. Braun, J. König, and J. Martinek. Frequency-dependent current noise through quantum-dot spin valves. Phys. Rev. B **74**, 075328 (2006).

[142] B. Sothmann, J. König, and A. Kadigrobov. Influence of spin waves on transport through a quantum-dot spin valve. Phys. Rev. B **82**, 205314 (2010).

[143] B. Sothmann and J. König. Transport through quantum-dot spin valves containing magnetic impurities. Phys. Rev. B **82**, 245319 (2010).

[144] S. Lindebaum, D. Urban, and J. König. Spin-induced charge correlations in transport through interacting quantum dots with ferromagnetic leads. Phys. Rev. B **79**, 245303 (2009).

[145] D. J. Monsma and S. S. P. Parkin. Spin polarization of tunneling current from ferromagnet/Al2O3 interfaces using copper-doped aluminum superconducting films. Appl. Phys. Lett. **77**, 720 (2000).

[146] R. K. P. Zia and B. Schmittmann. A possible classification of nonequilibrium steady states. J. Phys. A **39**, L407 (2006).

[147] R. K. P. Zia and B. Schmittmann. Probability currents as principal characteristics in the statistical mechanics of non-equilibrium steady states. J. Stat. Mech.: Theory Exper. **2007**, P07012 (2007).

[148] P. Stegmann and J. König. Violation of detailed balance for charge-transfer statistics in Coulomb-blockade systems. Phys. Status Solidi B **254**, 1600507 (2017).

[149] C. Flindt, T. Novotný, and A.-P. Jauho. Current noise spectrum of a quantum shuttle. Physica E **29**, 411 (2005).

[150] D. Marcos, C. Emary, T. Brandes, and R. Aguado. Finite-frequency counting statistics of electron transport: Markovian theory. New J. Phys. **12**, 123009 (2010).

Danksagung

An erster Stelle danke ich Herrn Prof. Dr. Jürgen König für die Betreuung meiner Promotion und für die Möglichkeit auf diesem spannenden Gebiet forschen zu dürfen.

Prof. Dr. Björn Sothmann danke ich dafür, dass er mich in das Gebiet eingeführt hat.

Mein Dank gilt auch Dr. Stephan Weiß, Eric Kleinherbers und meinem Bruder Dr. Thomas Stegmann für wissenschaftliche Diskussionen und Anmerkungen zum vorliegenden Text.

Dr. Alfred Hucht danke ich insbesondere für seine Ratschläge zur Programmierung mit Mathematica.

Bedanken möchte ich mich ebenfalls bei den Mitarbeitern der AG König, AG Entel und AG Sothmann für die angenehme Arbeitsatmosphäre sowie physikalische und nicht-physikalische Gespräche.

Erklärung

Ich versichere, dass ich die von mir vorgelegte Dissertation selbständig angefertigt, die benutzten Quellen und Hilfsmittel vollständig angegeben und die Stellen der Arbeit – einschließlich der Abbildungen –, die anderen Werken im Wortlaut oder dem Sinn nach entnommen sind, in jedem Einzelfall als Entlehnung kenntlich gemacht habe; dass diese Dissertation noch keiner anderen Fakultät oder Universität zur Prüfung vorgelegen hat; dass sie – abgesehen von unten angegebenen Teilpublikationen – noch nicht veröffentlich worden ist sowie, dass ich eine solche Veröffentlichung vor Abschluss des Promotionsverfahrens nicht vornehmen werde. Die Bestimmungen dieser Promotionsordnung sind mir bekannt. Die von mir vorgelegte Dissertation ist von Herrn Professor Dr. Jürgen König betreut worden.

Duisburg, 30. März 2017

Teilpublikationen

1. P. Stegmann, B. Sothmann, A. Hucht, and J. König, Detection of interactions via generalized factorial cumulants in systems in and out of equilibrium, Phys. Rev. B **92**, 155413 (2015).
2. P. Stegmann and J. König, Short-time counting statistics of charge transfer in Coulomb-blockade systems, Phys. Rev. B **94**, 125433 (2016).
3. P. Stegmann and J. König, Inverse counting statistics based on generalized factorial cumulants, New J. Phys. **19**, 023018 (2017).
4. P. Stegmann and J. König, Violation of detailed balance for charge-transfer statistics in Coulomb-blockade systems, Phys. Status Solidi B **254**, 1600507 (2017).

Curriculum Vitae

Der Lebenslauf ist in der Online-Version dieser Dissertation aus Gründen des Datenschutzes nicht enthalten.